Midlatitude Storm Track Response to Increased Greenhouse Warming

Yutian Wu

Submitted in partial fulfillment of the

requirements for the degree

of Doctor of Philosophy

in the Graduate School of Arts and Sciences

COLUMBIA UNIVERSITY

2012

ABSTRACT

Midlatitude Storm Track Response to Increased Greenhouse Warming

Yutian Wu

Storm tracks play a major role in regulating the precipitation and hydrological cycle in the midlatitudes. The changes in the location and amplitude of the storm tracks in response to global warming will have significant impacts on the poleward transport of heat, momentum and moisture and on the hydrological cycle. Recent studies have indicated a poleward shift of the storm tracks and midlatitude precipitation zone in the warming world that will contribute to subtropical drying and higher latitude moistening. This dissertation is to investigate the storm track response to increased greenhouse warming and the dynamical mechanisms driving the changes in the storm tracks using comprehensive climate models.

First, by analyzing the band-pass filtered eddy statistics simulated in the Geophysical Fluid Dynamics Laboratory (GFDL) Coupled Model version 2.1 (CM2.1) anthropogenic climate change experiments (A1B scenario), we confirm the poleward and upward shift and intensification of the storm tracks in the late 21st century. It has been found that this key feature is generally consistent with the change in Eady

growth rate. Diagnosis of the latitude-by-latitude energy budget for the current and future climate demonstrates how the coupling between radiative and surface heat fluxes and eddy heat and moisture transport influences the midlatitude storm track response to global warming. Through radiative forcing by increased atmospheric carbon dioxide and water vapor and increased solar absorption due to less low cloud cover in the subtropics, more energy is gained within the tropics and subtropics, while in the middle and high latitudes energy is reduced through increased outgoing terrestrial radiation in the Northern Hemisphere and increased ocean heat uptake in the Southern Hemisphere. This enhanced energy imbalance in the future climate requires larger poleward atmospheric energy transports in the midlatitudes which are partially accomplished by the intensified storm tracks. This strong connection between intensified storm track energy transports and intensified energy imbalance in the atmosphere is also confirmed in other CMIP3/IPCC AR4 models.

We further explore the dynamical mechanisms inducing the changes in the general circulation of the atmosphere due to increased carbon dioxide (CO_2) by looking into the transient step-by-step adjustment of the circulation. This allows an assessment of the causality sequence in the circulation and thermal structure response prior ro establishment of a quasi-equilibrium state. The transient atmospheric adjustment is examined using the National Center for Atmospheric Research (NCAR) Community Atmospheric Model version 3 (CAM3) coupled to a slab ocean model and the CO_2 concentration in the atmosphere is uniformly and instantaneously doubled. The thermal structure and circulation response is well established after one year of integration with the magnitudes gradually increasing afterwards towards quasi-equilibrium. Tropical upper tropospheric warming occurs in the first

month. The expansion of the warming in the middle and upper troposphere to the subtropics occurs later and is found to be primarily dynamically-driven due to the intensification of transient eddy momentum flux convergence and resulting anomalous descending motion in this region. This linkage between the eddy-driven vertical motion anomaly and the subtropical warming expansion in the middle and upper troposphere is also confirmed in the late 21st century in an ensemble of the CMIP3/IPCC AR4 coupled climate model simulations.

Our modeling results also demonstrate the sequential response of the zonal wind anomaly in the vertical column of the atmosphere during the transient adjustment process and the poleward displacement of the tropospheric jet streams occurs after the westerly acceleration anomaly in the subpolar stratosphere. It suggests the importance of the stratosphere and its coupling with the troposphere in regulating the extratropical tropospheric circulation response to CO_2 doubling. Three phases take place during the transient adjustment process including a fast radiative-induced thermal response in the stratosphere, a westerly acceleration in the stratosphere and a 'downward propagation' of the westerly anomaly from the stratosphere to the troposphere followed by a poleward shift of the tropospheric zonal jets. Diagnoses using wave spectra and index of refraction are used to understand the dynamics associated with each phase.

Contents

List of Tables

List of Figures

Acknowledgments

I owe my deepest gratitude to my Ph.D. advisors, Professor Mingfang Ting and Professor Richard Seager, who brought me into the field of climate science and guided and encouraged me all the way to the completion of this dissertation.

I would like to thank Professor Mark A. Cane, Professor Lorenzo M. Polvani and Professor Geoffrey K. Vallis from the Geophysical Fluid Dynamics Laboratory at Princeton University for kindly agreeing to serve on my thesis committee.

I would also like to thank every one in the Division of Ocean and Climate Physics at Lamont-Doherty Earth Observatory for helpful guidance and discussions and I have really enjoyed working in the group.

I am heartily thankful to my parents for their great support and encouragement.

To those who educate me and whom I love

Chapter 1

Introduction

1.1 Motivations

Midlatitude storm tracks play an important role in the Earth's climate system. Eddies within the storm tracks transport large amounts of energy poleward affecting the mean climate while much climate variability on seasonal to decadal timescales is associated with changes in the storm tracks. Previous studies have contributed greatly to our understanding of the dynamics of the storm tracks in the present climate (see a review by Chang et al., 2002). It is expected that as a consequence of increased greenhouse warming, the location and intensity of the midlatitude storm tracks will change.

The dynamics controlling the midlatitude storm tracks are complex and don't provide an easy answer to how the storm activity will respond to increased carbon dioxide (CO_2) in the atmosphere (e.g., Held, 1993). First of all, the conversion of available potential energy in the atmosphere supplies the energy for the growth of transient eddies according to linear baroclinic instability theory. The linear baroclinic instability growth rate is affected by both static stability and meridional temperature gradients in the atmosphere. In a warmer climate, temperature

gradients near the surface in northern winter are expected to weaken (except for the North Atlantic region) due to strong high latitude warming whereas those in the upper troposphere strengthen (e.g., Meehl et al., 2007b). Consequently, the resulting baroclinicity tends to weaken in the lower troposphere but strengthen in the upper troposphere. It is unclear in the real atmosphere which of the two opposing changes dominates the storm activity although linear instability theory and numerical experiments suggest that the lower-tropospheric baroclinicity has a stronger influence on mid-latitude eddy activity (e.g., Held and O'Brien, 1992; Pavan et al., 1999; Lunkeit et al., 1998). Second, previous studies have noted the strong influence of atmospheric moisture on the midlatitude dynamics and eddy energy fluxes (Emanuel et al., 1987; Lapeyre and Held, 2004; Frierson et al., 2007), which can occur in varying ways (e.g., Held, 1993; Pavan et al., 1999). For example, increased latent heat release in the warm sector of rising air in the storm system can provide a source of available potential energy leading to more intense storms (Emanuel et al., 1987; Held, 1993); on the other hand, less intense and less frequent storms can be expected as the eddies in moist air are more efficient in transferring energy poleward (Held, 1993). Therefore, one purpose of this thesis work is to diagnose how the midlatitude storm tracks are expected to change in a warmer climate from comprehensive climate model simulations and how these changes are related to the mean climate states and other components in the general circulation of the atmosphere from the perspective of global energy balance.

Climate models for the Coupled Model Intercomparison Project Phase 3 (CMIP3) / Intergovernmental Panel on Climate Change (IPCC) Fourth Assessment Report (AR4) have projected a poleward displacement of the midlatitude storm tracks associated with poleward shifts in surface wind stress and precipitation (Yin, 2005). However, the dynamical mechanisms underlying the changes in storm tracks are not well understood, in particular, the cause and effect that sequentially takes place in

the extratropical troposphere in response to global warming. Some possible mechanisms have been proposed to understand the simulation results. For example, Lorenz and DeWeaver (2007) suggested that the midlatitude circulation response to global warming is predominantly driven by the rising tropopause height; Chen and Held (2007) and Lu et al. (2008) attributed the trend to the increasing phase speed of the midlatitude eddies and the resulting poleward shift of the subtropical breaking region and the transient eddy momentum flux convergence; Lu et al. (2008) suggested another possibility of the rising tropospheric static stability that shifts the Hadley Cell, the baroclinic instability zone and thus the midlatitude eddies poleward; Kidston et al. (2010) and Kidston et al. (2011) argued that the increase in eddy length scale can move the surface westerlies poleward. Although the above mechanisms have sufficient evidence in both theory and idealized numerical experiments, they are all derived based on the equilibrium response of the CMIP3/IPCC AR4 climate model simulations and whether and how they really make impacts are not clear. Therefore, modeling experiments looking into the transient adjustment prior to the equilibrium state can provide valuable insights into the dynamical mechanisms, particularly the step-by-step sequence of the circulation change. This methodology has been applied successfully to the study of cause and effect in the tropospheric response to El Niño SST anomalies where the subtropical jets and the midlatitude eddies move equatorward (Seager et al., 2003a; Seager and Vecchi, 2010; Seager et al., 2010a,b; Harnik et al., 2010). Furthermore, the transient adjustment experiments also allow an assessment of all the possible mechanisms that have been proposed before within the same modeling framework.

1.2 Midlatitude Storm Track Variability and Dynamics

Not only the day-to-day weather system but also the climatic variability in the midlatitudes is largely effected by the baroclinic eddies or the synoptic storm activity. Eddies transport angular momentum into the midlatitudes and induce surface westerlies and the Ferrel Cell via upper-level angular momentum flux convergence. Eddies also help export water vapor into the upper troposphere in the extratropics from the source region in the tropics and subtropics, shaping the precipitation distribution and temperature structure of the planet. The midlatitude eddies closely link the extratropical circulation dynamics with every other component in the general circulation of the atmosphere, for example, the strength and meridional extent of the Hadley circulation (Walker and Schneider, 2006) as well as the rapid transition of the monsoon circulation (Bordoni and Schneider, 2008, 2010, and thus deserve thorough understanding.

There have been two basic approaches in diagnosing the preferred regions for synoptic storm activity in the midlatitudes, or the *storm tracks*. The first method identifies the weather systems, tracks their positions and intensities with time and generates statistics of cyclone occurrence and cyclogenesis (e.g., Klein, 1957; Hoskins and Hodges, 2002). The second approach defines the storm tracks as the 'geographically localized maxima in band-pass transient variance' in various climate variables, for example, geopotential height, meridional wind velocity and poleward eddy heat flux (e.g., Blackmon, 1976; Chang et al., 2002). There are generally similarities among different climate variables in representing the storm tracks except for some regional differences (e.g., Hoskins and Hodges, 2002; Chang et al., 2002). This thesis work uses the second approach i.e., band-pass transient eddy statistics, for the definition of the storm tracks.

Figure 1.1(a) shows the band-pass filtered eddy meridional velocity variance $\overline{v'v'}$ at upper tropospheric level 250mb using the daily data from the National Centers for Environmental Prediction-National Center for Atmospheric Research (NCEP-NCAR) reanalysis (Kalnay and Coauthors, 1996) for December-January-February (DJF) averaged over the years 1961-2000. Figure 1.1(c) shows the climatological zonal average $\langle\overline{v'v'}\rangle$ as a function of latitude and pressure level. The brackets denote zonal averages and the bars denote time averages. A 21-point standard band-pass filter is applied to daily variables to retain the variability on synoptic time scales of 2-8 days (see Appendix A in Chapter 2 for more information on the band-pass filter). As shown in Fig. 1.1(a), the Northern Hemisphere (NH) climatological storm tracks are characterized by a large-scale longitudinal path maximized in the mid-latitudes between 30^oN and 70^oN extending from the central North Pacific Ocean, across North America and the North Atlantic Ocean, into the western Europe. The NH storm tracks have maximum intensity over the North Pacific and North Atlantic basins with reduced intensity over the continents downstream. The Southern Hemisphere (SH) storm tracks cover the midlatitude band of the Southern Ocean and are more zonally symmetric than the ones in the NH with a localized maximum over the Indian Ocean. In Fig. 1.1(c), the maximum intensity in the storm tracks is localized in the upper troposphere between about 200mb and 300mb which is in agreement with the maximum zonal wind shear in this region. Because of the zonal symmetry in the SH, the zonal mean intensity of the storm tracks is in fact slightly larger in the SH than in the NH.

The midlatitude storm tracks also exhibit a strong seasonal and interannual variability. Although the midlatitude weather system is considered to grow in regions of high baroclinic instability, the "midwinter suppression" of the North Pacific storm track shows a minimum in storm activity while a maximum in zonal wind shear in January (Nakamura, 1992). The location of the storm tracks is also modu-

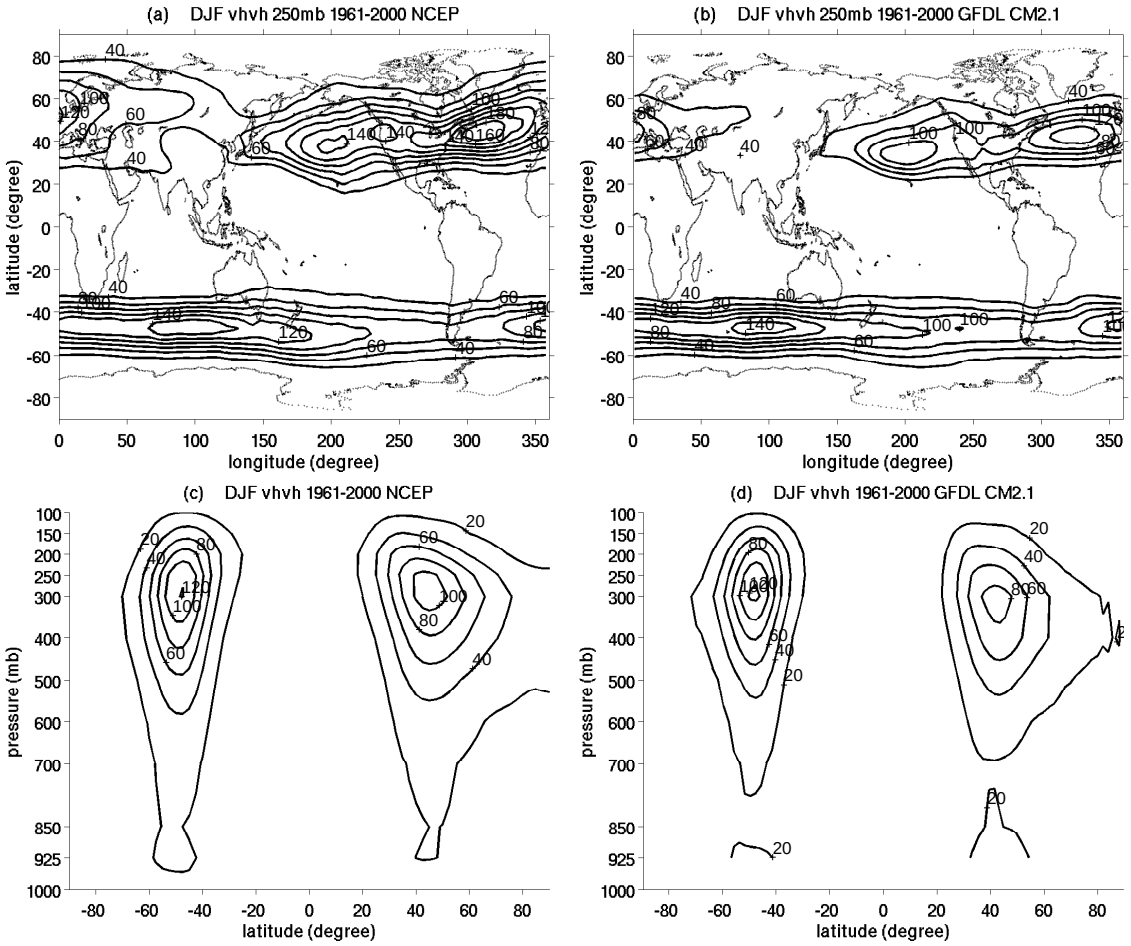

Figure 1.1: Comparison of band-pass filtered variance of meridional velocity, $\overline{v'v'}$, produced in the GFDL CM2.1 model simulations (right column) with that derived in the NCEP-NCAR reanalysis (left column). (a) shows the climatology of $\overline{v'v'}$ at 250mb and (c) shows the zonal mean $\langle\overline{v'v'}\rangle$ as a function of latitude and pressure level (mb) for December-January-February (DJF) during the years 1961-2000 from the NCEP-NCAR reanalysis. $(b)(d)$ are the counterparts from the model simulations. Contour intervals are 20 m^2/s^2. A band-pass filter has been applied to produce the variability of 2-8 days.

lated by interannual variabilities such as the El Niño Southern Oscillation (ENSO). The storm tracks are generally displaced equatorward and downstream during the El Niños with an opposite shift in La Nina years. The dynamical mechanisms have been attributed to the changing propagation path of the transient eddies due to the tropical heating anomalies and resulting equatorward shift of the subtropical jets (Seager et al., 2003a; Harnik et al., 2010).

It is well established that the baroclinic instability is the major mechanism in the generation of transient eddies, either through the growth rate of linear baroclinic instability or through the conversion of mean available potential energy (Charney, 1947; Eady, 1949; Lorenz, 1955). The warm ocean currents in the North Pacific and Atlantic oceans off the east coasts of the continents constitute sources of large baroclinic instability over these regions, especially in the winter season. While baroclinic conversion is indeed a maximum immediately downstream of the source of enhanced baroclinicity, baroclinic eddies tend to develop further downstream via downstream radiation of energy (Simmons and Hoskins, 1979; Orlanski and Chang, 1993; Chang and Orlanski, 1993). Other factors are also considered important in the maintenance of the storm tracks such as the diabatic heating (e.g., Hoskins and Valdes, 1990; Chang et al., 2002; Chang, 2009) and the planetary stationary waves (e.g., Broccoli and Manabe, 1992; Lee and Mak, 1996).

The current generation of comprehensive climate models is able to capture the major features of the midlatitude storm tracks. Figure 1.1(b)(d) shows the 250mb $\overline{v'v'}$ and the zonal mean $\langle\overline{v'v'}\rangle$, respectively, simulated by the Geophysical Fluid Dynamics Laboratory (GFDL) Coupled Model version 2.1 (CM2.1). Compared with the observations shown in Fig. 1.1(a)(c), the locations of the North Pacific and Atlantic storm tracks are well simulated as well as those in the SH. But the North Atlantic storm track simulated in the model is more zonally oriented than that in observations. The NH storm tracks are generally weaker in the GFDL

CM2.1 model than in observations while the magnitude of the SH storm tracks is well simulated. Similar results are found comparing other eddy statistics between the model simulation and reanalysis in both DJF and June-July-August (JJA) (not shown).

1.3 Various Perspectives on the Changes in Storm Track Location and Intensity in A Warmer Climate

In this section, we summarize various viewpoints on the changes in storm track location and intensity during climate change. Probably because of the complex dynamics governing the storm tracks, there is no consensus on how the midlatitude storm activity will change as a consequence of increased CO_2 among observations, idealized and comprehensive model simulations.

Recent studies using reanalyses for the latter half of the 20th century have found an increase in intensity of the midlatitude cyclones and a decrease in frequency (e.g., McCabe et al., 2001; Fyfe, 2003). General circulation models forced with increased greenhouse gases agree with this result (Lambert, 1995; Geng and Sugi, 2003; Lambert and Fyfe, 2006; Gastineau and Soden, 2009). Hall et al. (1994) found northward shifted and downstream intensified storm tracks with doubled CO_2 using the UK Meteorological Office atmospheric general circulation model (AGCM) with a mixed-layer slab ocean model. They also examined the total zonal mean poleward energy transport and found increased latent heat transport by transient eddies in the doubled CO_2 experiments which was required by the planetary energy budget. Yin (2005) found a consistent poleward and upward shift of the band-pass filtered transient eddy kinetic energy (EKE) among 15 IPCC AR4 coupled models, which

agrees with the poleward shift of the maximum baroclinic instability growth rate, the surface wind stress and the precipitation. The response in the storm tracks is in fact closely related to other components in the global general circulation of the atmosphere, for example, the poleward expansion of the Hadley Cell (Lu et al., 2007), the poleward shift of the tropospheric zonal jets (Kushner et al., 2001; Lorenz and DeWeaver, 2007) and the rise in tropopause height (Kushner et al., 2001; Lorenz and DeWeaver, 2007 as simulated by the CMIP3/IPCC AR4 models as a consequence of increased greenhouse warming.

However, some models found a weakening or insignificant intensification of the midlatitude transient eddies in the warming world (e.g., Stephenson and Held, 1993; Bengtsson et al., 2006, 2009; Frierson et al., 2006; O'Gorman and Schneider, 2008). For example, O'Gorman and Schneider (2008) found an approximate linear scaling relationship between EKE and dry mean available potential energy (MAPE) using an idealized moist GCM. The EKE and MAPE have a localized maximum for the climate state similar to the present-day Earth and decrease for both colder and warmer climates. They attributed the reason to the competing effects of the changing factors such as the tropopause height, the meridional temperature gradient and the dry static stability in affecting the MAPE. Bengtsson et al. (2006) used the European Center/Hamburg Model Version 5 (ECHAM5) T63 coupled climate model and investigated the changes in lower tropospheric synoptic cyclones by tracking 850mb relative vorticity under the A1B scenario. They found that there is a minor reduction in the number of extratropical cyclones but no indication of more intense ones except for regional weakening or intensification associated with the poleward shift. Bengtsson et al. (2009) used a high-resolution T213 ECHAM5 forced with sea surface temperatures (SSTs) from the one in T63 version and found similar results during climate change except for larger regional changes and increased precipitation extremes. However, the dynamics were not explored in their study.

Furthermore, the stratosphere and its coupling with the troposphere have also been found to be important in determining the circulation response in the troposphere to global warming. Sigmond et al. (2004) studied the climate effects of middle-atmospheric and tropospheric CO_2 doubling separately using the ECHAM middle-atmosphere climate model with prescribed SSTs. They found strengthened and northward shifted NH tropospheric westerlies as a consequence of a uniform CO_2 doubling everywhere in the atmosphere and attributed this mainly to the middle-atmosphere CO_2 doubling. It is expected that the midlatitude storm tracks shift poleward as long with the tropospheric zonal jets. However, a recent study in Scaife et al. (2011) demonstrated a southward shifted winter storminess in an ensemble of high-resolution stratosphere models during climate change, which differs from the results in CMIP3/IPCC AR4 models. The change in storm activity in their study was found to be consistent with the southward shift of the maximum growth rate of baroclinic instability associated with an equatorward shifted polar westerlies; however, the dynamical mechanisms are not clear.

1.4 Outline

In Chapter 2 we analyze the changes in storm track location and intensity using the Geophysical Fluid Dynamics Laboratory (GFDL) CM2.1 global coupled climate model simulations in the doubling CO_2 scenario (A1B scenario). We examine the eddy statistics in a broad range of band-pass filtered climate variables and confirm the poleward and upward shift and intensification of the midlatitude storm activity. We also analyze the latitude-by-latitude energy budget for the current and future climate simulations and find that in response to global warming, more energy is gained within the tropics and subtropics while in the middle and high latitudes more energy is lost. This enhanced energy imbalance in the future climate requires larger atmospheric energy transports in the midlatitudes which are partially accomplished

by intensified storm tracks. The content of this chapter appears in Wu et al. (2010).

In Chapter 3 we investigate the transient step-by-step atmospheric adjustment to an instantaneous CO_2 doubling using the National Center for Atmospheric Research Community Atmospheric Model Version 3 (NCAR CAM3) coupled to a slab ocean model. Our results are expected to reveal the chain of sequence that occurs in the circulation adjustment process, in particular, what leads to the extensive warming in the middle and upper troposphere and what drives the poleward movement of the tropospheric jet streams and transient eddies. It is found that the broad warming expansion in the subtropical middle and upper troposphere is primarily dynamically-driven due to the intensification of transient eddy momentum flux convergence and resulting anomalous descending motion in this region. The poleward displacement of the midlatitude tropospheric jet streams occurs after the intensification of the subpolar westerlies in the stratosphere, which resembles the features of 'downward control'. Chapter 3 has been submitted to Journal of Climate and is under revision.

In Chapter 4 we further explore the dynamical mechanisms associated with the transient circulation adjustment process following Chapter 3. Based on the evolution of the zonal mean zonal wind anomaly in the extratropics, three stages are defined including an equatorward shift in polar jets in the stratosphere in Phase 1, a westerly acceleration in the stratosphere in Phase 2, and a 'downward propagation' of the westerly anomalies from the stratosphere to the troposphere along with a poleward displacement of the tropospheric jet streams featured in Phase 3. We find the transient process is important in setting up the equilibrium response afterwards and thus a thorough understanding of the transient adjustment is of necessity. Chapter 4 is in preparation for submission to Journal of Climate.

In Chapter 5 we extend the midlatitude storm track diagnoses to other CMIP3/IPCC AR4 coupled models (A1B scenario). The changes in band-pass filtered eddy statis-

tics averaged over 14 models show a consistent poleward and upward shift and intensification of the storm tracks in the future climate. The global atmospheric energy budget is also analyzed and the enhancement of energy imbalance in the atmosphere is robust for individual CMIP3/IPCC AR4 models. This study confirms the strong connection between the midlatitude storm track response and the global atmospheric energy budget in the future climate. As a consequence of increased transient eddy momentum flux convergence, the eddies tend to drive a descending motion anomaly in the subtropical troposphere and thus warm up the atmosphere adiabatically.

Finally we provide a brief summary for this thesis in Chapter 6 along with some future directions.

Chapter 2

Midlatitude Storm Track Response in A Warmer Climate in GFDL CM2.1 Coupled Climate Model

2.1 Introduction

Recent studies have indicated a poleward shift of the storm tracks and the midlatitude precipitation zone in the warming world that will lead to subtropical drying and higher latitude moistening (e.g., Yin, 2005; Held and Soden, 2006; Seager et al., 2007). In this chapter, we focus on one of the CMIP3/IPCC AR4 coupled models, the Geophysical Fluid Dynamics Laboratory (GFDL) CM2.1 model, and examine the changes in storm track location and intensity in a warmer climate and how they are related to the changes in the mean states and the atmospheric energy budget in the globe.

Yin (2005) pointed out the consistent poleward and upward shift of the midlat-

itude storm tracks, characterized by the band-pass filtered transient eddy kinetic energy, in 15 coupled IPCC AR4 GCMs. These features are accompanied by the enhanced warming in the tropical upper troposphere and the associated change in midlatitude baroclinicity, as well as the poleward shifts in surface wind stress and precipitation. This chapter focuses on the GFDL CM2.1 coupled climate model and extends the diagnosis of the midlatitude storm tracks to a broader range of climate fields such as the transient eddy momentum flux, variance of meridional velocity, meridional heat and moisture flux. The location and intensity of the midlatitude storm tracks is always related to the time mean state since the baroclinic instability is regarded as the dominant mechanism for the baroclinic eddy generation. It is expected that in response to increased greenhouse warming, the latitudinal temperature gradient in the upper troposphere increases while that near the surface reduces. It is not clear, based on the thermal response to global warming, how the midlatitude storm tracks will change. In addition, idealized experiments have indicated the importance of other factors such as water vapor and diabatic heating in affecting the midlatitude storm track dynamics in more complicated manners (e.g., Frierson et al., 2006, 2007). Hence it is worth exploring how the storm tracks will respond in a warmer climate and the major dynamical mechanisms involved.

The poleward energy transport in the midlatitudes is dominated by the atmospheric component which contains a significant contribution from the midlatitude storm tracks (Trenberth and Caron, 2001; Trenberth and Stepaniak, 2003). Held and Soden (2006) examined the hydrological cycle in the globe and found increased moisture transport in the extratropics as climate warms which is presumably carried out by the midlatitude storm track system. From the perspective of energy balance, it is expected that there are also changes in the radiative fluxes at the top of the atmosphere (TOA) and at the surface as well as changes in the surface sensible and latent heat fluxes. This allows a further exploration of the dynamics underlying

the storm track response as climate warms by connecting the midlatitude storm systems with the planetary energy balance.

Therefore, in this chapter we explore the following questions:

(1) What are the changes in the location and intensity of the midlatitude storm tracks as simulated by the GFDL CM2.1 coupled climate model in a warmer climate? How are they related to the changes in the time mean states?

(2) What are the changes in transient eddy energy transport? How are they related to the changes in the time mean states? How is the energy transport associated with the storm tracks connected to the global energy budget in the planet and the atmosphere?

The chapter is organized as follows. A brief description of the data and methods is given in Section 2.2. Section 2.3 presents the midlatitude storm track response in the warming world simulated by the GFDL CM2.1 model in both boreal summer and winter. The relevance of the changes in baroclinic eddy energy transports to the changes in baroclinic instability and the time mean states is give in Section 2.4, followed by the change in atmospheric and planetary energy budget in Section 2.5. Conclusions and discussions are presented in Section 2.6.

2.2 Data and Methods

The model output analyzed in this paper is from GFDL's CM2.1 global coupled climate model developed at the Geophysical Fluid Dynamics Laboratory (GFDL) of the National Oceanic and Atmospheric Administration (NOAA) in 2004 (Delworth et al., 2006). The resolution of the land (LM2.1) and the atmospheric (AM2.1) components is 2^o latitude $\times$ 2.5^o longitude with 24 vertical levels in the atmosphere structured in a hybrid coordinate. The dynamical core of AM2.1 uses the finite volume method from Lin (2004). This model has been used prominently for climate change experiments in the Intergovernmental Panel on Climate Change Fourth

Assessment Report (IPCC AR4) and the US Climate Change Science Program (US CCSP) reports. In a doubling CO_2 concentration scenario (A1B scenario), this model has a climate sensitivity of 3.4K in the global mean[1]. In addition we use the daily data from the National Centers for Environmental Prediction-National Center for Atmospheric Research (NCEP-NCAR) reanalysis (Kalnay and Coauthors, 1996) to validate the current climate transient eddy activity in the GFDL CM2.1 global climate model.

We use both the 20th and the 21st century simulations in this study. For the 21st century simulation, we use the daily data from the A1B scenario. To identify the climate change response, we compare the time mean of the late 21st century (years 2081-2100) with that of the latter half of the 20th century (years 1961-2000) and define the trend of climate change as the difference between the two periods. All transient eddy statistics computed in this study are based on band-pass filtered data.

2.3 Poleward Shift and Intensification of the Storm Tracks

The storm track activities are represented by several major band-pass filtered transient eddy statistics including the transient momentum flux ($\overline{u'v'}$) and the variance of eddy meridional velocity ($\overline{v'v'}$) at 250mb, the meridional sensible heat flux ($\overline{v'T'}$) and moisture flux ($\overline{v'q'}$) at 700mb. It has been demonstrated in Chapter 1 that the location and intensity of the midlatitude storm tracks is well simulated in the

[1]The GFDL CM2.1 model included both stratospheric ozone depletion in the 20th century simulation and ozone recovery in the A1B scenario simulation. Son et al. (2008) and Son et al. (2009) found that the recent poleward shift of the midlatitude westerly jet and the poleward expansion of the Hadley Cell in the Southern Hemisphere were partially forced by ozone depletion and will be likely to be weakened or even reversed (depending on models) by anticipated ozone recovery in the current century. Ozone change and its effect are almost negligible in the Northern Hemisphere.

GFDL CM2.1 model. This provides credentials in using this coupled model to examine the future projections of the midlatitude storm tracks and their dynamical mechanisms.

2.3.1 Horizontal structures

Figure 2.1 shows the 21st century trend in horizontal structures of various eddy statistics in DJF and JJA (colors) along with the 20th century climatology (black contours). The predominant features are the poleward and eastward (downstream) intensifications of the storm activity accompanied by a weak equatorward reduction for both the North Pacific and North Atlantic storm tracks. These lead to a slight poleward shift and a large poleward and eastward expansion of the storm tracks in the late 21st century. The response of the North Atlantic storm tracks is much stronger than that of the North Pacific one in both seasons. Take $\overline{v'T'}$ at 700mb as an example: there is an approximately 2^o poleward shift and $20\% - 30\%$ increase in maximum intensity in northern winter (Fig. 2.1(e)). At the entrance regions of the two storm tracks, i.e. off the eastern coasts of Asia and North America, there is a weakening of the transient meridional sensible heat flux due to reduction in land-sea temperature contrast and resulting reduction in surface upward sensible heat flux from the ocean, while the magnitude increases significantly in the downstream and exit regions stretching northeastward to the west coast of North America and into Western Europe (Fig. 2.1(e)). The transient moisture flux $\overline{v'q'}$ also intensifies in both seasons in the two storm track regions (Figs. 2.1$(g)(h)$). These changes in eddy activity largely agree with Hall et al. (1994). In the Southern Hemisphere, the intensification on the poleward flank of the storm track regions is significant and zonally symmetric in both seasons.

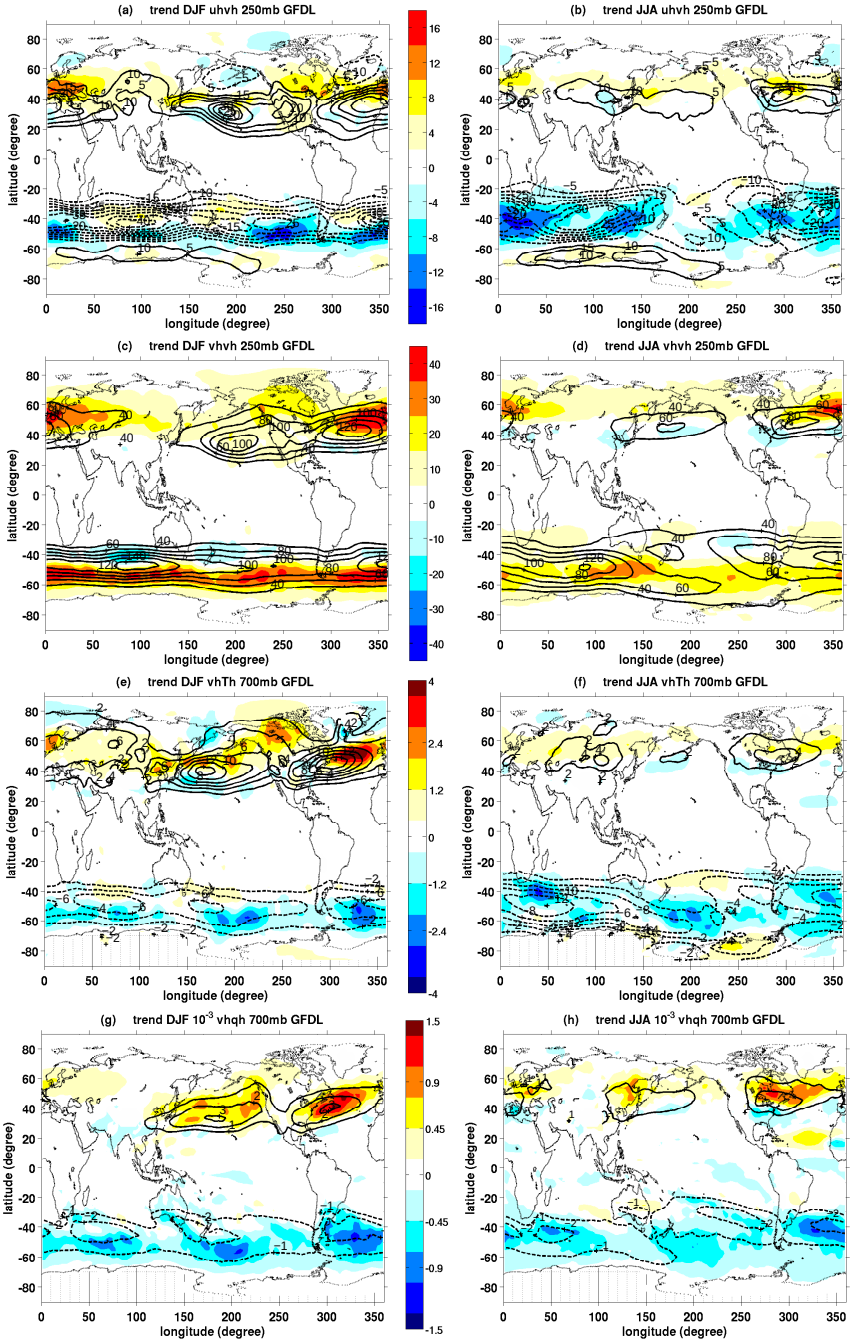

Figure 2.1: Global warming trends in $(a)(b)$ $\overline{u'v'}$ at 250mb, $(c)(d)$ $\overline{v'v'}$ at 250mb, $(e)(f)$ $\overline{v'T'}$ at 700mb and $(g)(h)$ $\overline{v'q'}$ at 700mb, in DJF and JJA, respectively, from the GFDL CM2.1 model simulations, plotted in colors, with the 20th century climatology in contours. Contour intervals are 5 m^2/s^2 for $(a)(b)$, 20 m^2/s^2 for $(c)(d)$, 2 $m/s \cdot K$ for $(e)(f)$ and 1×10^{-3} m/s for $(g)(h)$.

2.3.2 Zonal mean structures

The zonal mean eddy statistics are shown in Fig. 2.2 with the 20th century climatology in contours and the 21st century changes in colors. The consistent poleward shift and intensification on the poleward flank of all the eddy statistics can be seen in both seasons in both hemispheres. In some eddy statistics, there is an upward shift as well. Furthermore, the increased meridional moisture transport in the future climate is consistent with the poleward shift and intensification of the midlatitude precipitation zone and the resulting poleward expansion and drying of the subtropical dry zones (e.g., Seager et al., 2007). It is worth noting that the trend in zonal mean meridional heat transport in southern winter (JJA) is a local intensification rather than a poleward intensification and expansion (Fig. 2.2(f)).

2.4 Relating Changes in Baroclinic Eddy Energy Transports to Changes in Instability and the Mean State

The maximum intensity in synoptic eddy activity in the midlatitudes has long been related to the existence of strong baroclinic zones and the associated baroclinic instability which converts available potential energy of the time mean flow to eddy kinetic energy (e.g., Lorenz, 1955; Eady, 1949; Charney, 1947). One of the measures of linear baroclinic instability is the maximum Eady growth rate, which has been mathematically simplified and shown to be a useful estimate of the growth rate of the most rapidly growing instability in a range of baroclinic instability problems (Lindzen and Farrell, 1980). Hoskins and Valdes (1990) used the parameter to quantify the geographical location and intensity of the storm tracks.

Here we first apply the maximum Eady growth rate to determine the changes in

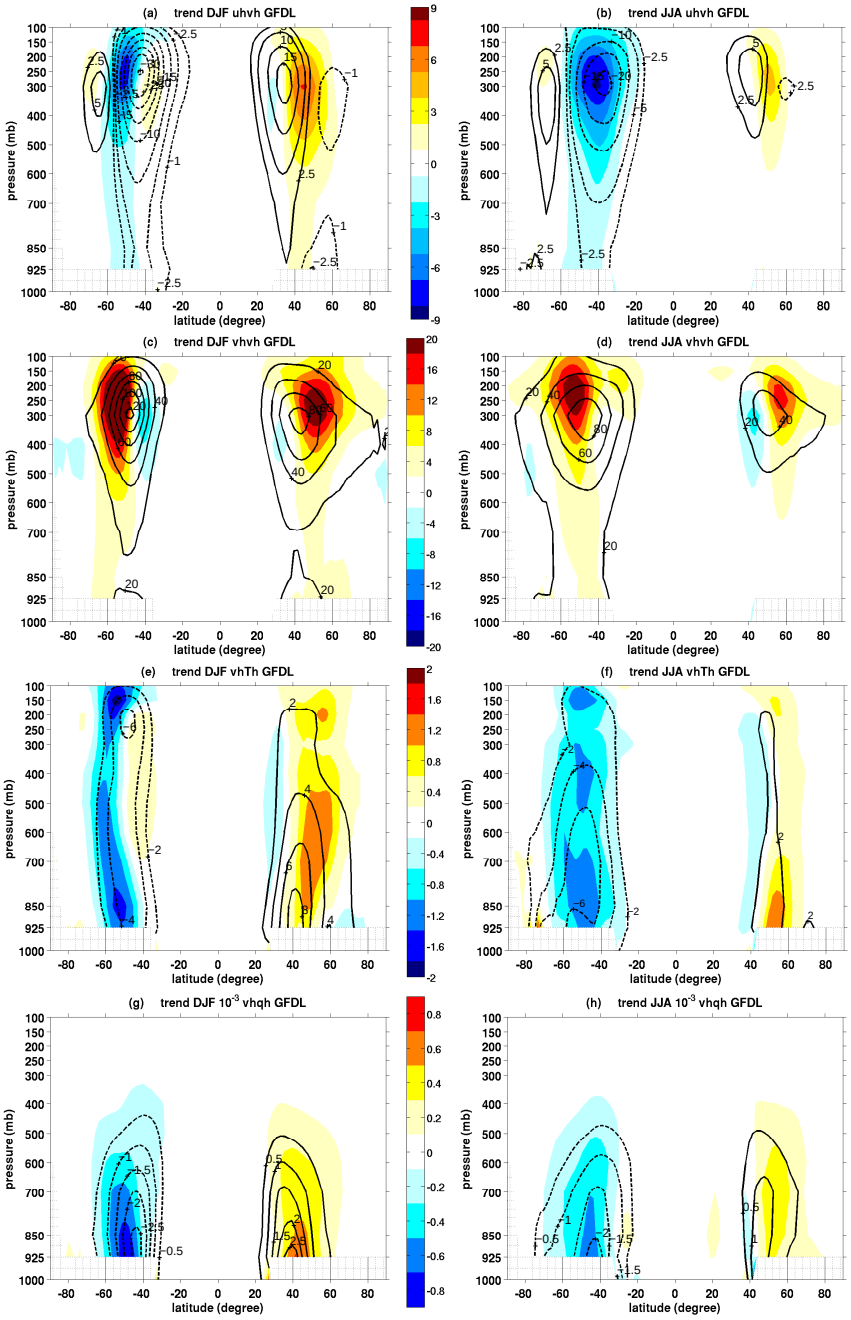

Figure 2.2: Same as Figure 2.1 but for the 21st century trend in zonal mean eddy statistics as a function of latitude and pressure level (mb), i.e. $(a)(b)$ $\langle\overline{u'v'}\rangle$, $(c)(d)$ $\langle\overline{v'v'}\rangle$, $(e)(f)$ $\langle\overline{v'T'}\rangle$ and $(g)(h)$ $\langle\overline{v'q'}\rangle$, in DJF and JJA, respectively, plotted in colors, with the 1961-2000 climatology in contours.

baroclinicity of the mean states in the late 21st century from that in the latter half of the 20th century as simulated in the GFDL CM2.1 model. A simple approximate result for the maximum growth rate of baroclinic instability is given by

$$\sigma_D = 0.31 g \frac{1}{N} \frac{1}{T} |\frac{\partial \bar{T}}{\partial y}| \tag{2.1}$$

(Lindzen and Farrell, 1980), where N is the Brunt-Vaisala frequency, a measure of static stability. Figures 2.3(a)(b) show the 21st century trend in zonal mean tropospheric temperature $\langle \bar{T} \rangle$ (colors) as well as the 20th century climatology (contours). It shows a strong upper tropospheric warming in both seasons and an enhanced Arctic warming in northern winter. The tropical upper tropospheric warming is caused by enhanced tropical convection which transports heat trapped by the additional greenhouse gases upward with the tropical atmosphere retaining a moist adiabatic lapse rate under a warmer condition. The large warming located in the Arctic in winter, where the ice-albedo feedback is weak, is largely a result of increased CO_2 radiative heating and large atmospheric static stability concentrating the warming at low levels (e.g., Hansen et al., 1984; also see discussions in Chapter 3). The associated climatology and trend in zonal mean meridional temperature gradients $|\frac{\partial \langle \bar{T} \rangle}{\partial y}|$ is given in Figs. 2.3$(e)(f)$. Strong gradients of temperature can be seen in the midlatitudes, particularly in the vicinity of the subtropical jet (shown in Figs. 2.3$(c)(d)$). The trend in both seasons in both hemispheres demonstrates a poleward shift and intensification in midlatitude meridional temperature gradients. The one exception is in the lower troposphere in northern winter when the warming at the Arctic winter surface leads to a reduced zonal mean meridional temperature gradient there[2]. Figures 2.3$(g)(h)$ represent the climatology and trend of the static stability in the atmosphere. The whole lower and middle troposphere becomes more statically stable except for the middle and high latitudes in northern winter.

[2]The zonal mean meridional temperature gradient reduces despite an increase in temperature gradient in the North Atlantic region.

The rising subtropical tropospheric static stability has been related to the poleward expansion of the Hadley Cell by Lu et al. (2007). The reduced static stability in the middle and high latitudes in northern winter is again due to the strong warming near the surface. The jet stream in a warmer climate tends to shift poleward and upward and intensify on the poleward and upward flank of the climatological jet in both seasons in both hemispheres (Figs. 2.3$(c)(d)$). This change in the jet stream is consistent with that in the storm tracks. These changes are representative of the changes in the time-mean states of many GCMs with increased greenhouse gases (e.g., Meehl et al., 2007b).

2.4.1 Zonal mean structures of baroclinic instability

As the dry Eady growth rate is determined by both the meridional temperature gradient and static stability, future changes in both terms will impact the change in the baroclinic instability of the time-mean flow. The zonal mean of the dry Eady growth rate is shown in Figs. 2.4$(a)(b)$ for both DJF and JJA. The climatology maximizes in the midlatitudes and is stronger in the winter hemisphere due to stronger meridional temperature gradients. The change in the dry Eady growth rate follows that in the meridional temperature gradient, i.e. a poleward shift and an intensification on the poleward flank in the middle and upper troposphere of the midlatitudes except for the lower troposphere in northern winter. The contribution from the static stability according to the dry Eady growth rate is small, but the rising tropospheric static stability south of 40^oN helps to stabilize the subtropical jet streams on the equatorward flank whereas the reduced static stability north of 40^oN acts to enhance the instability of the jet streams on the poleward flank, which would assist a poleward shift of the storm tracks. Therefore, as can be seen in Figs. 2.4$(a)(b)$, the poleward shift and enhancement of the dry Eady growth rate in the midlatitudes of both hemispheres in both seasons (except for the lower

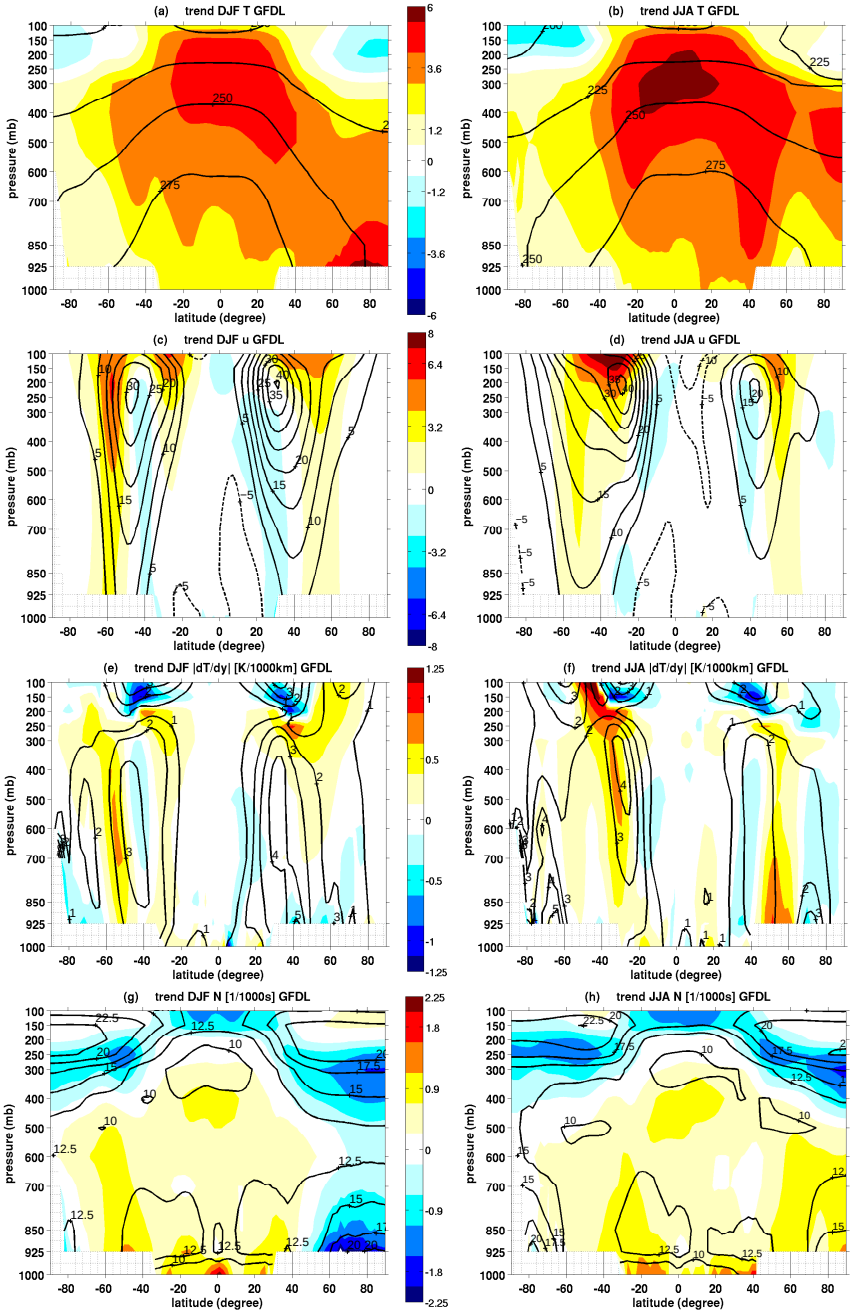

Figure 2.3: Same as Figure 2.1 but for the 21st century trend in zonal mean climatological states, i.e. $(a)(b)$ $\langle\overline{T}\rangle$, $(c)(d)$ $\langle\overline{u}\rangle$, $(e)(f)$ $|\frac{\partial\langle\bar{T}\rangle}{\partial y}|$, and $(g)(h)$ $\langle\overline{N}\rangle$, in DJF and JJA, respectively, plotted in colors, with the 20th century climatology in contours. Contour intervals are 225 K for $(a)(b)$, 5 m/s for $(c)(d)$, 1 K/1000km for $(e)(f)$ and 2.5/1000 s^{-1} for $(g)(h)$.

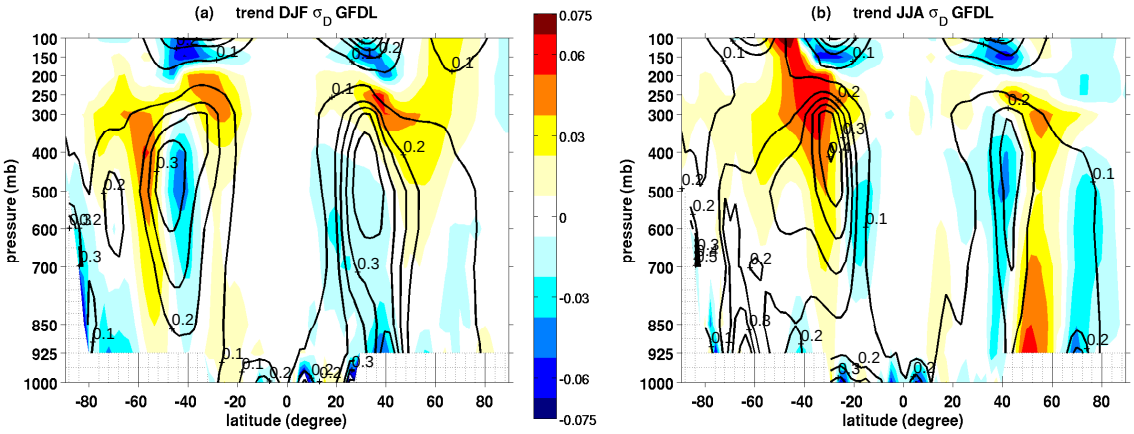

Figure 2.4: Same as Figure 2.1 but for the 21st century trend in zonal mean Eady growth rate σ_D in (a) DJF and (b) JJA, in colors, with the 20th century climatology in contours. Contour intervals are 0.5 day^{-1}. Units are day^{-1}.

troposphere in northern winter) fully supports the storm track changes. The results in Figs. 2.4$(a)(b)$ confirm the relevance of the changing characteristics of baroclinic instability in driving the storm track changes. The results further indicate that eddies are influenced by the baroclinicity in the upper troposphere rather than the surface instability, as the enhancement of the instability growth rate in the upper troposphere from 225mb to 550mb well corresponds to the storm track response in this region in terms of $\langle\overline{u'v'}\rangle$ and $\langle\overline{v'v'}\rangle$. However, it is not clear what role the decrease in instability growth rate in the lower troposphere plays in explaining the storm track response in northern winter.

2.4.2 Eddy transfer and mean state gradients

In order to explain that the transient eddy sensible heat transport in the middle latitudes of both hemispheres in both seasons increases as climate warms (Figs. 2.2$(e)(f)$) despite the decreased temperature gradients in the lower troposphere in northern winter, we apply mixing length theory in this section to attribute the increasing transient eddy energy transfer to eddy properties and mean state gradients

in boreal winter.

Based on the theoretical work of Charney (1947) and Eady (1949), Green (1970) proposed a theory for the large-scale eddy transfer, based on eddy mixing, by relating eddy transfer properties to eddy motion and mean gradients as follows:

$$\overline{v'm'} = k|v'||m'| = k|v'|(-L_{\text{mix}}\frac{\partial \overline{m}}{\partial y}) = -D\frac{\partial \overline{m}}{\partial y} \tag{2.2}$$

where $v'm'$ is the meridional transport of any conserved property m, D is defined as the eddy diffusivity, i.e. $D = kL_{\text{mix}}|v'|$ with k the correlation coefficient between v' and m', L_{mix} the mixing length scale, and $|v'|$ and $|m'|$ rms amplitudes of eddy velocity and m, and $\frac{\partial \overline{m}}{\partial y}$ is the time mean state gradient. The complete form in Green (1970) for the transfer in meridional-vertical section has additional contribution from vertical mixing which is neglected here. We apply Eq.(2.2) to the conserved quantity moist static energy, band-pass filtered transients and zonal mean fields (brackets denoting zonal averages are neglected here) and compute k and L_{mix} by definition, i.e. $k = \frac{\overline{v'm'}}{|v'||m'|}$ and $L_{\text{mix}} = \frac{|m'|}{-\frac{\partial \overline{m}}{\partial y}}$ for both the 20th and 21st century simulations. Here moist static energy (MSE) is defined as $m = C_pT + \Phi + L_eq$ with C_p the specific heat capacity for the atmosphere, Φ the geopotential height and L_e the latent heat of evaporation. Because of the quasi-geostrophic nature of eddies, the zonally averaged eddy potential energy transfer can be neglected and the transient eddy MSE transport can be written as $\overline{v'm'} \approx C_p\overline{v'T'} + L_e\overline{v'q'}$. It is noted that the original intention of Eq.(2.2) is for parameterizing eddy transfer using large-scale quantities. Our study here, however, is using Eq.(2.2) as a diagnostic tool for understanding the change in transient eddy energy transfer ($\overline{v'm'}$) in terms of correlation coefficient (k), transient eddy velocity (v'), mixing length scale (L_{mix}) and mean state gradients ($\frac{\partial \overline{m}}{\partial y}$).

Therefore, the change in eddy MSE transport can be written as

$$\begin{aligned}
\underbrace{\Delta(\overline{v'm'})}_{(a)} &= \Delta\{kL_{\rm mix}|v'|(-\frac{\partial\overline{m}}{\partial y})\} \\
&\approx \underbrace{\Delta(k)L_{\rm mix}|v'|(-\frac{\partial\overline{m}}{\partial y})}_{(c)} + \underbrace{k\Delta(L_{\rm mix})|v'|(-\frac{\partial\overline{m}}{\partial y})}_{(d)} + \underbrace{kL_{\rm mix}\Delta(|v'|)(-\frac{\partial\overline{m}}{\partial y})}_{(e)} \\
&+ \underbrace{kL_{\rm mix}|v'|\Delta(-\frac{\partial\overline{m}}{\partial y})}_{(f)}
\end{aligned} \tag{2.3}$$

which decomposes the impact of the change in correlation coefficient (term (c)), mixing length scale (term (d)), eddy velocity (term (e)) and mean MSE gradient (term (f)) on the change in total transient eddy MSE transport. Figure 2.5(a) shows the DJF change in transient eddy MSE transport for the late 21st century (colors), with the 20th century climatology shown in contours. It illustrates an enhanced poleward transient eddy MSE transport in both hemispheres. The sum of terms (c)-(f) in Eq.(2.3) is shown in Fig. 2.5(b) in contours, with the 21st century trend in $\overline{v'm'}$ in colors. The agreement between contours and colors in Fig. 2.5(b) indicates that the nonlinear contributions ignored on the right hand side of Eq.(2.3) are insignificant.

When separating the total change in $\overline{v'm'}$ into contributions from k, $L_{\rm mix}$, $|v'|$ and $\frac{\partial\overline{m}}{\partial y}$ (Figs. 2.5(c)-(f)), it is found that all of the terms contribute significantly. The colors in Figs. 2.5(c)-(f) indicate the total change as shown in Fig. 2.5(a). The most dominant contribution in the midlatitudes of the Northern Hemisphere comes from the increasing correlation between transient eddy velocity and eddy MSE while in the Southern Hemisphere it is the enhancement of mean state gradients. As shown in Fig. 2.5(f), the reduction in mean energy gradient in the lower-troposphere of the middle and high northern latitudes (caused by a

decreased meridional temperature gradient dominating over a specific humidity gradient increase) would reduce the poleward energy transport by the storm tracks. In contrast, in the midlatitudes of the Southern Hemisphere and the mid-troposphere in the Northern Hemisphere, the increase in mean energy gradient would lead to an increase in transient eddy energy transport and this dominates the total in these regions. The contribution from the other three terms in general is positive to the total. In particular, in the lower troposphere of the midlatitude Northern Hemisphere, it is mainly the increasing correlation coefficient, and to a lesser extent, the increasing eddy velocity and mixing length scale that overwhelms the decreasing contribution from the mean gradient and leads to the intensified transient eddy energy transport.

The question to be addressed in the following is what causes the increasing correlation coefficient between transient eddy motion and eddy energy and the increasing mixing length scale as climate warms. It is found that the wave packets in one-point correlation maps (Chang, 1993) become longer in the lower troposphere in the Northern Hemisphere in future projections (not shown), which implies more persistent wave structures and increasing correlation over greater distances. This can also be viewed through a cross-spectral analysis of the lower tropospheric eddy MSE transfer as in Randel and Held (1991). Figure 2.6 shows a zonal wavenumber-frequency contour diagram for $\frac{1}{C_p}\overline{v'm'}$ at 700mb, averaged over the midlatitudes between 40^oN and 60^oN in DJF, with the 20th century climatology in black contours and the 21st century trend in red. The climatological cross-spectrum shows a strong covariance for eastward propagating waves of zonal wavenumber 7 and with a time scale of 4-5 days. In future projections, there is an increase in spectral power in part of the spectrum related to longer wavelengths and longer time scales. This intensification in smaller zonal wavenumbers is also true for the lower-level transient eddy velocity variance (not shown) and the upper troposphere transient

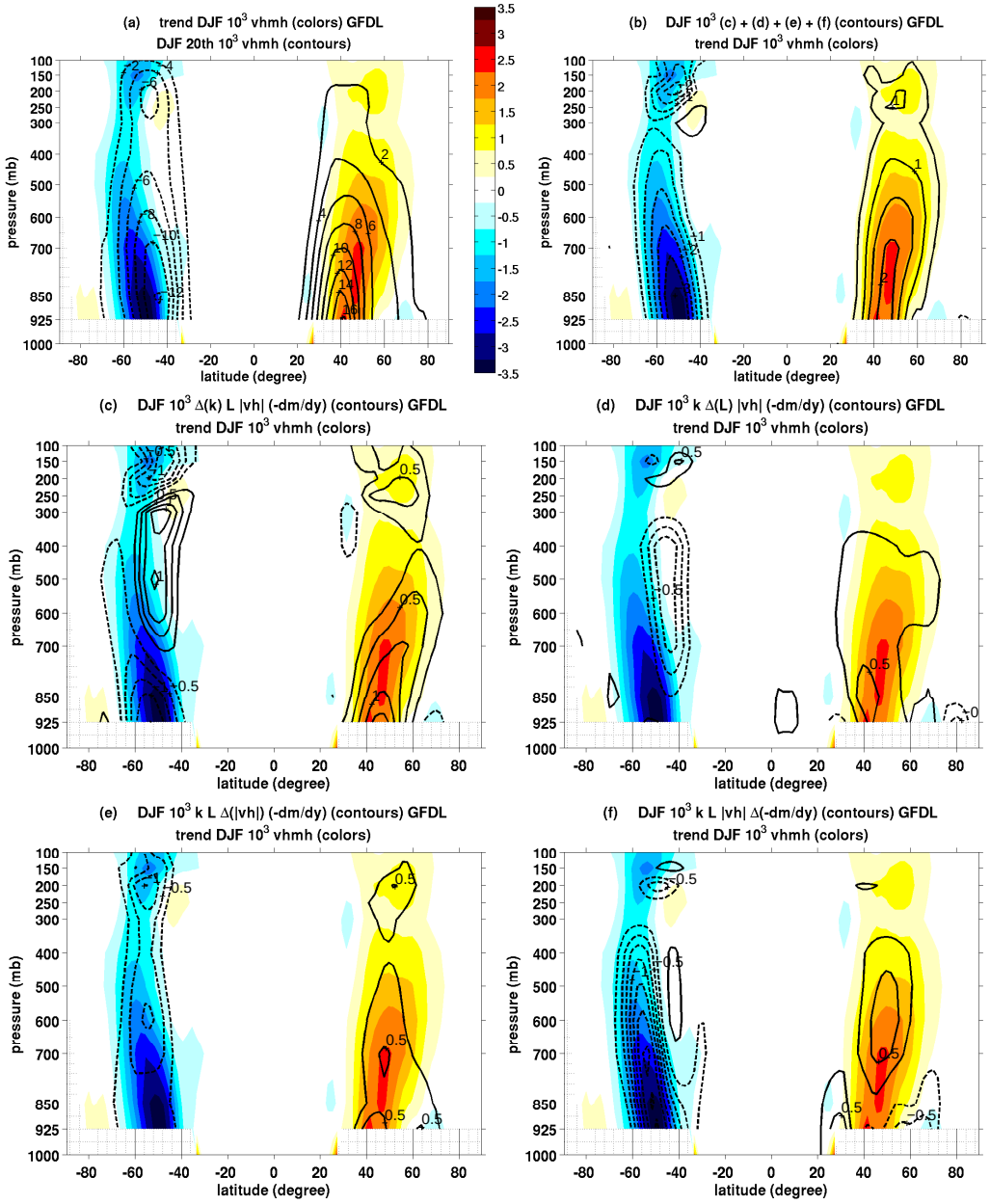

Figure 2.5: Shown in contours are (a) the 20th century climatology in band-pass filtered transient meridional eddy moist static energy (MSE) transfer $\langle\overline{v'm'}\rangle$; (b) Sum of (c), (d), (e) and (f) as indicated by the mixing length theory; Changes in eddy MSE transfer caused by (c) the change in correlation coefficient k between eddy motion v' and eddy MSE m', (d) the change in mixing length scale $L_{\rm mix}$, (e) the change in eddy intensity $|v'|$, and (f) the change in mean MSE gradients. Contour intervals are 2×10^3 m/s $\cdot$ J/kg for (a), 0.5×10^3 m/s $\cdot$ J/kg for (b) and 0.25×10^3 m/s $\cdot$ J/kg for (c)-(f). Colors in (a)-(f) are the 21st century trend in $\langle\overline{v'm'}\rangle$. Units are m/s $\cdot$ J/kg.

eddy momentum flux (Chen et al., 2008). Kidston et al. (2010) also found a robust increase in eddy length scale in the A2 simulations (the CO_2 concentration reaches about 800 ppmv at the end of the 21st century) among the CMIP3/IPCC AR4 climate models. Previous studies have shown that the growth rate of baroclinic eddies can depend on the basic state vertical shear and stratification in the stratosphere and the tropopause height (Harnik and Lindzen, 1997; Vallis, 2006; Wittman et al., 2007; Kunz, 2008), all of which are expected to change under global warming. Rivire (2011) emphasized the role of enhanced upper-tropospheric baroclinic instability in the poleward shift of the jet streams via changes in eddy length scale and anticyclonic/cyclonic wave breaking in the global warming scenario. In his study, the baroclinic instability was examined in a three-layer f-plane quasi-geostrophic model. It was found that the enhanced upper-level baroclinic instability leads to increased destablization (stablization) for long (short) waves. Therefore, in a warmer climate longer waves are expected to become more baroclinically unstable, which is attributed to the increase in upper tropospheric baroclinic instability and the rise in tropopause height.

In summary, although the midlatitude lower-level temperature gradient reduces in northern winter, the transient eddy poleward energy transfer intensifies as climate warms. As suggested by the mixing length theory, it mainly generates from the contributions of the increasing coherence between transient eddy motion and eddy energy, and to a lesser extent, the increasing eddy velocity and eddy mixing length scale, sum of which overwhelms the reduced mean state gradients.

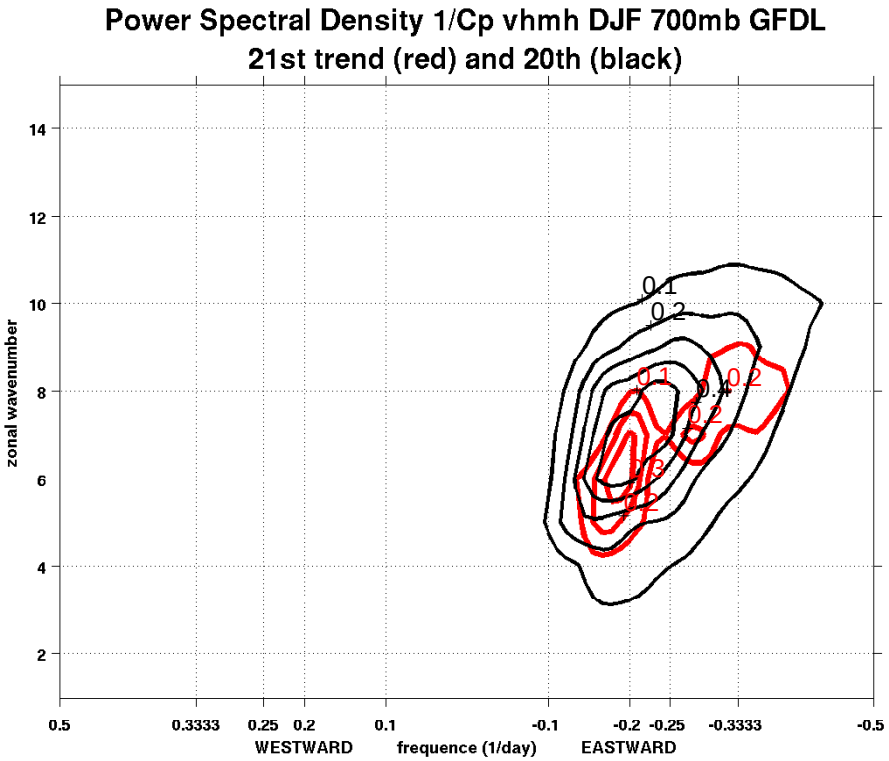

Figure 2.6: The global warming trend in transient eddy poleward moist static energy (MSE) transfer (normalized by C_p), i.e. $\frac{1}{C_p}\langle\overline{v'm'}\rangle$, as a function of zonal wavenumber and frequency, at 700mb, averaged over the midlatitudes between 40^oN and 60^oN, in DJF, plotted in red contours, with the 20th century climatology in black contours. Contour intervals are 0.1 m/s $\cdot$ K $\cdot$ day. Positive and negative frequency correspond to westward and eastward propagation, respectively.

2.5 Links Between Changes in Storm Tracks and Changes in the Energy Transports

The latitudinal distribution of the radiation budget at the top of the atmosphere (TOA) balances the meridional divergence of atmospheric and oceanic energy transports. In the future climate, the distribution and amplitude of the energy fluxes at the TOA and at the surface, including both radiative and non-radiative fluxes, is expected to change. The midlatitude storm tracks, as part of the global large-scale general circulation, are expected to change as well. In this section, we study the mechanisms for the future storm track projections from the perspective of the energy budget of the atmosphere. By combining the total atmospheric energy transport with the radiative fluxes at the TOA and at the surface, and the surface sensible and latent heat fluxes, a diagnosis of the latitude-by-latitude energy budget for the future climate can be performed and compared with that for the current climate.

Hall et al. (1994) examined the total zonal mean poleward energy transport in both control and doubled carbon dioxide experiments by using the UK Meteorological Office GCM with a mixed-layer slab ocean model and found slight differences. The planetary energy budget requirements are satisfied by this difference which is mainly due to increased latent heat transport by transient eddies. Here we examine the changes in atmospheric energy transport in the GFDL CM2.1 model and, building on Hall et al. (1994), link these to changes in the TOA radiative and surface fluxes.

Figure 2.7 (top) gives a summary of the global energy balance and changes due to global warming. The values inside the arrows are the global annual mean for years 1961-2000 from the GFDL CM2.1 model simulations and the values outside the arrows show the corresponding changes from the 20th to the 21st century (to

be discussed later). The positive or negative signs of relative changes are with respect to the climatological direction of energy fluxes. The model's simulations of these radiative and non-radiative fluxes in the current climate compare reasonably well with observations (e.g., Trenberth et al., 2001, 2009). Figure 2.7 (bottom) shows the corresponding latitudinal distribution of the annual and zonal mean energy fluxes, where the net energy flux into the atmosphere (F_{atm}^{net}) is defined as $F_{atm}^{net} = R_{TOA} - R_{surface} + SH + LH$. The top of the atmosphere radiation (R_{TOA}) shows a net gain of solar radiation in the tropics and subtropics and a net loss of terrestrial radiation in the high latitudes. The net radiative flux at the surface ($R_{surface}$) is almost everywhere positive downward, indicating a net gain of radiation by the surface in the form of net solar and terrestrial radiation. It is balanced by the loss of energy into the atmosphere in terms of upward sensible (SH) and latent heat fluxes (LH). The net energy flux into the atmosphere maximizes in the tropics and has a local minimum around the equator due to the presence of strong ocean heat divergence and suppressed surface latent heat flux (Seager et al., 2003b). The seasonal energy fluxes are similar except for hemispheric shifts (not shown).

In response to global warming it is expected that each component of the energy fluxes will change as a consequence of increased greenhouse gases. Figure 2.8 shows the zonal mean trend from the 20th to the 21st century of all the energy fluxes. Figure 2.9, as an aid to interpretation, shows the 21st century trend in zonal mean precipitation and total cloud fraction. As projected by the GFDL CM2.1 model simulations, the downward radiative flux at the TOA (R_{TOA}) increases by about 2 W/m^2 in the tropics and subtropics between 40^{o}S and 40^{o}N in DJF (Fig. 2.8(a)). This is caused by a reduction in solar reflection (except equatorial deep convective region) due to reduced cloud cover (shown in Fig. 2.9(a)) and a reduction in outgoing longwave radiation (OLR) around the equator due to enhanced deep convection. On the contrary, R_{TOA} decreases at the middle and high latitudes in

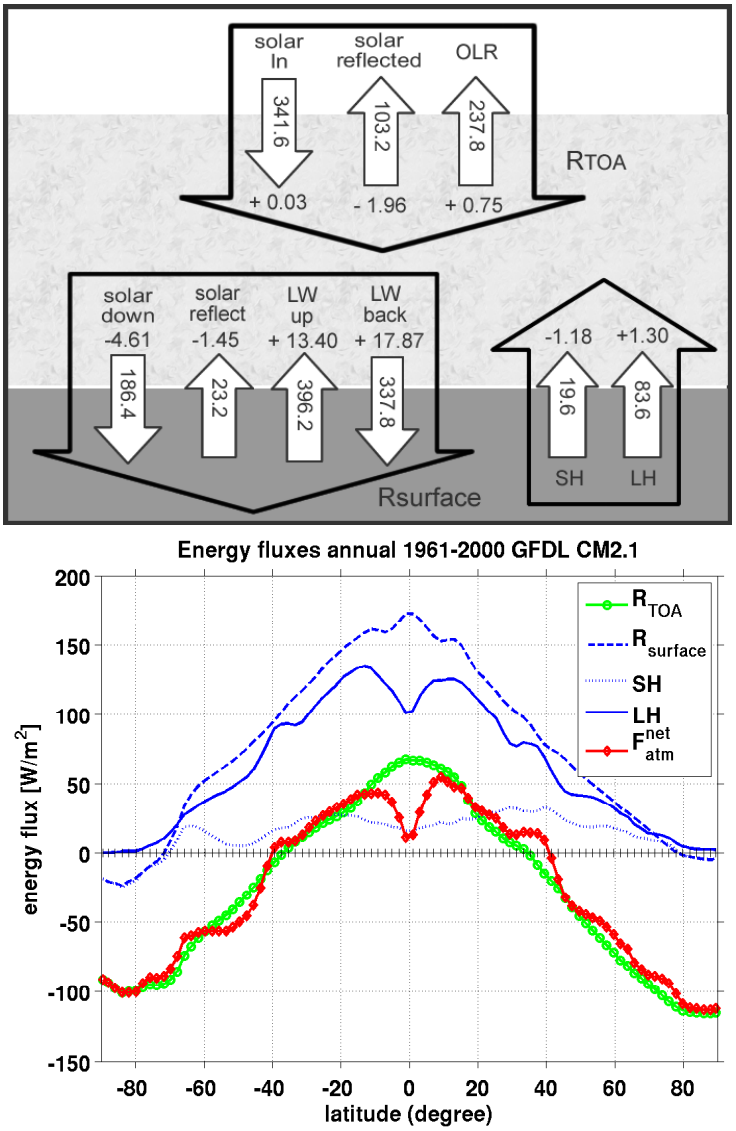

Figure 2.7: (Top) Summary of the global energy balance illustrating the notation and direction of energy fluxes. At the top of the atmosphere (TOA), the net downward radiative flux R_{TOA} (positive downward) is made up of the incoming and reflected solar radiation and the outgoing longwave radiation (OLR). The surface flux is made up of the net radiative flux $R_{surface}$ (positive downward), the surface sensible heat flux SH (positive upward) and the surface latent heat flux LH (positive upward). The surface radiative flux is comprised of the downward solar radiation, the surface reflected solar radiation, the surface emitted longwave radiation, the longwave radiation emitted back from the atmosphere. The values inside and outside the arrows are the global annual mean for years 1961-2000 and relative changes from years 1961-2000 to 2081-2100, respectively, from the GFDL CM2.1 model simulation. Positive or negative signs in relative changes are with respect to the climatological direction of energy fluxes. (Bottom) Annual and zonal mean energy fluxes for years 1961-2000. It comprises R_{TOA}, $R_{surface}$, SH, LH and the net energy flux into the atmosphere F_{atm}^{net}. Units are W/m^2.

both hemispheres. In the Northern Hemisphere, the reduction in R_{TOA} comes from the increased OLR which follows the surface terrestrial radiation, whereas in the Southern Hemisphere it is the increased cloudiness and resulting increased solar reflection that reduces the TOA radiation gain. This increase in radiative gain in the tropics and subtropics and radiative loss in the middle and high latitudes is an important factor in determining the change in atmospheric poleward energy transport (to be discussed).

At the surface, the downward radiative flux is expected to increase almost everywhere on Earth because of the increased downward longwave emission from the atmosphere but is offset at the middle and high latitudes of the summer hemispheres where increased cloudiness reflects more solar radiation to space. A notable change in surface non-radiative fluxes is the reduction in both upward sensible and latent fluxes in both seasons over the Southern Ocean. This is consistent with the results of Russell et al. (2006) who used the same model to show increased ocean heat uptake in response to increased greenhouse gases via increased ocean upwelling (forced by stronger westerlies), which reduces the air-sea temperature and humidity gradients. In addition, it is interesting to note that the partition between surface sensible and latent heat fluxes in response to global warming is seasonally and geographically dependent in the Northern Hemisphere. In northern winter, the evaporation over the ocean in general (except the North Atlantic ocean) increases as a result of increased greenhouse effect whereas the upward sensible heat flux reduces up to 70^oN due to reduced land-sea temperature contrast and increases north of 70^oN because of the sea ice melting (Fig. 2.8(b)). In northern summer, the increased subtropical drying (e.g., Gregory et al., 1996; Held and Soden, 2006; Seager et al., 2007) tends to increase the upward sensible heat flux and decrease the evaporation over land, especially around the latitude band of 40^oN. In contrast, there is a reduction in sensible heat flux and an increase in latent heat flux over

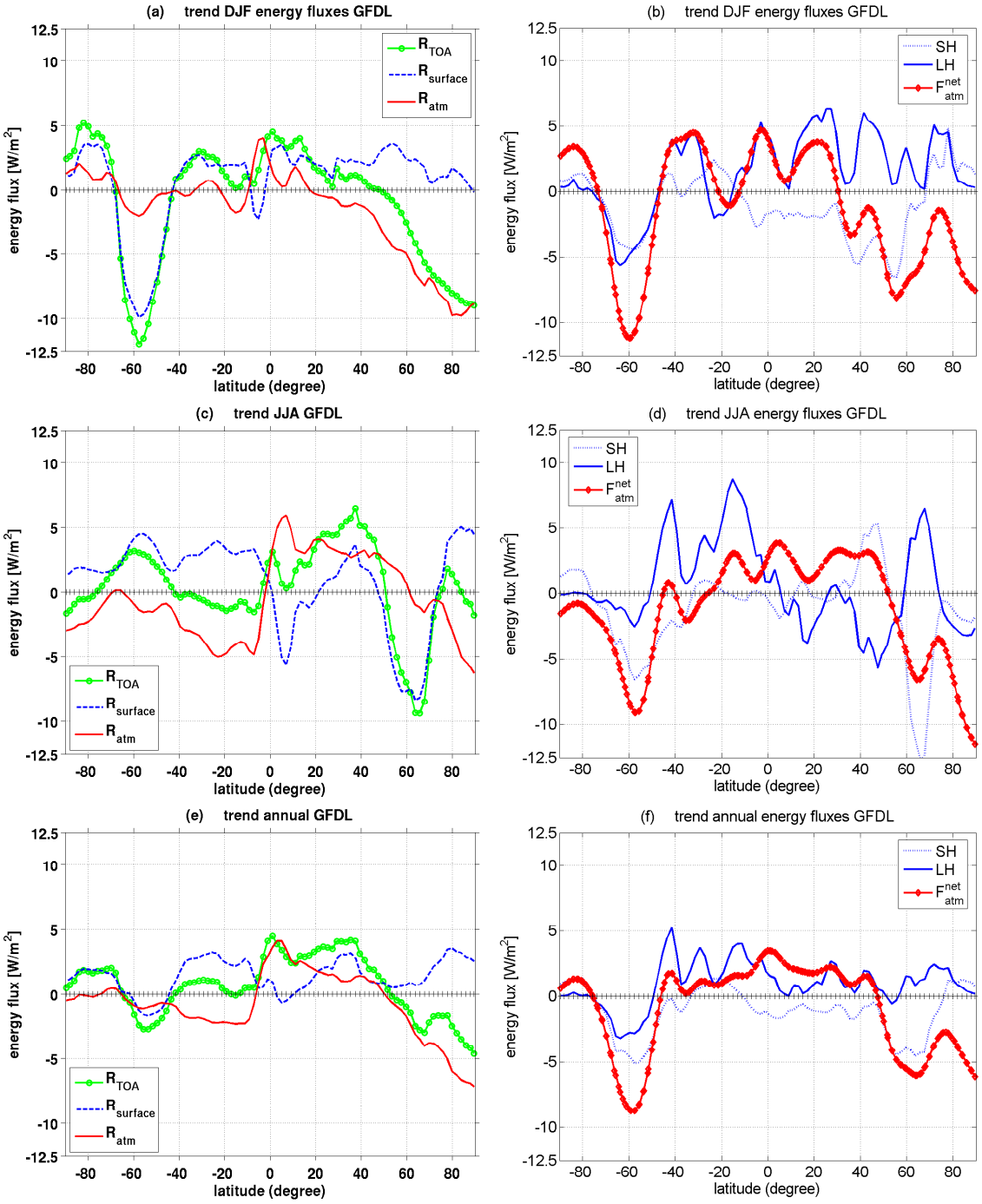

Figure 2.8: Global warming trend in zonal mean energy fluxes, i.e. $(a)(c)(e)$ R_{TOA}, $R_{surface}$ and the net radiative flux into the atmosphere R_{atm}, and $(b)(d)(f)$ SH, LH and the net energy flux into the atmosphere F^{net}_{atm}, in DJF, JJA and annual mean, respectively. Units are W/m^2. A cubic smoothing spline has been applied to the trend of F^{net}_{atm} to remove small scale noises.

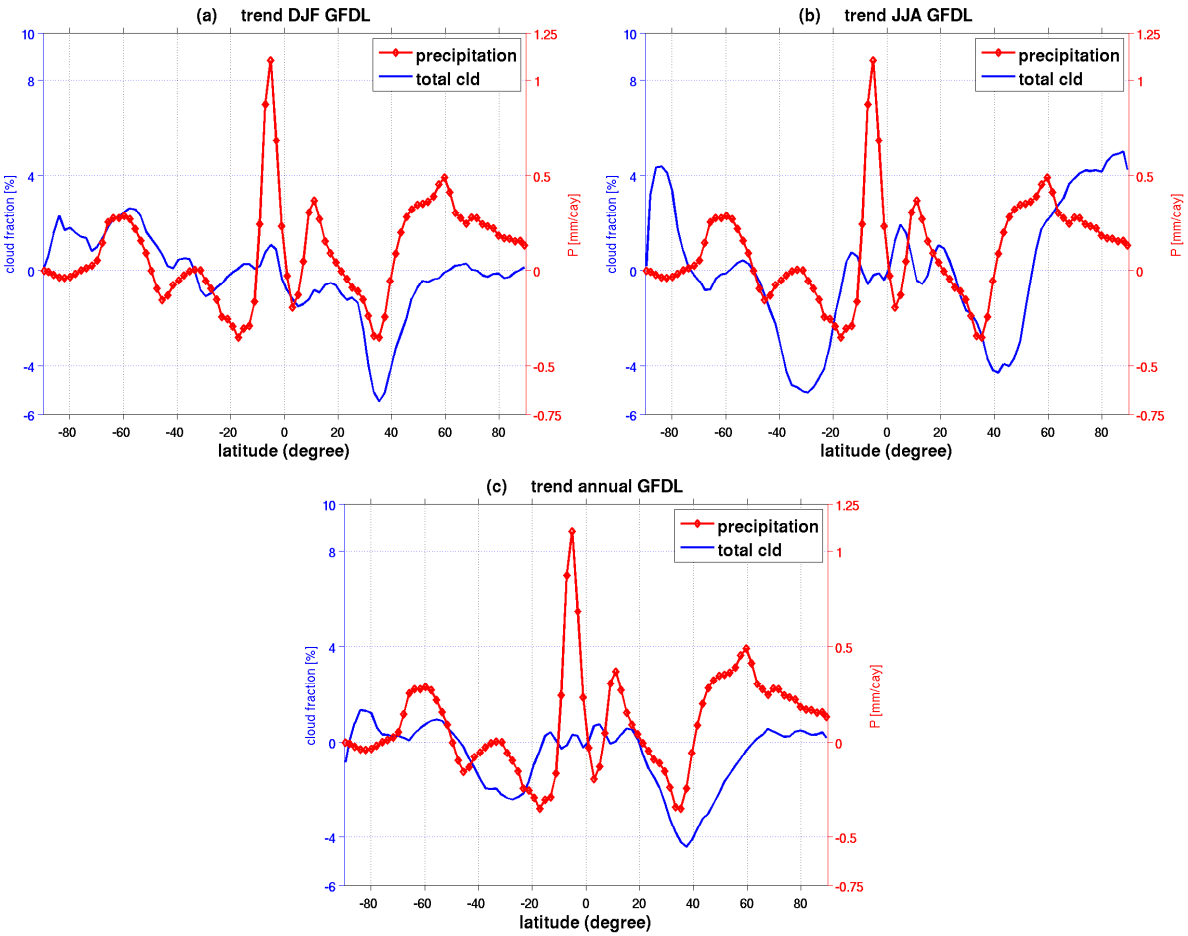

Figure 2.9: Global warming trend in zonal mean total cloud fraction (in unit of %) and precipitation (in unit of mm/day), in (a) DJF, (b) JJA and (c) the annual mean, from the GFDL CM2.1 model simulations.

land between about 60^oN and 80^oN because of moistening of continental land masses (Fig. 2.8(d)).

As a consequence of the TOA radiation, the surface radiation, and sensible and latent heat fluxes, the net energy flux into the atmosphere is found to increase within the tropics and subtropics between about 40^oS and 40^oN and decrease elsewhere in both seasons (Figs. $2.8(b)(d)(f)$) [3]. Consequently the gradient between the energy surplus in the tropics and subtropics and the energy deficit at the middle and high latitudes becomes greater in the future climate independent of season. Furthermore, the enhanced energy imbalance in the future climate is primarily radiative driven. To achieve an equilibrium state, the total atmospheric energy transport from the equator to the poles must increase. This can be accomplished, all or in part, by intensified transient eddy heat transport.

2.5.1 Changes in the atmospheric energy transport

In this section we quantitatively measure the amount of increased energy transport in the atmosphere required by the energy budget change and examine how it is partitioned among the mean meridional circulation and transient and stationary eddies. We will demonstrate that the increased atmospheric energy transport is concentrated in mid-latitudes and is partially accomplished by the intensified transient eddies, particularly the storm tracks in both seasons in both hemispheres.

The total atmospheric energy transport was first estimated based on the energy budget of the atmosphere as follows:

$$S_A = F_{atm}^{net} - \nabla \cdot F_A \tag{2.4}$$

where S_A is the energy storage rate in the atmosphere and F_A is the total atmospheric energy transport. Although the atmospheric heat content increases during

[3] In order to pick out the major feature of the change in F_{atm}^{net}, a cubic smoothing spline has been applied to it in the meridional direction to remove small scale noises.

the latter half of the 20th century due to anthropogenic warming (e.g., Levitus et al., 2001), it is at least one order of magnitude smaller than the net energy flux into the atmosphere and is neglected. Averaged over a time period and over longitude domain, $\langle \bar{F}_A \rangle$ satisfies

$$\frac{1}{a\cos\phi}\frac{d}{d\phi}(\langle \bar{F}_A \rangle \cos\phi) = \langle \bar{F}_{atm}^{net} \rangle \tag{2.5}$$

where a is the Earth's radius and ϕ is latitude. Integrating from any specific latitude ϕ_o, the energy transport in the atmosphere across any latitudinal wall ϕ, denoted by $\langle \bar{T}_A^{EB} \rangle$, can therefore be written as

$$\begin{aligned} \langle \bar{T}_A^{EB} \rangle &= 2\pi a \cos\phi \langle \bar{F}_A \rangle \\ &= 2\pi a^2 \int_{\phi_o}^{\phi} \langle \bar{F}_{atm}^{net} \rangle \cos\phi d\phi + \langle \bar{T}_A^{EB} \rangle|_{\phi_o} \end{aligned} \tag{2.6}$$

where $\langle \bar{T}_A^{EB} \rangle|_{\phi_o}$ is an integral constant and is the total atmospheric energy transport at latitude ϕ_o. The integral is commonly taken from the North Pole where $\langle \bar{T}_A^{EB} \rangle|_{\phi_o=\frac{\pi}{2}} = 0$ (e.g., Hall et al., 1994) and corrections are made to eliminate the occurrence of spurious nonzero transports of energy at both poles (Carissimo et al., 1985). In this case, the integral constant is determined with respect to the atmospheric energy transport derived from daily data in the model, for example, at the Equator, to ensure accurate estimates. Figure 2.10 shows $\langle \bar{T}_A^{EB} \rangle$ for DJF, JJA and the annual mean during the years 1961-2000 and is broadly consistent with the estimates of the meridional atmosphere heat transport in Trenberth and Caron (2001).

For the second method, the total atmospheric energy transport is computed directly from the daily data of meridional velocity, temperature and humidity by integrating the energy transport throughout the whole atmosphere column on hybrid coordinates (Delworth et al., 2006; Lin, 2004), which, denoted by $\langle \bar{T}_A \rangle$, is written as

$$\langle \bar{T}_A \rangle = 2\pi a \cos\phi \frac{1}{g} \int_0^{p_s} \langle \bar{F}_{E\phi} \rangle dp \tag{2.7}$$

where $\langle \bar{F}_{E\phi} \rangle = \langle \overline{vE} \rangle = C_p \langle \overline{vT} \rangle + \langle \overline{v\Phi} \rangle + L_e \langle \overline{vq} \rangle + \langle \overline{vK} \rangle$ which comprises the meridional transport of sensible heat, geopotential energy, latent heat and kinetic energy (K). It is also shown in Fig. 2.10 and agrees well with the estimates from the energy balance requirement. The total atmospheric energy transport is furthermore decomposed into the contributions from different dynamical processes such as the mean meridional circulation (MMC), the transient eddies and the stationary waves, i.e. $\langle \overline{vE} \rangle = \langle \overline{v} \rangle \langle \overline{E} \rangle + \langle \overline{v'E'} \rangle + \langle \overline{v}^* \overline{E}^* \rangle$, where * denotes the deviation from the zonal average i.e. $v^* = v - \langle v \rangle$. The storm tracks are the high-frequency part of the transient eddies and the low-frequency component in this study is defined as the difference between the total transient eddies and the storm tracks. The 20th century climatology for each term is shown in Fig. 2.10, in which the energy transport by transient eddies in large part dominates the atmospheric energy transport in mid-latitudes while the mean meridional circulation transports a large amount of energy to the poles in the tropics. It is also noted that the midlatitude heat transport within the high-frequency transient eddies is as large as that in stationary waves and is smaller than that in low-frequency eddies. Figure 2.11 shows the corresponding trend for each term. The total atmospheric energy transport increases almost everywhere across the globe in the late 21st century, especially in the regions of the mid-latitudes where eddies dominate the energy transport in the atmosphere. With respect to the contribution from each dynamical process, the increased atmospheric energy transport, in part, comes from the intensified storm tracks in both seasons in both hemispheres; moreover, the location of the maximum energy transport associated with the storm tracks also shifts to the poles in the warming world, which is consistent with the discussions of previous sections. It is also noticed that the intensified stationary waves and low-frequency eddies also have significant contributions to the increased midlatitude energy transport. It is also noticed that the poleward energy transport within the Hadley Cell in DJF in

the NH branch decreases in response to global warming because of the increased equatorward transport of atmospheric moisture.

Therefore, this quantitative analysis further confirms the strengthening of the storm tracks in the future climate as an important component of the large-scale general circulation in the atmosphere. The storm tracks intensify in tandem with the atmospheric energy transport in midlatitudes, serving to achieve energy balance in the atmosphere in a warmer climate. Combined with the analysis of baroclinic instability, a possible dynamical mechanism underlying the intensification and the poleward shift of the storm tracks can be summarized as the follows. As climate warms, the planetary and atmospheric energy imbalance enhances which is primarily radiative driven. This provides more available potential energy in the atmosphere causing the midlatitude storm tracks to intensify and to shift towards the poles.

In addition to the thermal structure and the energy transport in the atmosphere, the midlatitude ocean fronts are also important in the formation and development of the storm tracks. Although the oceanic heat transport in the midlatitudes is smaller relative to the atmospheric component (Trenberth and Caron, 2001), the coupling between the atmosphere and the ocean in driving the midlatitude storm tracks has been noticed in both observations and model experiments (see a review by Nakamura et al., 2004). We have found that the annual mean meridional oceanic heat transport derived from the surface energy balance (with the differential ocean heat storage rate taken into account) reduces in the future projections (Fig. 2.12; see Appendix B in this chapter). The reduction in oceanic heat transport is, in fact, consistent with the reduction in sea surface temperature contrast and salinity contrast between low and high latitudes, and the weakening of the Meridional Overturning Circulation (MOC) in the North Atlantic and North Pacific (Hazeleger, 2005; Meehl et al., 2007b). The detailed analysis of how change in oceanic heat

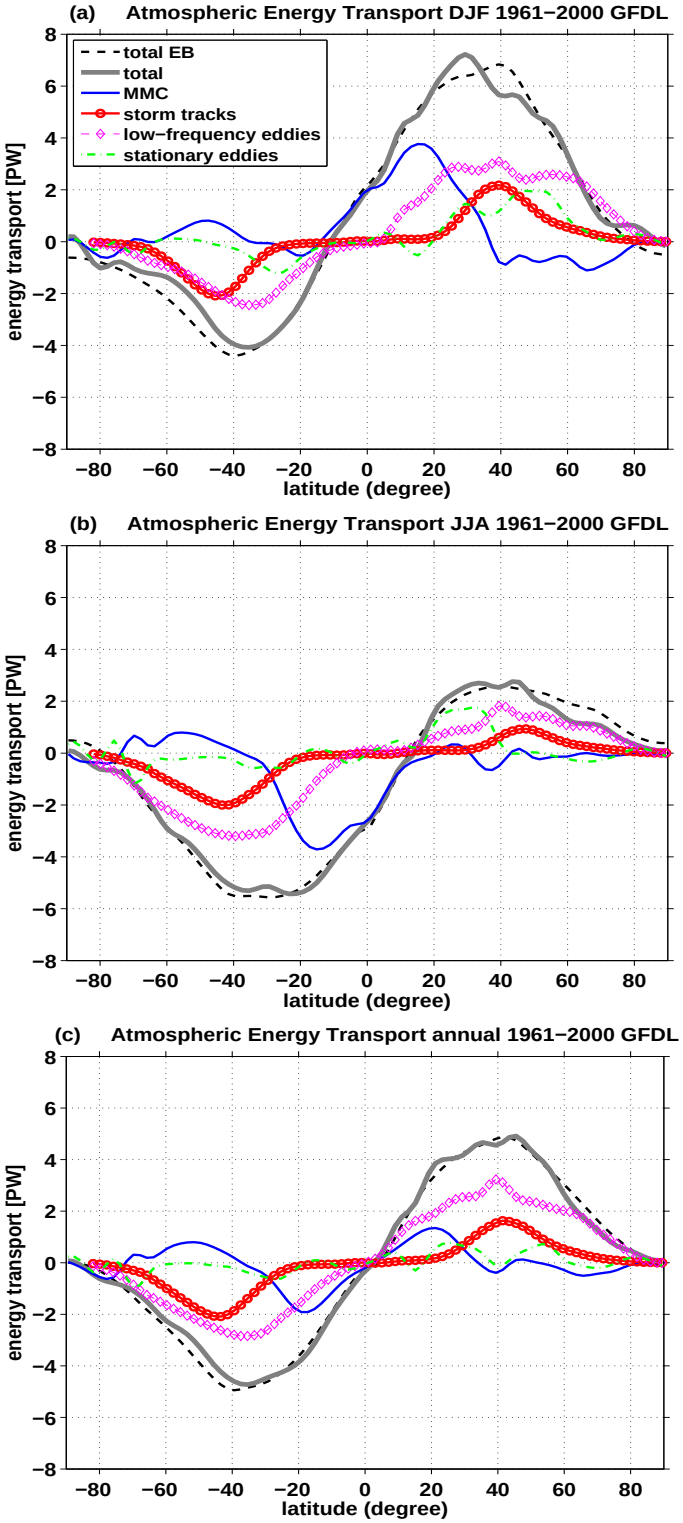

Figure 2.10: Estimates of the total atmospheric energy transport, i.e. $\langle \bar{T}_A^{EB} \rangle$ derived from the energy budget of the atmosphere and $\langle \bar{T}_A \rangle$ derived directly from daily variables (more in the text), and the energy transport in the atmosphere from the mean meridional circulations (MMC), the storm tracks (band-pass filtered transient eddies with period of 2-8 days), the low-frequency eddies (difference between total transient eddies and the storm tracks) and the stationary waves, for (a) December-February (DJF), (b) June-August (JJA) and (c) the annual mean, respectively, during years 1961-2000 from the GFDL CM2.1 model simulations. Units are PW.

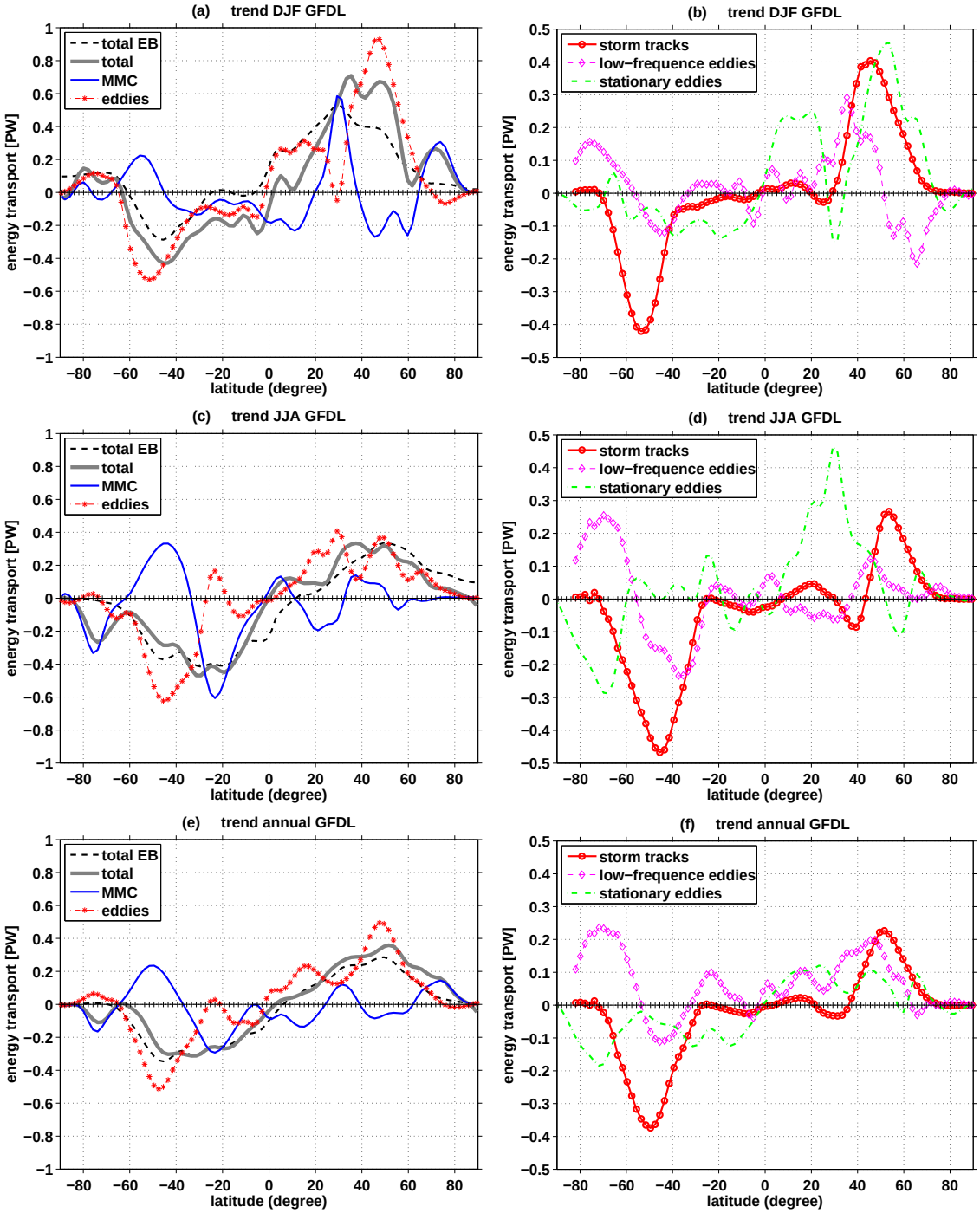

Figure 2.11: Same as Figure 2.10 but for the late 21st century trend. The trend in total eddies (transient plus stationary eddies) is also included. Units are PW.

transport impacts the storm tracks in future climate, however, is beyond the scope of this study.

2.6 Conclusions and Discussions

In this paper we have examined the future projections in the location and amplitude of the storm tracks from the GFDL CM2.1 global coupled climate model simulations, the A1B scenario. We have identified a poleward shift, poleward expansion, and intensification on the poleward flank, of storm tracks in the future climate from several major band-pass filtered transient eddy statistics. In particular, we have noticed a prominent change in meridional moisture transport associated with the storm tracks, which is important in regulating the hydrological cycle (e.g., Seager and Vecchi, 2010; Seager et al., 2010c) and atmospheric large-scale general circulation.

The future projections in transient eddy activity and its heat transport well correspond to the changes in baroclinic instability. To first order, the linear baroclinic instability growth rate is in large part determined by the meridional temperature gradients and associated available potential energy. In a warmer climate, the upper troposphere in the tropics and subtropics warms up more than that at higher latitudes, which implies increasing available potential energy, and thus the linear instability growth rate strengthens and shifts to the poles in the midlatitude upper troposphere. This is consistent with the strengthened transient eddy activity in this region. The zonal mean growth rate decreases in the midlatitude lower troposphere in northern winter because of the significant warming at the high latitude surface, however, the storm tracks intensify on their poleward flank throughout the whole troposphere. This implies that the transient eddy activity is more determined by the baroclinicity in the troposphere as a whole. It is also found that the contributions from the increasing correlation coefficient between eddy motion and eddy

energy, the increasing eddy mixing length scale and the increasing eddy velocity overwhelm that from the reduction in mean state gradients and increase transient eddy poleward energy transport in the lower troposphere in northern winter.

From the perspective of energy budget, the increased poleward energy transport associated with the midlatitude storm tracks is in good agreement with the enhanced energy imbalance in the atmosphere with increased energy gain in the tropics and subtropics and increased energy loss at high latitudes. The increased energy gain at low latitudes is mainly caused by a reduction in solar reflection (except equatorial deep convective region) due to reduced cloud cover and a reduction in outgoing longwave radiation around the Equator due to enhanced deep convection. On the contrary, in the middle and high latitudes energy is reduced through increased outgoing terrestrial radiation due to large surface warming in the NH and for the SH, through increased ocean heat uptake.

Our main objective in this chapter is to investigate the changes in storm track location and intensity in a warmer climate and how these changes are related to mean climate states and the global atmospheric energy budget. This chapter focuses on the GFDL CM2.1 global coupled climate model simulations and similar diagnoses with other CMIP3/IPCC AR4 models will be presented in Chapter 5 of this thesis. As noticed in this chapter and other previous studies (e.g., Yin, 2005; O'Gorman, 2010; Butler et al., 2010), there is a close linkage and consistency between the thermal structure in the atmosphere and the circulation response to global warming, i.e., the warming occurs extensively in the tropical and subtropical upper and middle troposphere while the tropospheric jet streams and the midlatitude storm tracks shift poleward and intensify. However, the equilibrium simulations always present the results with the radiative forcing and climate feedbacks as a whole and it is difficult to tell whether the atmospheric thermal structure is solely due to the radiative forcing or occurs as a result of the circulation change. In order

to find out the chain of causality that leads to the establishment of the equilibrium results, model experiments looking into the transient adjustment process are of great necessity. This motivates the work to be presented in Chapter 3.

2.7 Appendix A: Band-pass Filter

A band-pass filter is used in this thesis work to measure the midlatitude storm tracks as defined in Blackmon (1976) and retains the variability within 2-8 days. It is a 21-point time domain filter and does weighted moving averages using the surrounding 21 data points. Table 2.1 lists the coefficients for this band-pass filter:

Table 2.1: 2-8 day band-pass filter coefficients used in this study.

-0.00254647908947
-0.00256375080803
-0.00000000000000
0.00866936394030
0.02110671382623
0.02430854053624
-0.00000000000000
-0.06079995259343
-0.14517283397168
-0.22001164809014
0.75000000000000
-0.22001164809014
-0.14517283397168
-0.06079995259343
-0.00000000000000
0.02430854053624
0.02110671382623
0.00866936394030
-0.00000000000000
-0.00256375080803
-0.00254647908947

2.8 Appendix B: Change in Oceanic Heat Transport

The meridional oceanic heat transport can be derived from the surface energy balance and is written as

$$S_o = R_{surface} - SH - LH - \nabla \cdot F_o \tag{2.8}$$

where S_o denotes the rate of ocean heat storage, $R_{surface}$ is the net downward radiative flux at the surface, SH and LH are the surface upward sensible and latent heat fluxes, and F_o denotes the oceanic heat transport. The difference here is that the ocean heat storage (S_o) can't be neglected in the long term as climate warms. The heat storage rate is defined as the oceanic potential temperature difference between years 1961-2000 and years 2081-2100 integrated over the ocean depth, multiplying by the sea water density and heat capacity, divided by the time period of 110 years. The increase in heat storage in the oceans is rather uniform over the latitude with relatively larger values in the Southern Ocean and smaller values in the North Atlantic Ocean (not shown). It is approximately 1.5 W/m^2 on global average which is consistent with what was found in Russell et al. (2006). Figure 2.12(a) shows the climatological meridional total (atmospheric plus oceanic), atmospheric and oceanic energy transport derived based on the energy balance requirement. The atmospheric poleward energy transport generally dominates over the oceanic part except in the NH tropics. Taking the differential ocean heat storage rate into account, Fig. 2.12(b) shows the corresponding changes in heat transport in the future climate. It is noted that the oceanic heat transport decreases almost everywhere whereas the atmospheric heat transport increases. Held and Soden (2006) pointed out that the reduction in meridional ocean heat transport serves as a compensation for the increased poleward latent heat transport in the atmosphere.

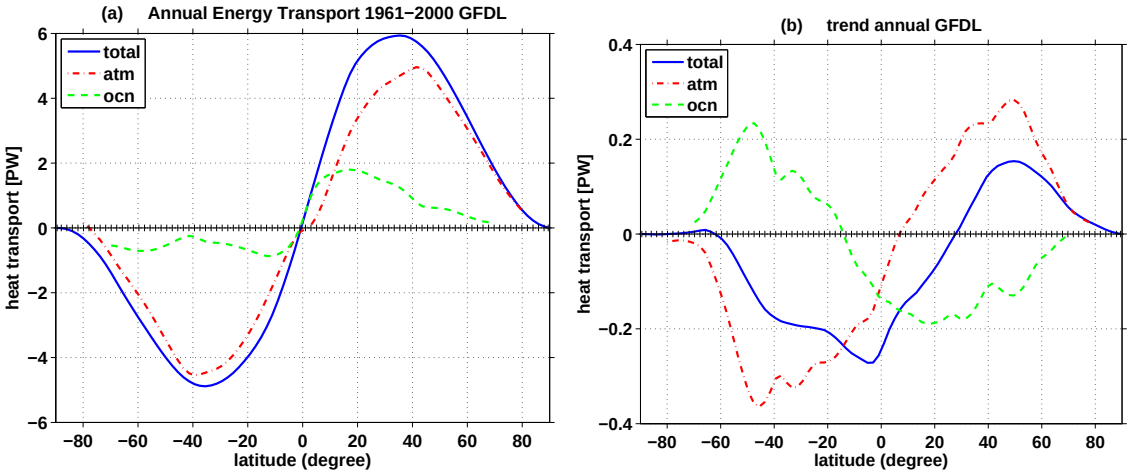

Figure 2.12: (a) Climatological and (b) 21st century trend in annual mean meridional total (atmospheric plus oceanic), atmospheric and oceanic heat transport, derived from the energy balance requirement from the GFDL CM2.1 model simulations. Units are PW.

Chapter 3

Atmospheric Circulation Response to An Instantaneous Doubling of Carbon Dioxide - Part I: Transient Thermal Response in the Troposphere

3.1 Introduction

As the climate warms due to increased greenhouse gases in the atmosphere, the atmospheric general circulation is expected to change. Climate model simulations have found a weakening of the tropical atmospheric circulation (Held and Soden, 2006; Vecchi and Soden, 2007), a poleward expansion of the Hadley Cell (Lu et al., 2007), a poleward shift of the tropospheric zonal jets (Kushner et al., 2001; Lorenz and DeWeaver, 2007) and the midlatitude storm tracks (Yin, 2005) as well as a rise in tropopause height (Kushner et al., 2001; Lorenz and DeWeaver, 2007). These cir-

culation changes have also been noticed in observational analyses for recent decades (e.g., Hu and Fu, 2007; Chen and Held, 2007). Stratospheric ozone depletion in the second half of the 20th century might dominate over the role of CO_2 increase in explaining Southern Hemisphere (SH) trends (Polvani et al., 2011; McLandress et al., 2011) and there is a possible contribution from natural variability in both hemispheres (e.g., Seager and Naik, 2011).

Some mechanisms have been proposed to understand the cause for the extratropical circulation response to global warming. Lorenz and DeWeaver (2007) suggested that the midlatitude circulation response is predominantly driven by a rise in tropopause height based on the similarities in extratropical circulation response between a simple dry general circulation model (GCM) when the tropopause height is raised and the global warming simulations of models participating in the Coupled Model Intercomparison Project 3 (CMIP3) and assessed by the Intergovernmental Panel on Climate Change Assessment Report Four (IPCC AR4). Lu et al. (2008) proposed two possible mechanisms for the zonal mean circulation response to global warming by analyzing the CMIP3/IPCC AR4 models. The first mechanism suggests that the rising tropospheric static stability stabilizes the subtropical jet streams on the poleward flank of the Hadley Cell, shifting the Hadley Cell, the baroclinic instability zone and the midlatitude eddies poleward. The second mechanism points to the importance of the increased phase speed of the midlatitude eddies. They suggested that the strengthened midlatitude wind in the upper troposphere and lower stratosphere, as a result of enhanced tropical upper tropospheric warming and/or stratospheric cooling along the sloped tropopause, accelerates the eastward phase speeds of the midlatitude eddies, shifting the subtropical breaking region and the transient eddy momentum flux convergence and surface westerlies poleward. Butler et al. (2010) prescribed a heating in the tropical troposphere in a simple atmospheric GCM and found similar poleward jet and

storm track displacements as in the CMIP3/IPCC AR4 models, suggesting that the tropical upper troposphere heating drives the circulation response to climate change. Kidston et al. (2010, 2011) found a robust increase in eddy length scale in the CMIP3/IPCC AR4 models, which is possibly caused by increased static stability in the midlatitudes. They argued that the increase in eddy length scale is a possible cause of the poleward shift of the eddy-driven jets and surface westerlies by reducing the eddy phase speed relative to the mean flow on the poleward flank of the jets and shifting the dissipation and eddy source regions poleward.

In addition, the stratosphere and its coupling with the troposphere have also been found to be important in determining the circulation response in the troposphere to global warming. Sigmond et al. (2004) studied the climate effects of middle-atmospheric and tropospheric CO_2 doubling separately using the European Centre Hamburg Model (ECHAM) middle-atmosphere climate model with prescribed sea surface temperatures (SSTs). They found strengthened Northern Hemisphere (NH) midlatitude tropospheric westerlies as a consequence of a uniform CO_2 doubling everywhere in the atmosphere and attributed this mainly to the middle-atmosphere CO_2 doubling.

The mechanisms mentioned above emphasize the close link between the thermal structure and circulation responses to global warming and suggest the warming in the middle and upper troposphere and/or the cooling in the stratosphere as possible causes. The stratospheric cooling is caused directly by increased emission due to increased CO_2 while the middle and upper tropospheric warming in the tropics arises from increased boundary layer temperature and humidity and a shift to a warmer moist adiabatic lapse rate (e.g., Hansen et al., 1984; Held, 1993). This explanation for the tropospheric warming is essentially the same as that for the enhanced tropical upper tropospheric warming during El Niños. However, in contrast to the broad warming response under global warming, the heating in the

atmosphere during El Niño events is confined in the tropics and anomalous cooling occurs in the midlatitude troposphere induced by anomalous eddy-driven ascending motion (Seager et al., 2003a). Also the Hadley Cell strengthens and narrows, and the tropospheric jets and midlatitude transient eddies shift equatorward in response to El Niños (see also Lu et al., 2008). In contrast, the warming in the middle and upper troposphere in response to global warming, as simulated by the CMIP3/IPCC AR4 models (e.g., Figure 10.7 in Chapter 10 Global Climate Projections for the IPCC AR4), expands beyond the tropical convective region to about 40^oN(S). It is not clear what causes the warming expansion into the extratropics.

In this study, we investigate the transient atmospheric adjustment to an instantaneous doubling of CO_2. The response is investigated using the National Center for Atmospheric Research (NCAR) Community Atmospheric Model (CAM) Version 3 coupled to a slab ocean model. In contrast to previous studies on the equilibrium response to global warming (e.g., Hansen et al., 1984; Manabe et al., 1990; Meehl and Washington, 1996; Shindell et al., 2001; Sigmond et al., 2004; Held and Soden, 2006; Meehl et al., 2007b; Lu et al., 2008), our work focuses on the transient evolution which allows an assessment of the sequence of cause and effect in the circulation and thermal structure response prior to establishment of a quasi-equilibrium state. Since the actual rate of anthropogenic CO_2 increase is slow compared to the instantaneous CO_2 doubling in our model experiments, the instantaneous CO_2 doubling framework may not be strictly comparable to that in the actual response to global warming in every aspect. However, we demonstrate that our simulations in both transient and equilibrium states agree well with that from the CMIP3/IPCC AR4 models in which the CO_2 concentration is gradually increased. Therefore we believe that the transient atmospheric adjustment to instantaneous CO_2 doubling provides valuable insight into the actual mechanisms underlying the extratropical tropospheric circulation response to global warming. In the paper, the following

questions will be addressed: (1) What gives rise to the broad warming in the middle and upper troposphere between 40^oS and 40^oN? (2) What are the dynamical mechanisms involved in the extratropical circulation response to increased greenhouse gases? First, we describe the model and numerical experiments in Section 3.2. The quasi-equilibrium response in thermal structure and circulation is presented in Section 3.3. Furthermore, Section 3.3 also presents the transient evolution step by step, and in particular, the diagnostics of the cause of the broad warming expansion in the extratropical middle and upper troposphere. Finally, a mechanism of the extratropical tropospheric circulation response to increased CO_2 is proposed. Section 3.4 extends the analysis of the linkage between the eddy-driven vertical motion anomaly and the warming expansion in the subtropical middle and upper troposphere to 14 CMIP3/IPCC AR4 coupled models. Discussions and conclusions are presented in Section 3.5. In Part II, we will mainly focus on the transient, sequential, response day by day before the structure of the extratropical tropospheric circulation response is established, in particular, the perturbations in both the stratosphere and the troposphere and their coupling.

3.2 Model Experiments

3.2.1 Model Description

The NCAR CAM3 is a three-dimensional atmospheric general circulation model (AGCM), which includes the Community Land Model Version 3 (CLM3), an optional slab ocean model, and a thermodynamic sea ice model. There are substantial modifications in the physics and dynamics of CAM3 from the previous version Community Climate Model (CCM3), a detailed description of which is in Collins et al. (2006). CAM3 includes options for Eulerian spectral, semi-Lagrangian, and finite-volume formulations of the dynamical equations. The implementation of CAM3

with T85 spectral dynamics is the version used in the Community Climate System Model Version 3 (CCSM3), which is a fully coupled climate model for the CMIP3/IPCC AR4. CAM3 includes revised parameterizations of cloud condensation and precipitation processes as well as for radiative processes and atmospheric aerosols. The changes to the model lead to a more realistic tropical upper troposphere temperature, a less pronounced double Intertropical Convergence Zone and an improved simulation of tropical continental precipitation. However, biases remain such as the underestimation of the tropical variability associated with the Madden-Julian oscillation, the underestimation of the implied oceanic heat transport in the SH, excessive midlatitude westerlies and surface stress in both hemispheres (Collins et al., 2006; Hurrell et al., 2006; Rasch et al., 2006).

In this study, we use the spectral version of CAM3 with resolution T42L26 (which is equivalent to $2.8^o \times 2.8^o$ (longitude by latitude) horizontal resolution and 26 vertical layers with model top at 2.917mb) coupled to a slab ocean model and a thermodynamic sea ice model (CAM3-SOM). The slab ocean model specifies the observed climatological monthly mean ocean mixed layer depths h and the monthly mean distribution of the ocean heat transport, Q_{flx} ("Q flux"), which is calculated from the surface energy fluxes obtained from a control run with prescribed ice and SSTs (McCaa et al., 2004; Collins et al., 2004). The mixed layer temperature (SST) is the prognostic variable computed from the slab ocean model:

$$\rho_o C_p h \frac{\partial SST}{\partial t} = F_{net} + Q_{flx}, \tag{3.1}$$

where ρ_o and C_p are density and specific heat capacity of ocean water, respectively, h is the ocean mixed layer depth, F_{net} is the net surface energy flux from the atmosphere to the ocean and Q_{flx} is the prescribed ocean heat transport.

3.2.2 Experimental Design

A control experiment of CAM3-SOM is run for 140 years with the CO_2 concentration fixed at 355 ppmv. The year-by-year evolution of the global annual mean surface temperature (T_s) is shown in Figure 3.1(a) (grey line) and has an average value of 288.5K. The model asymptotes towards a quasi-equilibrium state after approximately 20 years (not shown).

Using January 1st of each year of the last 100 years of the control experiment as initial conditions, we generated a 100-member ensemble of single and doubled CO_2 pair runs. The $1CO_2$ run is the same as the control experiment and keeps the CO_2 level constant at 355 ppmv and is integrated forward for 22 years. The $2CO_2$ experiment is a branch model run lasting for 22 years as well and doubles the CO_2 concentration instantaneously to 710 ppmv at the beginning of the experiment on January 1st. The difference between the $1CO_2$ run and the instantaneous $2CO_2$ run provides the atmospheric response to an instantaneous doubling of CO_2. The ensemble average across the 100 runs to a large extent removes the model's internal variability and allows for an assessment of the day-to-day adjustment of the atmospheric general circulation. Several variables such as zonal and meridional winds, temperature and specific humidity are output daily for the first two years of the model integration. This methodology has been applied successfully to the study of cause and effect in the tropospheric response to El Niño and tropical Atlantic SST anomalies (Seager and Vecchi, 2010; Seager et al., 2010a,b; Harnik et al., 2010).

3.3 Quasi-Equilibrium Atmospheric Circulation Response

Figure 3.1 shows the year-by-year evolution of the global annual mean T_s for the $1CO_2$ runs (blue lines) and the $2CO_2$ runs (red lines), for 10 of the 100 ensemble

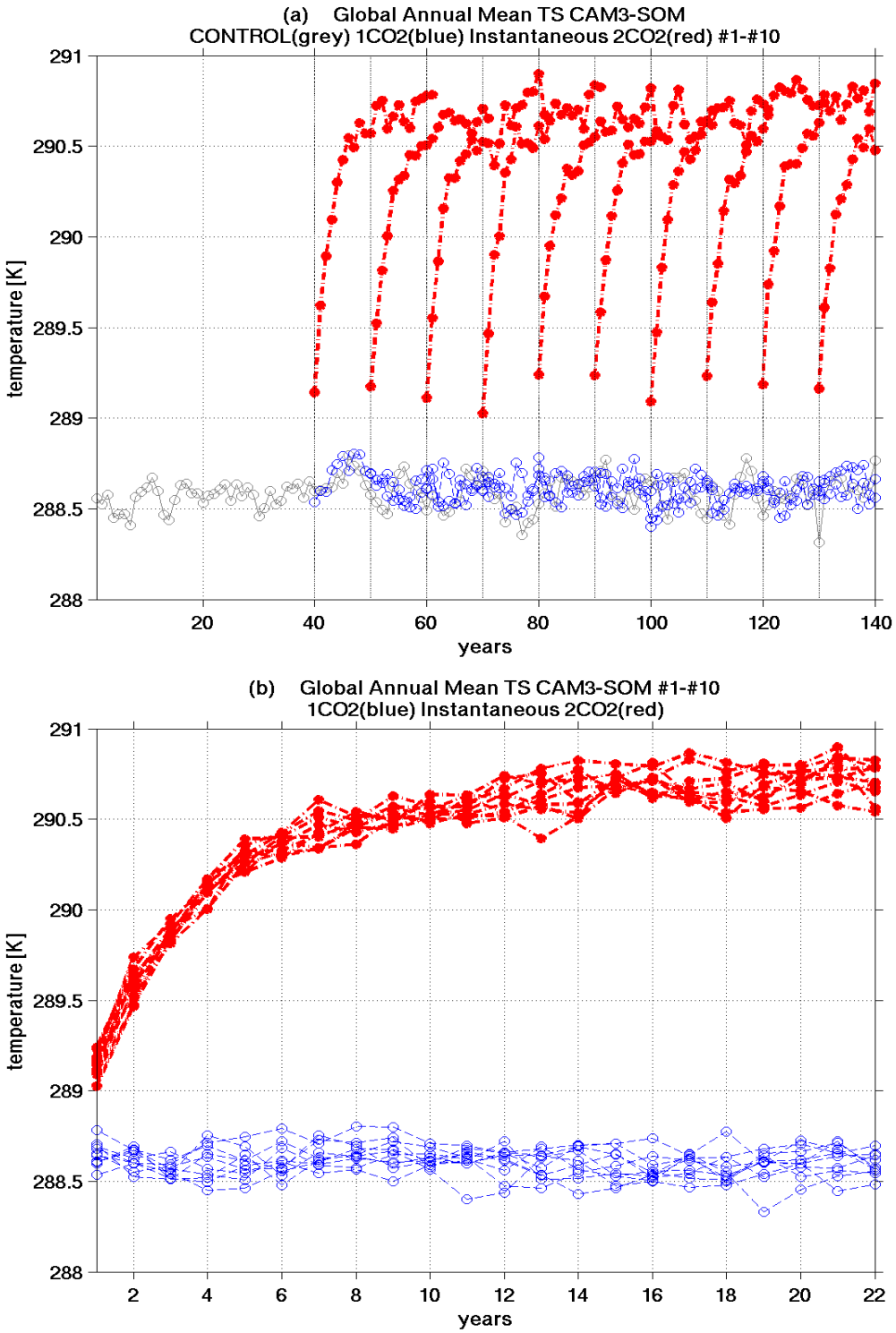

Figure 3.1: The global annual mean surface temperature T_s for the control experiment for 140 years (grey lines), 10 of the 100 $1CO_2$ climatological runs (each for 22 years) (blue lines) and instantaneous $2CO_2$ runs (each for 22 years) (red lines) (a). Same for (b) except that the time series are shifted to the same starting year (year 1) and last for 22 years.

runs. The global annual mean T_s immediately increases by about 0.5 K in the first year after the doubling of CO_2 on January 1st. After about 20 years, the $2CO_2$ runs reach a quasi-equilibrium state with T_s asymptoting towards an increase of 2.2 K (shown in Fig. 3.1(a)(b)).

The CO_2 forcing and the model's climate sensitivity are also examined in the $2CO_2$ runs. Following Gregory et al. (2004), a scatterplot of the ensemble mean change in global annual mean T_s and the change in global annual mean net radiative flux at the top of the atmosphere (TOA) for the 22 years of integration is shown in Figure 3.2. The intercept of the regression line provides an estimate for the CO_2 forcing at the time of doubling $F_{2\times} = 3.33$ W/m^2 and the slope indicates the climate response parameter $\alpha = 1.54$ W/m^2/K. In Gregory and Webb (2008), they found a doubled CO_2 forcing of 2.93 ± 0.23 W/m^2 and a climate feedback parameter of 1.1 W/m^2/K for the CCSM3 T85 slab ocean model. The two results generally agree with each other despite different horizontal resolutions.

As shown in Figure 3.1, the $2CO_2$ simulations reach equilibrium after about 20 years. Figure 3.3 shows the equilibrium response in zonal mean temperature (T), zonal wind (u), transient eddy momentum flux ($\langle\overline{u'v'}\rangle = \langle\overline{uv}\rangle - \langle\bar{u}\bar{v}\rangle$ [1]) and variance of transient meridional velocity ($\langle\overline{v'v'}\rangle = \langle\overline{vv}\rangle - \langle\bar{v}\bar{v}\rangle$) averaged over 100 ensemble members in year 22 for January-February-March (JFM) and June-July-August (JJA), where bars denote monthly averages and brackets denote zonal averages. The colors show the difference between the $2CO_2$ runs and the $1CO_2$ runs and the contours show the climatological response from the $1CO_2$ runs. The 95% significance level among the 100 ensemble runs is plotted in grey dots. We also estimated the tropopause height as the lowest pressure level at which the temperature lapse rate decreases to 2 K/km following the algorithm in Reichler et al. (2003). Figure 3.3(a) shows the tropopause level for the $1CO_2$ ($2CO_2$) runs in green (dashed ma-

[1] Without band-pass filtering.

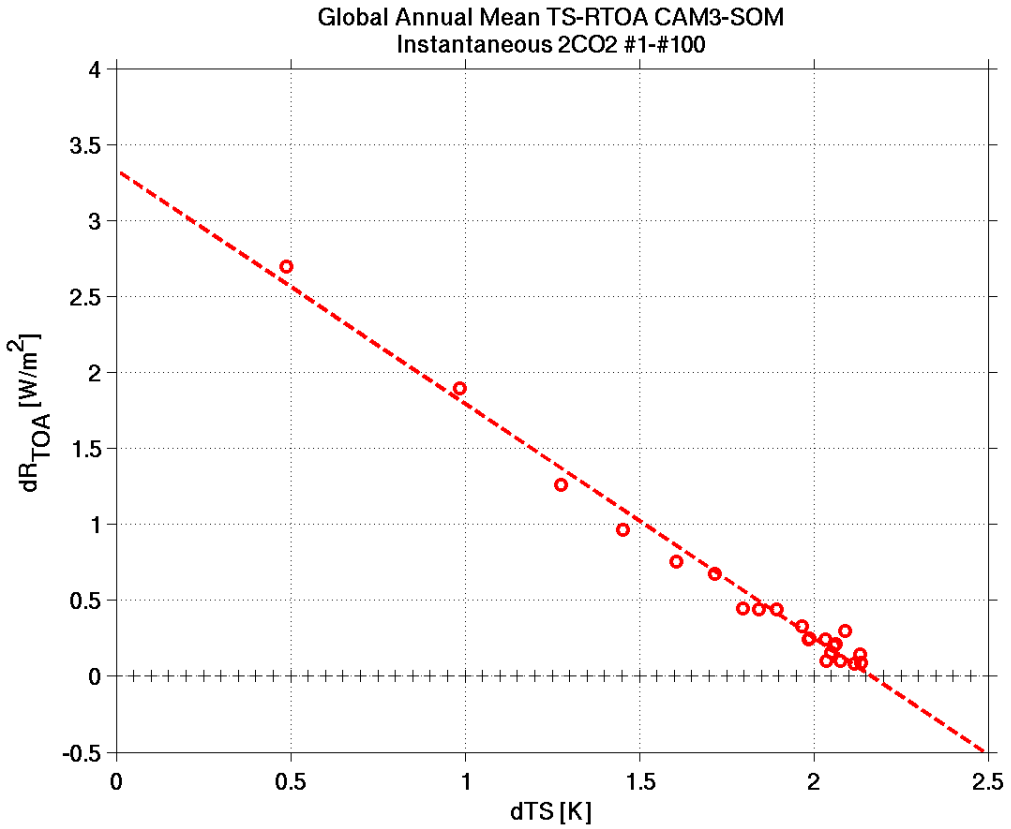

Figure 3.2: Scatter plot of the year-to-year change in global annual mean T_s and net radiative flux at the top of the atmosphere (TOA) for the 22 years of $2CO_2$ integration. It provides an estimate for the doubling CO_2 forcing $F_{2\times} = 3.33$ W/m^2 and the climate sensitivity of about 2.2 K.

genta) lines. As expected, the troposphere warms everywhere with a maximum in the tropical upper troposphere, and the stratosphere cools due to additional radiation emission to space. The tropopause height associated with the temperature increase (decrease) in the troposphere (stratosphere) rises by about 5-10mb in the tropics and 10-20mb in the extratropics, which is broadly consistent with Lu et al. (2008). The zonal mean zonal wind response shows a prominent acceleration in the upper troposphere and the stratosphere in both seasons and both hemispheres with the exception of a strong reduction in the stratospheric polar jet in JJA in the SH. The zonal wind response in the middle and lower troposphere is less obvious but in the SH there is a clear poleward shift in the tropospheric jet streams and an intensification of about 0.5 m/s on the poleward side of the climatological jets. In the NH, there is a weak poleward shift. These features in the equilibrium zonal wind response are also true for the NCAR CCSM3 coupled model simulations (not shown).

The responses in transient eddy momentum flux and variance of meridional velocity include a prominent poleward and upward shift, especially in the upper troposphere and lower stratosphere. There is also an intensification in $\langle\overline{u'v'}\rangle$ on the poleward side of the climatological maxima (NH) and minima (SH), which agrees well with that simulated in the CMIP3/IPCC AR4 coupled models (e.g., Lu et al., 2008; Wu et al., 2010). The change in $\langle\overline{v'v'}\rangle$[2] is also broadly consistent with that simulated in the CMIP3/IPCC AR4 models (e.g., Yin, 2005; Wu et al., 2010; O'Gorman, 2010) except the areas of reduction in $\langle\overline{v'v'}\rangle$ on the equatorward flank of the climatological maxima are more pronounced in our experiments.

The response in transient eddies agrees well with the temperature anomaly and the change in linear baroclinic instability in CAM3-SOM. The largest increase in meridional temperature gradient occurs in the midlatitude upper troposphere and

[2]The change in $\langle\overline{v'v'}\rangle$ is similar to the result after a band-pass filter which retains synoptic variability within 2-8 days (not shown).

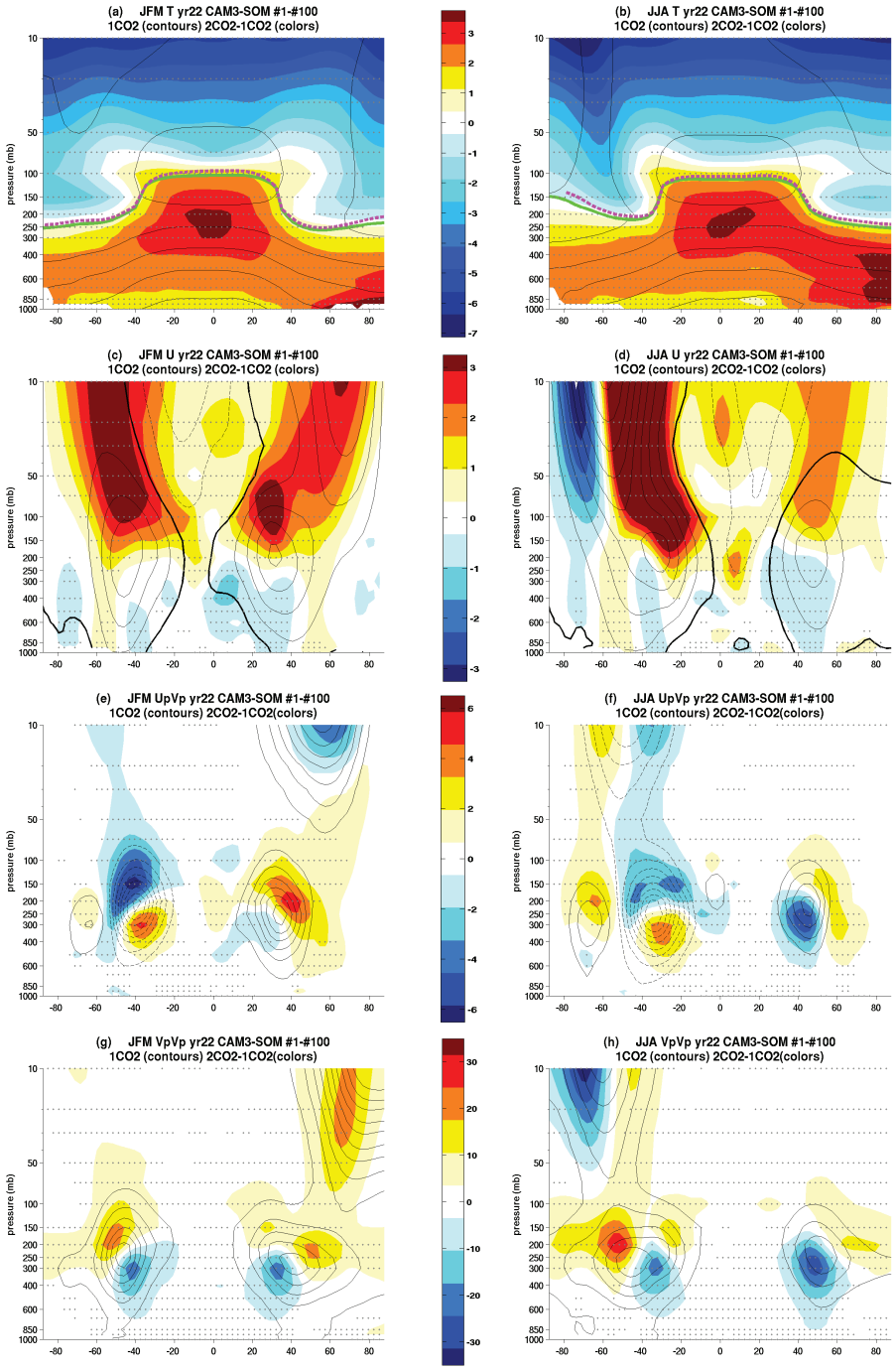

Figure 3.3: The $2CO_2$ equilibrium response in (a)(b) $\langle \bar{T} \rangle$, (c)(d) $\langle \bar{u} \rangle$, (e)(f) $\langle \overline{u'v'} \rangle$ and (g)(h) $\langle \overline{v'v'} \rangle$ for January-February-March (JFM) (left) and June-July-August (JJA) (right) as a function of latitude and pressure level. The tropopause level is plotted in green (dashed magenta) lines for the $1CO_2$ ($2CO_2$) runs. The colors show the difference between the $2CO_2$ and the $1CO_2$ runs while the contours show the climatology. The thick black lines in (c)(d) denote the climatological zero wind lines. The grey dots indicate the 95% significance level for the responses. The contour intervals are 20 K for (a)(b), 10 m/s for (c)(d), 10 m^2/s^2 for (e)(f) and 50 m^2/s^2 for (g)(h).

lower stratosphere. This is consistent with the strengthened transient eddies in this region. The close linkage between the thermal structure change and the circulation response to increased greenhouse gases has also been found in other studies (e.g., Yin, 2005; Wu et al., 2010; O'Gorman, 2010; Butler et al., 2010). Because neither daily variables nor monthly covariances in the NCAR CCSM3 coupled model are available for the CMIP3/IPCC AR4 experiments, the transient eddy activity and its future projections in the coupled model can't be assessed and compared with our results.

3.4 Transient Atmospheric Circulation Adjustment and Thermodynamics Diagnostics

3.4.1 Transient Adjustment Response

Figures 3.4, 3.5 and 3.6 show the month-by-month evolution of $\langle \bar{T} \rangle$, $\langle \bar{u} \rangle$ and $\langle \overline{u'v'} \rangle$ during the first year after the CO_2 concentration is instantaneously doubled on January 1st. The temperature structure and circulation response in the atmosphere are well established during the first year. For example, the pattern correlation between year 1 and year 22 in $\langle \bar{u} \rangle$ is above 0.6 for all months (not shown). The stratospheric cooling in December of year 1 is already similar to that of the equilibrium response (shown in Fig. 3.3(a)). The tropospheric temperature adjustment also resembles that in equilibrium with a prominent warming in the tropical middle and upper troposphere albeit with lesser magnitude. The stratosphere responds to the CO_2 doubling almost instantaneously and cools by about 2 K in January. The response in the troposphere is slower because of the delay associated with the warming of the oceans followed by transmission of the warming into the troposphere. The middle and upper troposphere in the extratropics only warms up by about 0.5 K in March.

The change in tropopause height is quite small in year 1 with the climatological $1CO_2$-run and $2CO_2$-run tropopause heights basically overlaping. The tropopause level, in general, rises by about 2mb except for about 10mb in the NH high latitudes in March of year 1. In March there is also a large westerly anomaly in the stratosphere in both hemispheres and the tropospheric zonal jets shift poleward. This then persists in the SH but weakens probably due to seasonal variation in the NH[3]. The response in transient eddy momentum flux in the troposphere gets stronger on the poleward side of the climatological jets starting from March of year 1. Similar to the change in tropospheric jets, the strengthening of the transient eddies occurs persistently throughout the year in the SH but has a notable seasonal variation in the NH.

Figure 3.7(a)(b) show the day-by-day evolution of the zonal mean temperature and zonal wind averaged over 30^oN to 70^oN from January 1st to April 30th of year 1 as a function of time and pressure level. The average over 30^oS to 70^oS is shown in Figure 3.7(c)(d). The response is robust for different choices of latitudinal bands. A 5-day running average has been applied to all the variables. It is noted that the cooling in the stratosphere occurs first in the upper stratosphere and extends to the lower stratosphere in about a month. The substantial warming (0.5 K) in the middle and upper troposphere takes place in early March. The eastward zonal wind anomaly clearly begins in the upper stratosphere and then gradually moves downward into the lower stratosphere and the troposphere with the whole process taking about 100 days. The succession of events, first happening in the stratosphere and subsequently in the troposphere, resembles that in observations of subseasonal to seasonal variability (Baldwin and Dunkerton, 2001) as well as in the "downward control" theory (Haynes et al., 1991).

[3]In this model experiment the NH tropospheric jet shift in summer is very weak (in both the transient and equilibrium states) while that in winter is slightly stronger (shown in Fig. 3(c)(d)). However, there is not much seasonal dependence for the tropospheric jet displacement in the SH.

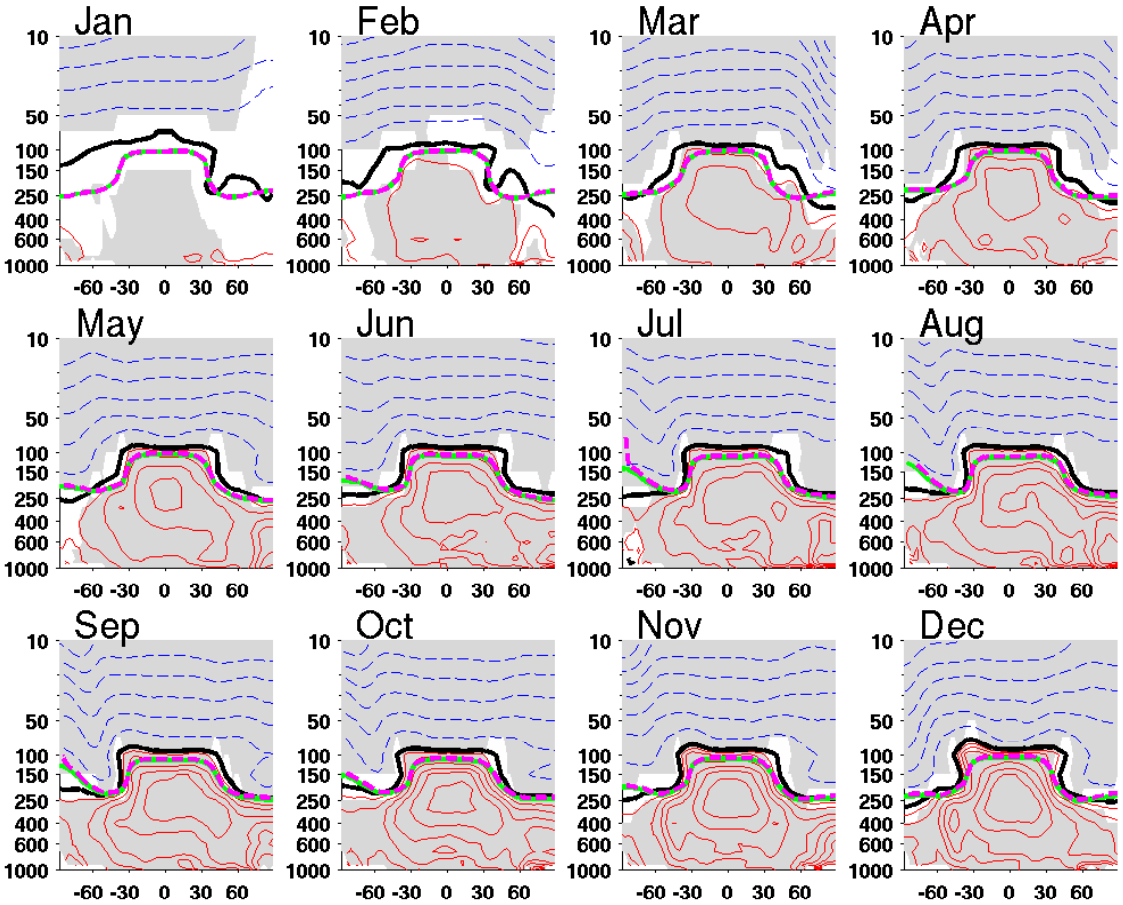

Figure 3.4: The month-by-month transient response in $\langle \bar{T} \rangle$ in year 1 shown as a function of latitude and pressure level. The color contours show the difference between the $2CO_2$ and the $1CO_2$ runs with red (dashed blue) denoting positive (negative) anomalies. The think black lines show zero values. The tropopause height is plotted in thick green (dashed magenta) lines for the $1CO_2$ ($2CO_2$) runs. The grey shadings show the 95% significance level. The contour intervals are 0.25 K for positive values and -1 K for negative values.

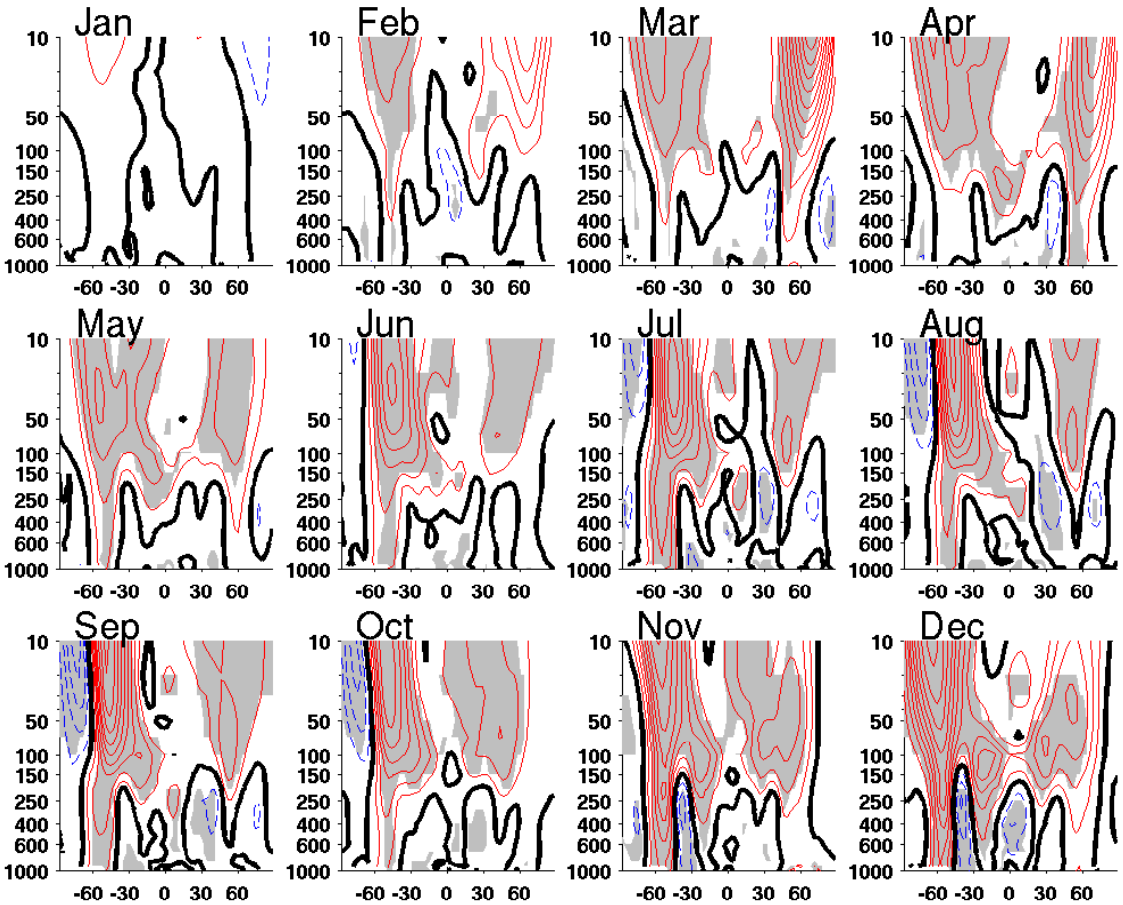

Figure 3.5: Same as Figure 3.4 for but for $\langle \bar{u} \rangle$. The contour interval is 0.5 m/s.

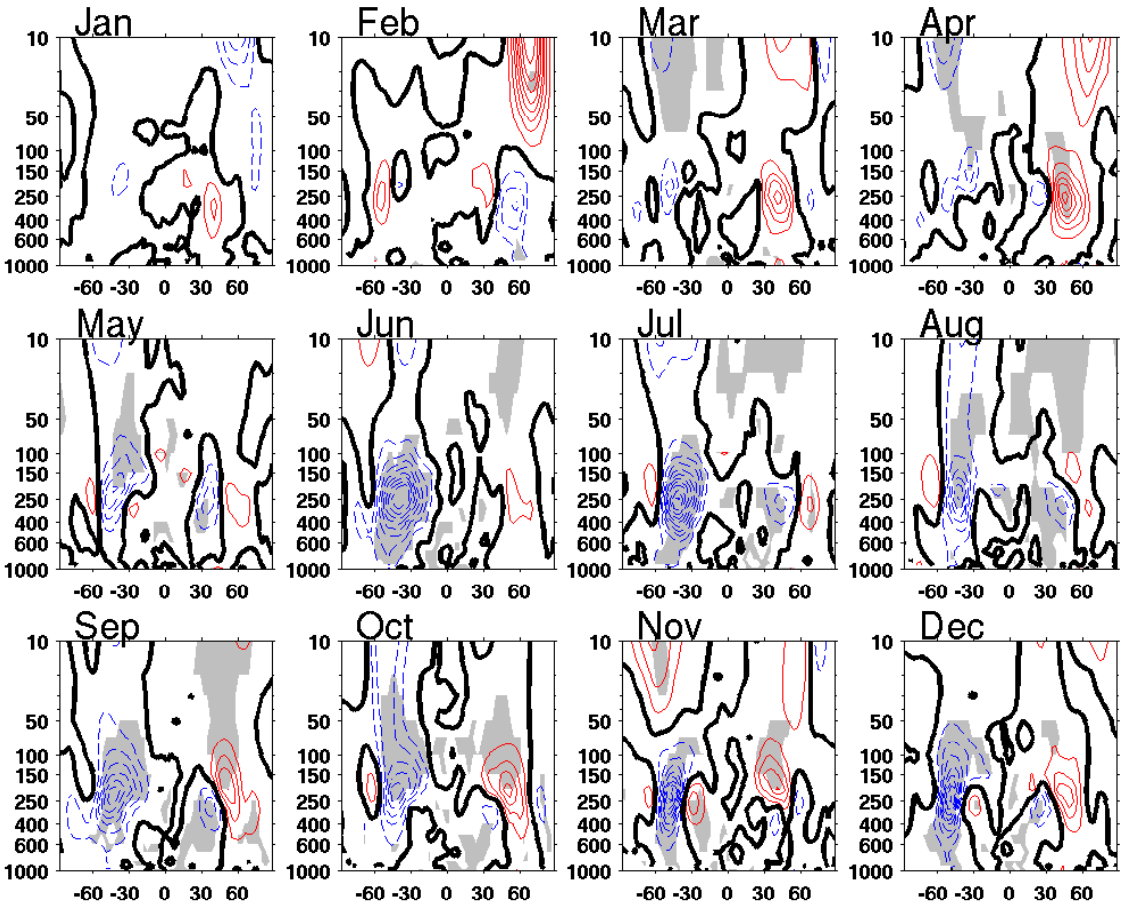

Figure 3.6: Same as Figure 3.4 for but for $\langle \overline{u'v'} \rangle$. The contour interval is 1 m^2/s^2.

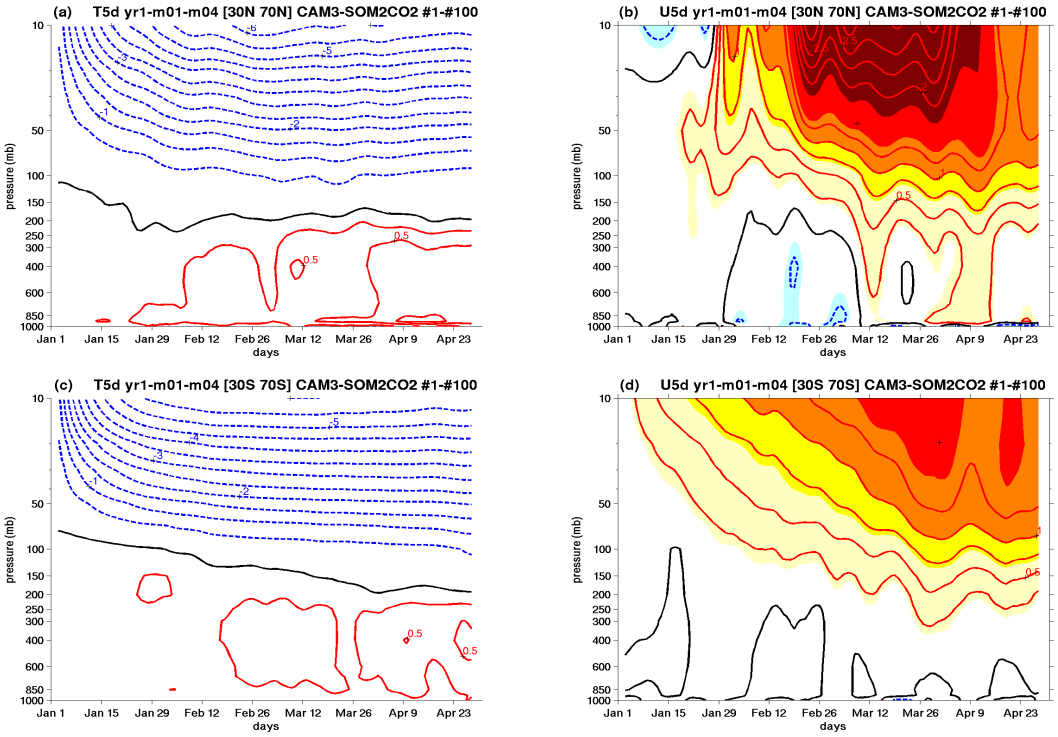

Figure 3.7: The $2CO_2$ transient day-by-day response in $\langle T \rangle$ (left) and $\langle u \rangle$ (right) shown as a function of day (from January 1st to April 30th) and pressure level. (a)(b) are averaged between 30^oN and 70^oN while (c)(d) are averaged between 30^oS and 70^oS. A 5-day running average has been applied for plotting. The contour intervals are 0.25 K (-0.5 K) for positive (negative) values in (a)(c) and 0.25 m/s for (b)(d).

Figure 3.8 shows the day-by-day response in $\langle \bar{T} \rangle$, $\langle \bar{u} \rangle$, total and 2-8 day band-pass filtered[4] eddy momentum flux convergence as a function of time and latitude in January-February-March-April (JFMA) of year 1. These variables are all averaged over the middle and upper troposphere from 150mb to 500mb, and a two-dimensional spatial (latitude-pressure level) 1-2-1 smoothing and a 10-day temporal running average are applied in plotting. Grey shadings in Fig. 3.8 denote the 90% significance level among the 100 ensemble runs. The total eddy momentum flux convergence is defined as $-\frac{1}{acos^2\phi}\frac{\partial}{\partial\phi}(\langle uv \rangle - \langle u \rangle \langle v \rangle) cos^2\phi$ while its band-pass filtered transient component is denoted by $-\frac{1}{acos^2\phi}\frac{\partial}{\partial\phi}\langle u_H v_H \rangle cos^2\phi$. As shown in Fig. 3.8(a), the warming of the middle and upper troposphere first occurs in the tropics and then extends to the subtropics around and beyond 40^oS in mid-February and 40^oN in early March. Almost simultaneously the jet in the middle and upper troposphere is displaced poleward with a reduction in zonal wind equatorward of 40^oN and an intensification poleward of 40^oN and 40^oS (shown in Fig. 3.8(b)). The change in eddy momentum flux convergence, and in particular, its band-pass filtered component, shows a similar transition with a dipole pattern starting from mid-February in the SH and early March for the NH (shown in Figs. 3.8(c)(d)). In fact, this (significant) enhanced transient eddy momentum flux convergence in the extratropics occurs ahead of the (significant) tropospheric jet shift and acts to accelerate the westerlies in the subtropical middle and upper troposphere.

3.4.2 Thermodynamics Diagnostics

As mentioned in the Introduction, there is a close link and consistency between the tropospheric thermal structure and the circulation response in both the El Niños and the global warming scenario. During the El Niños, there is a confined tropical

[4]The time filter used here is a standard 21-point two-sided band-pass filter that keeps the variability within 2-8 days. It skips the first and last 10 days in the time series of daily eddy momentum flux convergence.

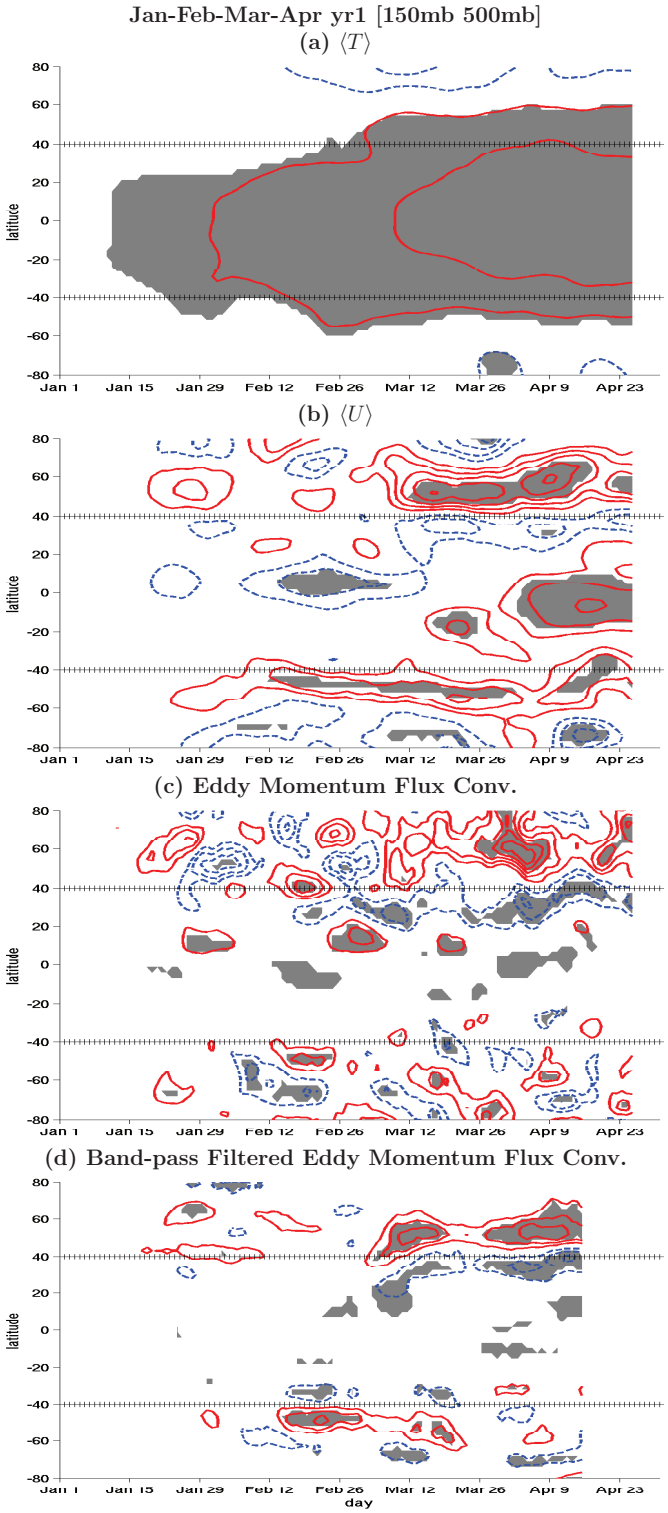

Figure 3.8: The $2CO_2$ transient day-by-day response in (a) $\langle T \rangle$, (b) $\langle u \rangle$, (c) total and (d) band-pass filtered eddy momentum flux convergence (defined in text) as a function of day (from January 1st to April 30th) and latitude. These variables are averaged from 150mb to 500mb, and a two-dimensional (latitude-pressure level) 1-2-1 smoothing and a 10-day temporal running average are applied. Grey shadings denote 90% significance level. The contour intervals are (a) 0.25 K, (b) 0.25 m/s and (c)(d) 0.1 m/s/day.

tropospheric warming and a cooling in the midlatitudes which is associated with an equatorward displacement of the tropospheric jets and midlatitude transient eddies. On the contrary, as a result of CO_2 increase, the tropospheric warming extends broadly into the subtropics and the midlatitudes along with a poleward shift of the zonal wind and the storm tracks. Previous studies have demonstrated that the midlatitude cooling in response to the El Niños is driven by eddy-induced ascent anomaly (Seager and Vecchi, 2010; Seager et al., 2010a,b; Harnik et al., 2010), then what is responsible for the extensive tropospheric warming to CO_2 increase?

This section will diagnose the cause of the subtropical warming tendency (diabatic vs. adiabatic) in the $2CO_2$ experiments. Here we focus on March of year 1 when the middle and upper troposphere starts to warm up in the NH subtropics by about 0.5 K (shown in Fig. 3.4). Following Seager et al. (2003a), the zonal mean temperature budget is written as

$$\begin{aligned}\frac{\partial \langle \bar{T} \rangle}{\partial t} &= \underbrace{-\left\{ \frac{\langle \bar{v} \rangle}{a} \frac{\partial \langle \bar{T} \rangle}{\partial \phi} + \langle \bar{\omega} \rangle \left(\frac{\partial \langle \bar{T} \rangle}{\partial p} - \frac{R}{C_p} \frac{\langle \bar{T} \rangle}{p} \right) \right\}}_{\text{(a) MMC}} \\ &\quad \underbrace{-\frac{1}{a cos\phi} \frac{\partial}{\partial \phi} \big(\langle \overline{vT} \rangle - \langle \bar{v} \rangle \langle \bar{T} \rangle \big) cos\phi - \frac{\partial}{\partial p} \Big(\langle \overline{\omega T} \rangle - \langle \bar{\omega} \rangle \langle \bar{T} \rangle \Big) + \frac{R}{C_p} \frac{1}{p} \Big(\langle \overline{\omega T} \rangle - \langle \bar{\omega} \rangle \langle \bar{T} \rangle \Big)}_{\text{(b) Eddies}} \\ &\quad \underbrace{+ \frac{\langle \bar{Q} \rangle}{C_p}}_{\text{(c) Diabatic Heating}},\end{aligned} \tag{3.2}$$

where bars denote monthly averages and brackets denote zonal averages. In Equation 3.2, the temperature tendency is divided into contributions from (a) the mean meridional circulation (MMC), (b) the transient and stationary eddies and (c) the total diabatic heating Q. The diabatic heating term is the sum of the temperature tendency due to horizontal diffusion and vertical diffusion, solar heating rate, long-

wave heating rate, and the heating resulting from shallow, deep-convective, and large-scale condensation processes. Other terms such as the temperature tendency due to orographic gravity wave drag and kinetic energy (KE) dissipation are not saved and are neglected in our analysis. However, due to the reformulation of the parameterized heating since CAM2 in order to conserve energy in the model, the KE dissipation term in the surface layer is large ($\approx$ 0.9 K/day) and maximizes in the midlatitude oceanic storm track region where the surface stress is large (Boville and Bretherton, 2003). This KE dissipation term results in some discrepancies in the balance in the zonal mean temperature equation in the surface layer (not shown).

Figure 3.9 shows the latitude-pressure level plot of the net temperature tendency ($\frac{\partial\langle\bar{T}\rangle}{\partial t}$) (Fig. 3.9(a)), the temperature tendency computed from the RHS of Equation 3.2 (Fig. 3.9(b)), the temperature tendencies due to the MMC (Fig. 3.9(c)), the eddies (Fig. 3.9(d)) and the total diabatic heating (Fig. 3.9(f)), separately, during March of year 1. In addition, Figure 3.9(e) shows the total dynamical contribution, computed as the sum of the MMC and the eddies (Fig. 3.9(c) and 3.9(d)). The colors show the difference between the $2CO_2$ runs and the $1CO_2$ runs and the contours show the results from the $1CO_2$ runs. The net temperature tendency (in unit of [K/month]) is estimated as the temperature difference from March 1st to March 31st, which shows a warming tendency in the subtropical middle and upper troposphere from 200mb to 500mb and from 20^oN to 45^oN (indicated by the black box in Fig. 3.9) as well as a warming tendency poleward of 50^oN. Figure 3.9(b), in colors, shows the matching temperature tendency computed from the RHS of Equation 3.2, which, away from the surface, is in good agreement with the actual tendency shown in Fig. 3.9(a). A comparison between Figs. 3.9(e) and 3.9(f) shows that the thermodynamical and dynamical contributions are always opposing each other and it is the dynamical part that leads to the warming tendency in the

subtropical middle and upper troposphere. More specifically, the adiabatic warming in the subtropical middle and upper troposphere comes from the change in MMC which is mostly attributed to the anomalous downward vertical motion (Fig. 3.9(c)) and is opposed by the change in transient eddy heat transport (Fig. 3.9(d)) and, at lower levels, diabatic heating (Fig. 3.9(f)). The anomalous downward vertical motion in the subtropical region, in fact, tends to reduce the low-level cloud cover and the condensational heating rate (not shown) and, hence, the total diabatic heating in the region. The polar warming at northern high latitudes is caused by the increased diabatic heating, in particular, the increased longwave radiative heating as a result of increased greenhouse gases (Fig. 3.9(f)). The temperature tendency diagnosis demonstrates that the warming expansion beyond the tropical convective region is *mainly dynamically driven* and thermodynamically opposed with the circulation change preceding the tropospheric temperature change.

In order to identify the cause for the anomalous vertical motion in the subtropics, we have computed the eddy-driven vertical motion ω_{eddy}. It is derived using the continuity equation and the balance between the Coriolis torque and the momentum flux convergence, which is the dominant balance in the extratropics in the zonal momentum equation, following Seager et al. (2003a):

$$\langle\bar{\omega}_{eddy}(p)\rangle = \langle\bar{\omega}(p_o)\rangle - \frac{1}{acos\phi}\frac{\partial}{\partial\phi} \times \int_{p_o}^{p} \frac{1}{acos\phi}\frac{1}{f + a^{-1}\langle\bar{u}\rangle tan\phi}\frac{\partial}{\partial\phi}\Big(\langle\overline{u'v'}\rangle cos^2\phi\Big)\, dp, \tag{3.3}$$

where p_o is taken to be 100mb[5] (Equation 3.3 is not applicable in the deep tropics where the Coriolis parameter approaches zero.). This is, in fact, the downward motion controlled by the wave forcing above in the "downward control" principle in Haynes et al. (1991) except in the conventional Eulerian framework. The eddy-induced motion ω_{eddy} was computed at all pressure levels using $\langle\bar{u}\rangle$ and $\langle\overline{u'v'}\rangle$ from the model output. Figure 3.10 shows ω_{eddy} computed from Equation 3.3 and the

[5]There is a $\cos\phi$ term missing in the denominator of Equation (7) in Seager et al. (2003a).

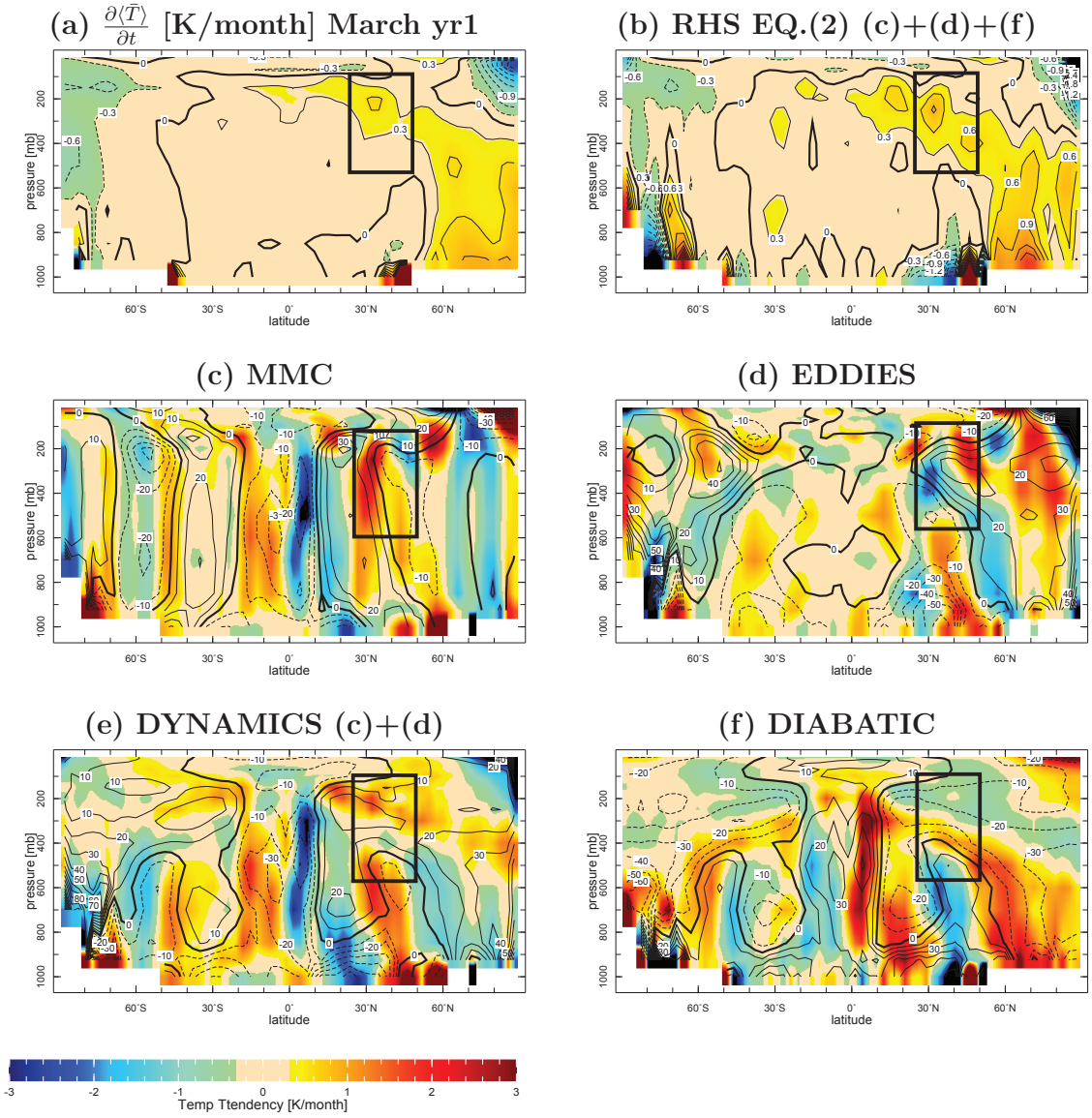

Figure 3.9: (a) The actual zonal mean temperature tendency ($\frac{\partial\langle\bar{T}\rangle}{\partial t}$), (b) the temperature tendency in sum of (c)(d)(f), temperature tendencies due to (c) mean meridional circulation (MMC), (d) total eddies (stationary and transient eddies) and (f) total diabatic heating, (e) dynamical heating in sum of (c) and (d). The plots are all for March of year 1 and of unit K/month. Both the contours and colors in (a) and (b) show the $2CO_2$ response with contour interval of 0.3 K/month. The colors in (c)(d)(e)(f) show the $2CO_2$ response while the contours show the climatology.

actual vertical motion ω from the model output in March of year 1 (Note, the values of ω_{eddy} are large in the surface layer because of neglect of surface friction.). In both hemispheres there is reasonable agreement in the meridional structure of the actual vertical velocity and the eddy-induced vertical velocity away from the tropics in both the climatological $1CO_2$ runs (shown in contours) and the $2CO_2$-run anomalies (shown in colors). The anomaly in ω_{eddy} is primarily attributed to the change in $\langle\overline{u'v'}\rangle$. As shown in Fig. 3.10(b), there is an anomalous ascending motion in the NH tropics driven by enhanced tropical convective heating following the CO_2 increase which is consistent with the increased diabatic heating in the region (Fig. 3.9(f)). In the NH subtropics (between 30^oN and 45^oN), there is a descending motion anomaly which also shows up in the change in ω_{eddy}. This indicates that the anomalous downward motion is primarily driven by the enhanced transient eddy momentum flux convergence. The Hadley Cell expansion as found in CMIP3/IPCC AR4 coupled models (Lu et al., 2007) is also presumably related to the changing transient eddies in this region.

As shown in Fig. 3.8(a), the subtropical warming expansion in the SH takes place in mid-February of year 1 albeit of small magnitude. A similar thermodynamic analysis has been done for February and it is found that the SH subtropical warming at that time is also driven by enhanced transient eddy momentum flux convergence and resulting anomalous downward vertical motion (not shown).

The heating anomaly in the subtropical middle and upper troposphere in this model experiment is induced by the dynamical circulation change rather than vice versa. It is the enhanced transient eddy momentum flux convergence in response to increased CO_2 that causes anomalous descending motion and adiabatic heating in the subtropical middle and upper troposphere. The dynamics of the changing transient eddies is closely connected with the response in the stratosphere and coupling between the stratosphere and the troposphere, and this will be further

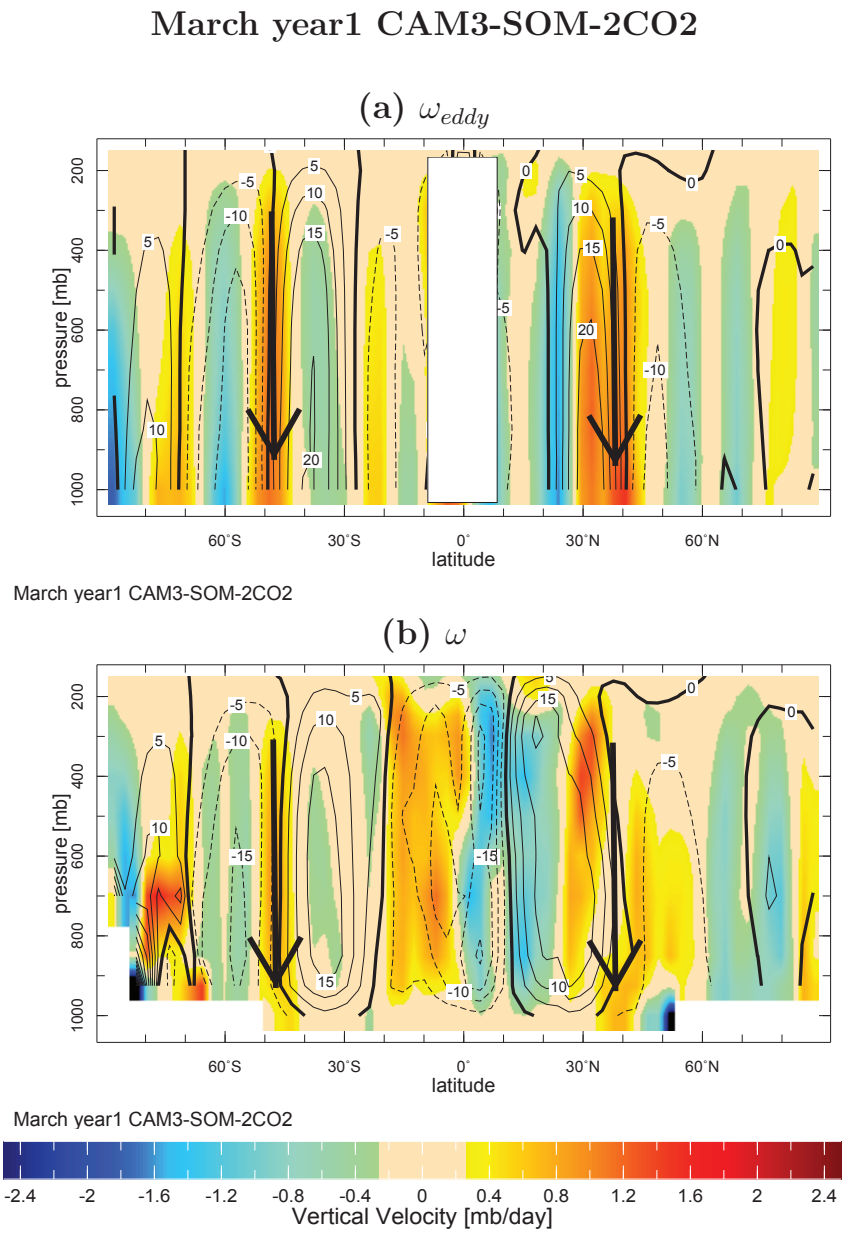

Figure 3.10: (a) The transient eddy-driven vertical motion ω_{eddy} [mb/day] and (b) the actual vertical motion ω [mb/day] from model output in March of year 1. Equation 3.3 for eddy-driven vertical motion is not applicable in the deep tropics and thus regions between 10S and 10N are masked out in (a). The colors show the $2CO_2$ response while the contours show the climatological results with contour interval of 5 mb/day. The positive (negative) values in ω_{eddy} (ω) denote downward (upward) motion.

investigated in Part II.

3.4.3 Possible Dynamical Mechanisms

Based on the above diagnostic work, we propose a possible dynamical mechanism for the extratropical circulation response to increased CO_2 with the following sequence:

(1) The CO_2 doubling gives rise to a westerly zonal wind anomaly in the stratosphere. The westerly acceleration propagates downward into the lower stratosphere and upper troposphere.

(2) The westerly acceleration in the lower stratosphere and upper troposphere changes the propagation of baroclinic eddies, leading to enhanced transient eddy momentum flux convergence between 40^oN(S) and 60^oN(S).

(3) The increased transient eddy momentum flux convergence drives an anomalous mean meridional circulation in the troposphere as well as a poleward displacement of the tropospheric jets.

(4) The induced anomalous descending motion in the subtropical middle and upper troposphere leads to an adiabatic heating anomaly and thus a broad warming expansion beyond the tropical convective region. The subtropical warming allows adjustment to thermal wind balance with the poleward shifted jets.

A schematic figure showing the hypothesized sequence of the dynamical response is shown in Figure 3.11. Other mechanisms are also possible. For example it is expected that the increase in tropopause height could cause an increase in the length scale of transient eddies which has been associated with a poleward jet shift (Williams, 2006). The dynamical mechanisms of the transient adjustment and their cause and effect, explaining all possibilities, will be analyzed in detail in Part II. Here we provide a brief summary of Part II. Part II will emphasize the transient sequential response in both the stratosphere and the troposphere before the circulation change is well established in the extratropical troposphere. Three phases

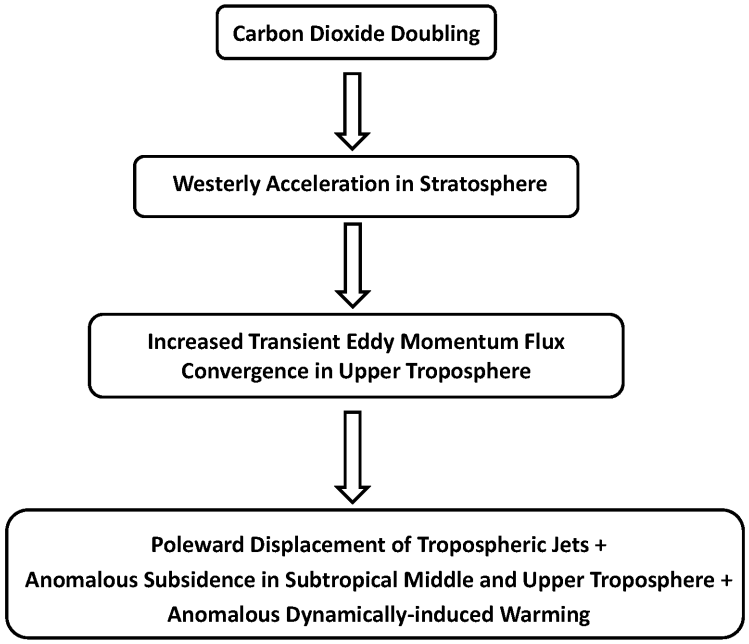

Figure 3.11: Summary of the proposed mechanisms causing the tropospheric extratropical circulation response to increased CO_2 concentration.

are defined during the period of transient adjustment. A fast radiatively-induced thermal response occurs during January (Phase One) and an easterly anomaly is generated in the NH subpolar stratosphere. Phase Two, which covers February, features a westerly acceleration in the stratosphere and this is driven dynamically by the intensified momentum flux convergence of planetary stationary eddies. A 'downward propagation' of the westerly acceleration from the lower stratosphere to the troposphere is seen in March and April (Phase Three) and this is followed by a poleward displacement of the tropospheric midlatitude jets. In this final phase, the transient eddies play an important role in shifting the position of the tropospheric zonal wind.

3.5 Conclusions and Discussions

We have explored the transient evolution of the atmospheric adjustment to an instantaneous doubling of CO_2 concentration. The sequence in the general circulation response in the atmosphere helps reveal the dynamical mechanisms underlying the equilibrium circulation response, for example, the poleward expansion of the Hadley Cell (Lu et al., 2007), and the poleward shift of the tropospheric jets and storm tracks (e.g., Kushner et al., 2001; Yin, 2005) as found in CMIP3/IPCC AR4 models. In contrast to previous studies suggesting that the thermal forcing in the tropical upper troposphere drives the tropospheric circulation response (e.g., Butler et al., 2010), our results indicate that the broad warming expansion in the subtropical middle and upper troposphere is a consequence of the circulation change. Enhanced transient eddy momentum flux convergence in the lower stratosphere and upper troposphere, possibly originating from the stratospheric westerly acceleration, drives an anomalous mean meridional circulation in the troposphere. The induced anomalous descending motion in the subtropical middle and upper troposphere warms the air adiabatically. Afterwards the subtropical warming and the poleward displacement of the jets and the baroclinic eddies can potentially feed back positively onto each other via a poleward shift in eddy generation region, leading to a further poleward shift of the jets and the eddies and a further warming expansion in the subtropical troposphere.

It is noted here that this study focuses primarily on the atmospheric transient adjustment process before there is any appreciable SST change. Certainly SST change in a longer time scale may cause further circulation change. Nonetheless, the transient adjustment shown here is similar to the results in CMIP3/IPCC AR4 fully coupled models. As also demonstrated in Lu et al. (2009), the observed widening of the tropics in the latter half of the twentieth century is entirely attributed to the direct effect in the atmosphere of changing trace gas concentrations rather than to

SST warming.

Our results also show the sequence of the zonal wind anomaly in the vertical column of the atmosphere, indicating that the poleward displacement of the tropospheric jets follows the subpolar westerly anomaly in the stratosphere. It suggests the importance of the stratosphere, and the coupling between the stratosphere and the troposphere, in regulating the extratropical tropospheric circulation response to increasing CO_2. A detailed analysis of the stratospheric response and the stratosphere-troposphere coupling, including how the response 'propagates' downward into the troposphere and how the eddies respond step-by-step will be further examined in Part II. It is noted here that our study intends to understand the circulation response and the dynamical mechanisms in CMIP3/IPCC AR4-like models albeit most of the models have poorly resolved stratospheres. Some studies have argued that a well resolved stratosphere is required to reproduce observed behavior (e.g., Shindell et al., 1999; Sassi et al., 2010). On the other hand, Sigmond et al. (2008) suggested that the atmospheric circulation response to CO_2 doubling does not necessarily require a well-resolved stratosphere but rather a realistic simulation of the zonal wind strength in the middle and high latitude lower stratosphere. The zonal mean zonal wind in CAM3 agrees with reanalysis data in this region. The circulation response to a CO_2 doubling in both the troposphere and the stratosphere in our results also agrees to a large extent with those from previous studies, which used models with much finer vertical resolution in the middle atmosphere (e.g., Shindell et al., 2001; Sigmond et al., 2004). However, a model lid in the mid-stratosphere is known to impact the vertical propagation of stationary planetary scale waves during northern hemisphere winter (Shaw and Perlwitz, 2010; Sassi et al., 2010). Assessing the transient and equilibrium responses to CO_2 doubling in a model with high vertical resolution and a high model lid height is the subject of future investigation. Finally, as our experiments double the CO_2 concentration on

January 1st, it would be interesting to change the time of CO_2 doubling and see if the model responds differently. A set of experiments with an instantaneous CO_2 doubling on July 1st is currently under investigation.

Chapter 4

Atmospheric Circulation Response to An Instantaneous Doubling of Carbon Dioxide - Part II: Dynamics and Stratosphere-Troposphere Coupling

4.1 Introduction

The anthropogenic climate change simulations from the comprehensive climate models for the Coupled Model Intercomparison Project phase 3 (CMIP3) / Intergovernmental Panel on Climate Change the Fourth Assessment Report (IPCC AR4) have projected changes in the general circulation of the atmosphere as a consequence of increased CO_2. Yin (2005) found a consistent poleward and upward

shift of the midlatitude storm tracks along with the poleward shifts of the surface wind stress and the precipitation zone. The changes in the location and intensity of the storm tracks are also closely related to the poleward displacement of the tropospheric zonal jets (Kushner et al., 2001) and the poleward expansion of the Hadley Cell (Lu et al., 2007); however, what leads to these circulation changes is not entirely clear.

The atmospheric circulation response to increased greenhouse gases was investigated using the National Center for Atmospheric Research (NCAR) Community Atmospheric Model Version 3 (CAM3) coupled to a slab ocean model (SOM) when the carbon dioxide (CO_2) in the atmosphere was instantaneously and uniformly doubled. While the CMIP3/IPCC AR4 climate models more realistically gradually increase the CO_2 concentration, these simulations are always in quasi-equilibrium and don't provide evidence on how and why the general circulation of the atmosphere adjusts to the external CO_2 forcing. The methodology used in this study, however, allows a step-by-step assessment of the cause and effect that occurs in the circulation adjustment to increased greenhouse warming.

The model description and experiment design were presented in Chapter 3. It was demonstrated that the simulations approximately reach quasi-equilibrium after about 20 years of model integration after the sudden CO_2 doubling and the quasi-equilibrium responses resemble that from the CMIP3/IPCC AR4 coupled climate models under the A1B global warming scenario. In fact, most of the features, such as the enhanced tropical and subtropical upper tropospheric warming and the poleward shift of the tropospheric jets and the midlatitude storm tracks, are well established after a few months of model integration. It has been widely recognized that the enhanced upper tropospheric warming is closely related to the circulation responses such as the poleward displacement of the tropospheric jet streams and the midlatitude transient eddies (e.g., Wu et al., 2010; O'Gorman, 2010; Butler

et al., 2010; Rivire, 2011), and some studies, for example, Butler et al. (2010) and Rivire (2011) assumed the extensive upper tropospheric warming as the forcing of the circulation response. Whether this is true or not was investigated by looking into the temperature tendency (diabatic vs. adiabatic) in our instantaneous CO_2 doubling experiments. It turns out that the broad upper tropospheric warming expansion in the subtropics is a consequence of the circulation change (rather than the cause) and is primarily dynamically-driven by the intensification of transient eddy momentum flux convergence and resulting anomalous descending motion in this region. Chapter 3 also tracked the day-by-day sequential response in the jet streams and found that the poleward displacement of the tropospheric jets takes place after the intensification of the subpolar westerlies in the stratosphere and the enhancement of the tropospheric transient eddy momentum flux convergence. This 'downward propagation' process is similar to Baldwin and Dunkerton (2001) which demonstrated from observations that anomalous weather regimes in the troposphere and at the surface follow the extreme events in the stratosphere. This similarity suggests the importance of the stratosphere and its coupling with the troposphere in the circulation adjustment in our model experiments.

The stratospheric influence on the tropospheric circulation has been widely recognized in both observational and modeling studies in the last decade. The concept of annular modes (AMs) was brought up in Thompson et al. (2000) and unifies the large-scale variability in the extratropics in both the stratosphere and the troposphere in both the Northern and Southern Hemispheres. Baldwin and Dunkerton (2001), by tracking the daily evolution of the AMs, identified from observations that extreme events in the stratosphere are followed by anomalous weather regimes in the troposphere and at the surface with a time delay. Kushner and Polvani (2004), by using a simple GCM, elucidated that the stratospheric thermal perturbations (which resemble the stratospheric polar cooling due to ozone depletion) can induce

a mean flow response penetrating from the stratosphere into the mid-troposphere and also demonstrated the crucial role of the tropospheric synoptic eddy feedback in shifting the tropospheric jet. Ineson and Scaife (2009) investigated the mechanisms underlying the European surface climate response to El Niño events and demonstrated a global teleconnection pathway from the Pacific region to Europe via the stratosphere. Several mechanisms have been proposed to understand how the stratosphere can impact the troposphere including the downward control theory (Haynes et al., 1991), the direct potential vorticity inversion (Hartley et al., 1998), changes in index of refraction (e.g., Perlwitz and Harnik, 2003; Simpson et al., 2009) and eddy-mediated feedbacks (e.g., Kushner and Polvani, 2004; Song and Robinson, 2004). (Song and Robinson (2004) also suggested the importance of the direct role of planetary waves and stated that the 'downward control through secondary circulation with eddy feedback' doesn't offer a complete dynamical explanation.)

As for global warming, a number of studies have suggested that the tropospheric circulation response to increased greenhouse gases critically depends on the stratosphere and its dynamical interaction with the troposphere. Sigmond et al. (2004) studied the climate effects of middle-atmospheric and tropospheric CO_2 doubling separately using the European Centre Hamburg Model (ECHAM) middle-atmosphere climate model with prescribed sea surface temperatures (SSTs). They found strengthened Northern Hemisphere (NH) midlatitude tropospheric westerlies as a consequence of a uniform CO_2 doubling everywhere in the atmosphere and attributed this mainly to the middle-atmosphere CO_2 doubling. Sigmond and Scinocca (2010) found that different stratospheric basic states (controlled by different parameterization settings of orographic gravity wave drag) can result in distinct NH circulation responses to CO_2 increase.

Figure 4.1 is the same as Figure 3.7(b) and shows the day-by-day evolution of the zonal mean zonal wind anomalies averaged in the extratropics between 30^oN

and 70^{o}N during January-February-March-April (JFMA) of year 1 in the ensemble model simulations for the case following the CO_2 doubling minus the case with control CO_2 concentration. It is shown as a function of time and pressure level and is smoothed with a 5-day temporal running average. Based on Fig. 4.1, we define three phases during this 120-day period of transient adjustment in the NH. Phase 1 roughly covers the first month after the instantaneous doubling of CO_2 on January 1st and shows an easterly anomaly in the stratospheric subpolar region. Phase 2 presents a transition into a westerly acceleration in the stratosphere which takes place in February. Phase 3 includes March and April and features a 'downward propagation' of the westerly anomalies from the stratosphere to the troposphere and a poleward tropospheric jet displacement associated with that. In this paper, we analyze the dynamical mechanisms involved in each of the three phases, in particular, what drives the easterly (westerly) acceleration in the stratosphere in Phase 1(2) and what brings down the anomalous westerly acceleration signal from the stratosphere to the troposphere and leads to the poleward displacement of the tropospheric zonal jets in Phase 3. There are several mechanisms that have been raised to understand the circulation shift in response to global warming such as the increase in eddy phase speed (Lu et al., 2008; Chen et al., 2008), the rise in tropopause height (Lorenz and DeWeaver, 2007) and the increase in eddy length scale (Kidston et al., 2010, 2011). We examine all the above possible mechanisms based on our model simulations and see whether or not they make impacts during the transient process. This diagnosis will provide an unified assessment of all the possible mechanisms within the same framework. It has been shown in Chapter 3 that the process of transient adjustment is crucial in setting up the quasi-equilibrium response afterwards and thus understanding the dynamical mechanisms involved in this transient process is important in better understanding the climate change simulation results in CMIP3/IPCC AR4 coupled climate

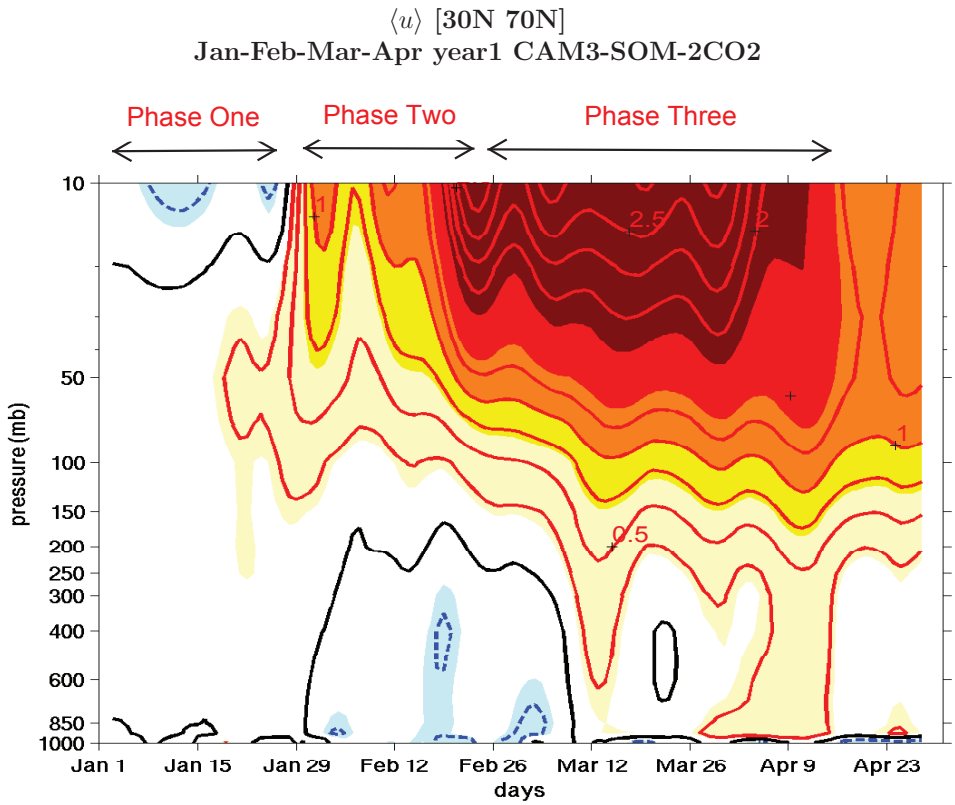

Figure 4.1: Day-by-day evolution of the zonal mean zonal wind averaged over [30N 70N] as a function of day and pressure level during January-February-March-April (JFMA) in year 1. Three phases are defined during this transient adjustment process.

models.

In section 4.2 we present the diagnostic methodologies that have been used in this study as well as the climatological simulation results from CAM3-SOM. Section 4.3 analyzes the dynamical mechanisms underlying each of the three phases during the transient adjustment process. Conclusions and discussions are presented in section 4.4.

4.2 Diagnostic Methodology and and Climatological CAM3-SOM Simulations

4.2.1 Eliassen-Palm (EP) Flux and Its Convergence

The quasi-geostrophic (QG) EP flux in spherical and pressure coordinate is defined as:

$$F_{(\phi)} = -acos\phi(\langle uv\rangle - \langle u\rangle\langle v\rangle) \quad (4.1)$$

$$F_{(p)} = afcos\phi\frac{\langle v\theta\rangle - \langle v\rangle\langle\theta\rangle}{\langle\theta\rangle_p} \quad (4.2)$$

where f is the Coriolis parameter and θ is potential temperature (Edmon et al., 1980). Eddy momentum flux and heat flux are denoted by $\langle uv\rangle - \langle u\rangle\langle v\rangle$ and $\langle v\theta\rangle - \langle v\rangle\langle\theta\rangle$, respectively, where the angle brackets in this study follow the same notation in previous chapters and denote zonal averages. The northward component of $\vec{F}$, $F_{(\phi)}$, is minus the northward flux of zonal momentum by the eddies while the vertical component, $F_{(p)}$, is proportional to the meridional flux of potential temperature. The direction of the flux vectors, ($F_{(\phi)}$, $F_{(p)}$), generally indicates the propagation of waves and the flux divergence, denoted by $\frac{1}{acos\phi}\nabla\cdot\vec{F} = \frac{1}{acos\phi}\{\frac{1}{acos\phi}\frac{\partial}{\partial\phi}(F_{(\phi)}cos\phi) + \frac{\partial}{\partial p}F_{(p)}\}$, measures the wave forcing on the zonal mean flow. The relationship between the wave forcing and the zonal mean flow is presented in the Transformed Eulerian Mean (TEM) framework and the TEM zonal momentum equation is written as:

$$\frac{\partial\langle u\rangle}{\partial t} - \big[f - \frac{1}{acos\phi}\frac{\partial}{\partial\phi}(\langle u\rangle cos\phi)\big]\langle v\rangle^* = \frac{1}{acos\phi}\nabla\cdot\vec{F} \quad (4.3)$$

where $\langle v\rangle^*$ is the meridional component of the residual mean circulation defined as $\langle v\rangle^* = \langle v\rangle - \frac{\partial}{\partial p}(\frac{\langle v\theta\rangle - \langle v\rangle\langle\theta\rangle}{\langle\theta\rangle_p})$ (Andrews et al., 1987). The Brewer-Dobson circulation, characterized by upwelling motion in the tropics and poleward and downwelling motion in the extratropics, is regarded as a Lagrangian mean circulation and is

usually approximated by the residual circulation of the TEM equations (Dunkerton, 1978). In the NH winter, the EP flux divergence usually imposes a westward forcing on the zonal mean flow due to the breaking and dissipation of vertically propagating planetary waves and is primarily responsible for the decceleration of the polar night jets in the stratosphere. This decceleration tendency is mainly balanced by the Coriolis torque associated with the residual circulation. It is also noted that the dissipative forcing including the orographic gravity wave drag can be large in the subtropical lower stratosphere and high latitude upper stratosphere ($\approx$ 2-3 m/s/day) (e.g., Monier and Weare, 2011) and contributes to an imbalance in Equation 4.3.

4.2.2 Spectral and Cross-spectral Analysis

In order to identify the dominant waves during the transient adjustment process, the EP flux is decomposed into different zonal wave numbers as the following:

$$u(\lambda) - \langle u \rangle \quad \xrightarrow{FT} \quad \sum_{k=0}^{k_{max}} \hat{u}(k) \tag{4.4}$$

$$(u - \langle u \rangle)(v - \langle v \rangle) \quad \xrightarrow{FT} \quad 2\mathrm{Re} \sum_{k=0}^{k_{max}} \hat{u}(k) \cdot \hat{v}^*(k) \tag{4.5}$$

where λ is longitude and k is zonal wave number. $\hat{u}(k)$ ($\hat{v}(k)$) is the Fourier transform (FT) of the zonal (meridional) eddy velocity and $\hat{v}^*(k)$ denotes the complex conjugate of $\hat{v}(k)$. The same methodology applies to the meridional heat flux.

In addition, following Randel and Held (1991), a phase speed spectrum for eddy momentum flux convergence is computed. We first compute the zonal wave number (k)-frequency (ν) co-spectra of (u, v) using the daily data of u and v. The wave number (k)-angular phase speed ($C_{p,a}$) co-spectra is then defined and transformed from the k-ν co-spectra by conserving the total power of momentum flux convergence, where $C_{p,a}$ here is defined as $C_{p,a} = \frac{\nu a cos\phi}{k}$. Finally the phase

speed spectrum of momentum flux convergence is constructed by summing over all the zonal wave numbers and is plotted as a function of latitude and angular phase speed.

4.2.3 Linear Quasi-geostrophic (QG) Refractive Index

The linear QG refractive index is a useful predictor and diagnostic for the propagation of planetary waves and has been widely used in various climate states to help interpret the behavior of waves and their interaction with the mean flow (e.g., Charney and Drazin, 1961; Matsuno, 1970; Butchart et al., 1982; Chen and Robinson, 1992; Lorenz and Hartmann, 2001; Seager et al., 2003a; Simpson et al., 2009; Harnik et al., 2010; Sigmond and Scinocca, 2010). Karoly and Hoskins (1982) demonstrated that under linear Wentzel-Kramers-Brillouin (WKB) theory waves are refracted by the gradients of linear refractive index and thus tend to propagate from regions of low refractive index to regions of high refractive index. Although WKB theory requires the wavelength of the perturbations to be smaller than the scale of the basic state, which may not be well satisfied in the stratosphere, interpretations of wave propagation in the stratosphere using the index of refraction have been successful (e.g., Matsuno, 1970; Perlwitz and Harnik, 2003; Shaw et al., 2010).

Matsuno (1970) provided an analytical formula for the stationary QG linear refractive index by assuming the atmosphere isothermal (thus constant buoyancy frequency, N). This assumption is a reasonable approximation for the stratosphere but may not for the troposphere. The zonal mean QG refractive index for both stationary and transient eddies with phase speed C_p is written as:

$$n^2_{\text{ref}} = \frac{a\langle q_\phi \rangle}{\langle u \rangle - C_p} - \frac{k^2}{cos^2\phi} - \frac{f^2 a^2}{4N^2 H_o^2} \tag{4.6}$$

$$\langle q_\phi \rangle = 2\Omega cos\phi - \frac{\partial}{\partial \phi}\Big[\frac{1}{acos\phi}\frac{\partial \langle u \rangle cos\phi}{\partial \phi}\Big] + \frac{f^2 a}{R}\frac{\partial}{\partial p}\Big(\frac{p\langle \theta \rangle}{\langle T \rangle}\frac{\langle u \rangle_p}{\langle \theta \rangle_p}\Big) \tag{4.7}$$

where R_d is the dry air gas constant (287 J/kg/K), q_ϕ is the meridional potential vorticity (PV) gradient and H_o is the scale height of pressure ($H_o = 7$ km). The n^2_{ref} is dimensionless in Equation (4.6) which is the same as that in Simpson et al. (2009).

Furthermore, we also make use of a linear quasi-geostrophic (QG) model to diagnose the wave propagation characteristics of a two-dimensional zonal mean basic state (Harnik and Lindzen, 2001). The model is basically a QGPV conservation equation with a specified eddy phase speed (C_p) and zonal wave number (k) and numerically calculates the steady-state eddy fluxes purely via the index of refraction. The model also separates the index of refraction (n^2_{ref}) into the vertical (m^2_z) and meridional wave numbers (l^2_y) which serve as a more accurate indicator of wave propagation in the vertical and meridional directions (e.g., Harnik and Lindzen, 2001; Perlwitz and Harnik, 2003; Shaw et al., 2010).

4.2.4 Climatological CAM3-SOM Simulations

The circulation in the NH winter stratosphere is largely modulated by the planetary waves generated in the troposphere due to the orographic forcing and large-scale zonally asymmetric diabatic heating near the surface. Figure 4.2(a) shows the climatological QG EP flux and its convergence in February[1] from the CAM3-SOM simulations. The EP flux vectors in this study are all normalized by the basic state density as in Edmon et al. (1980) to better display the wave activity in the stratosphere. As can be seen waves are generated in the lower troposphere and propagate upward into the stratosphere. These upward propagating Rossby waves in the extratropics are always refracted equatorward toward the critical layer where

[1]The climatology is shown for February here for a better comparison with the anomalies in February of year 1 to be shown later. The climatological features in February are similar to January-February-March averages.

the eddy phase speed[2] equals the zonal mean flow velocity and the waves are all absorbed there. This feature is well presented by the EP flux vectors.

The maxima in climatological EP flux convergence, i.e. $\frac{1}{acos\phi}\nabla \cdot \vec{F} < 0$, in general occur in regions where waves are absorbed or dissipated, for example, north of the subtropical critical layer, in the high latitude middle troposphere and in high latitudes below the polar jet. However, the modeling experiments with CAM3 fail to get the convergence in the stratospheric high latitudes correct (e.g., Monier and Weare, 2011). In fact, as shown in Fig. 4.2(a), the climatological simulations produce a divergence of EP flux (i.e., $\frac{1}{acos\phi}\nabla \cdot \vec{F} > 0$) which imposes an unrealistic westerly acceleration tendency in the polar stratosphere as a result of the amplification of the momentum flux and the under-estimate of the heat flux near the model lid of CAM3 (e.g., Sassi et al., 2010). The upper boundary condition is commonly applied in general circulation models and the upper model lid in CAM3 is at about 2.9mb where the vertical velocity is assumed zero. The effects of this artificial upper boundary on climate model simulations in both the stratosphere and the troposphere have been long recognized (e.g., Boville, 1984; Boville and Cheng, 1988; Shaw and Perlwitz, 2010). The upper model lid leads to reflection of vertically propagating wave activity, changes the meridional/vertical phase structures, causes increased (decreased) poleward eddy momentum (heat) flux, and results in a net westerly forcing on the zonal mean flow (Boville and Cheng, 1988). Although Rayleigh friction is usually applied at the model top to damp vertically propagating planetary waves, it can't prevent the reflection of all the wave activities. Sassi et al. (2010) compared the present-day simulations between CAM3 and the Whole Atmosphere Community Climate Model version 3 (WACCM3) (its vertical domain extends to 5.9×10^{-6}mb) and found substantial differences in the zonal mean state

[2]The dominant waves in the stratosphere are planetary stationary waves with phase speed of 0 m/s while those in the troposphere are transient eddies with typical phase speed of 8 m/s. Contours of $C_p = 0$ m/s and 8 m/s are highlighted in Fig. 4.2(a).

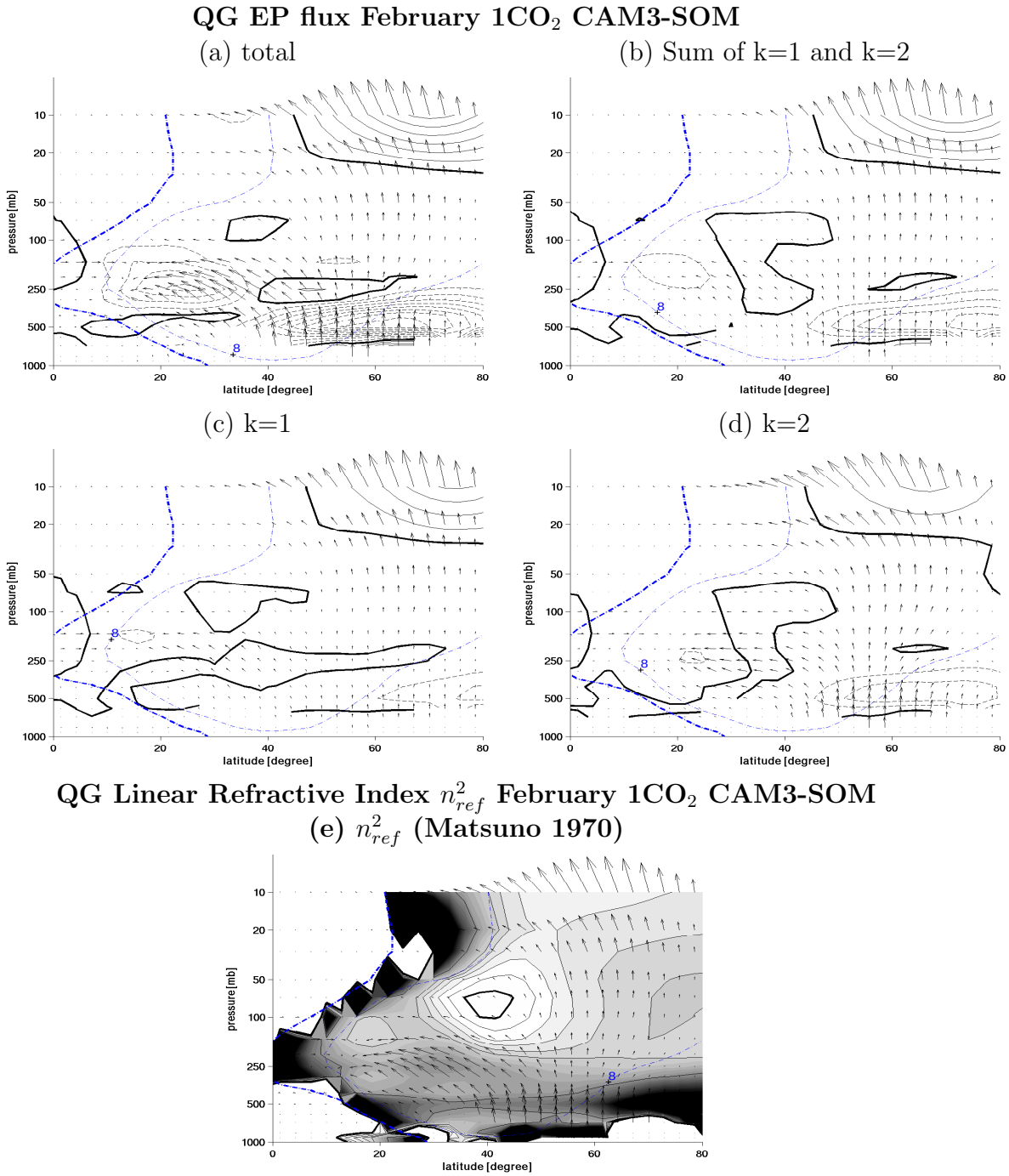

Figure 4.2: The climatological simulations of the QG EP flux (vectors) and its convergence (black contours) for (a) all the waves, (b) k=1 plus k=2, (c) k=1 and (d) k=2 for February from the CAM3-SOM with blue contours showing the critical layer for stationary (C_p = 0 m/s) and transient (C_p = 8 m/s) eddies. The contour intervals for EP flux convergence are 2m/s/day. (e) shows the corresponding calculated index of refraction (black contours and shadings).

of the stratosphere and the behavior of the stratospheric variability, such as the life cycle of weak stratospheric vortex events, and their influence on the tropospheric circulation. Sigmond and Scinocca (2010) demonstrated that with different basic states in the lower stratosphere the climate change response in the NH can be different as well. This suggests caution in interpreting the circulation behavior in CAM3-SOM as a consequence of CO_2 doubling.

Figure 4.2(c)(d) shows the contributions from zonal wave number $k = 1$ and $k = 2$ respectively, the sum of which is shown in Fig. 4.2(b). The agreement between Fig. 4.2(a) and Fig. 4.2(b) in the stratosphere indicates the dominance of the planetary-scale long waves ($k = 1$ and 2) there, which is consistent with the theoretical work of Charney and Drazin (1961). Figure 4.2(e) shows the calculated n^2_{ref} as defined in Equation (6) superimposed with the corresponding EP flux vectors in the CAM3-SOM simulations for the case of planetary-scale stationary waves in the stratosphere with $C_p = 0$. The n^2_{ref} in Equation (6) is dominated by the contribution from $\frac{a\langle q_\phi \rangle}{\langle u \rangle - C_p}$, while the term carrying the zonal wave number $-\frac{k^2}{cos^2\phi}$ is much smaller than the other terms and is neglected. The n^2_{ref} is positive almost everywhere in the extratropics except for the region of negative values in the midlatitude lower stratosphere at about 40^oN between 70mb and 100mb. Matsuno (1970) noted the significance of this minimum in refractive index and argued that it creates a partial wave guide for vertical propagation on its poleward side. In addition, the n^2_{ref} increases almost monotonically from high to low latitudes and becomes infinitely large as the waves reach the zero wind line (critical layer) which is highlighted in blue in Fig. 4.2(e). As can be seen, the propagation of waves, indicated by the EP flux vectors, generally follows the gradients of n^2_{ref}, and the waves are indeed refracted equatorward toward increasing n^2_{ref}. The linkage between wave propagation and the index of refraction appears to be robust for the climatological basic state in both the stratosphere and the troposphere.

4.3 Three-Phase Atmospheric Transient Circulation Adjustment Process and its Dynamics

As shown in Fig. 4.1, three phases are defined during the first 120 days of transient adjustment in January-February-March-April (JFMA) in year 1. At the end of this transient adjustment process, the extratropical circulation response resembles that in the quasi-equilibrium state and the tropospheric jet streams are shifted poleward. Figure 4.3 shows the latitude-pressure level plot of the $\langle T \rangle$ and $\langle u \rangle$ anomalies in Phase 1 (January), 2 (February) and 3 (March and April), respectively. The climatological $\langle T \rangle$ and $\langle u \rangle$ on January 1st is also shown in Fig. 4.3 as a reference. In the following we discuss the dynamical mechanisms involved in each of the three phases.

4.3.1 Phase One (January): Stratospheric Subpolar Easterly Anomaly

An easterly anomaly in the stratospheric high latitudes, together with a westerly anomaly in the low latitudes occur in the first few days after the instantaneous doubling of CO_2 on January 1st. This is a fast purely radiatively-driven response. The stratosphere cools with increased CO_2 and resulting increased longwave radiation to space. In general, with a uniform CO_2 increase, the stratosphere cools more (less) where the control basic state temperature is warmer (colder). Thus the stratospheric cooling anomaly increases with height and also varies with latitude. As shown in Fig. 4.3(a), the NH basic state temperature in the stratosphere increases with latitude but only up to the midlatitudes and then decreases towards the North Pole where there is no incoming solar radiation. The radiative response basically follows the control temperature structure in the stratosphere, with more longwave radiation emitted out to space in the northern middle latitudes, causing

maximum cooling there and generating a poleward (equatorward) flow and a westerly (easterly) anomaly in the low (high) latitudes due to geostrophic adjustment (shown in Fig. 4.3(c)(d)). In Phase 1 the circulation response is primarily in the stratosphere.

It is noted here that the radiative response in the SH is different from that in the NH because of the difference in basic state temperature. Here the stratospheric basic state temperature has a minimum at the Equator and monotonically increases towards the South Pole as a consequence of absorption of incoming solar radiation by the ozone during summer. This reversed temperature gradient in the stratosphere is consistent with the climatological easterlies in the southern summer (shown in Fig. 4.3(b)). After the CO_2 is increased, the SH stratosphere cools most at the pole and least at the Equator, reducing the meridional temperature gradient causing a poleward flow and a westerly zonal wind anomaly. Because of the weak planetary forcing in the southern summer, the stratospheric circulation response is primarily controlled by the radiative forcing until the zonal wind anomaly penetrates into the middle troposphere where the transient eddies are expected to respond and impact the whole troposphere. In contrast, the planetary wave activity in the NH and its upward propagation greater modulates the stratospheric circulation there as to be discussed below.

4.3.2 Phase Two (February): Stratospheric Westerly Acceleration

In February there is now a westerly anomaly in the NH stratosphere which is consistent with more cooling in the stratospheric subpolar region (shown in Fig. 4.3(e)(f)). A diagnosis of the QG EP flux and the TEM zonal momentum equation indicates that the westerly acceleration in the stratosphere is now mainly eddy-driven. Figure 4.4(a) shows the QG EP flux anomaly in Phase 2 and the combined

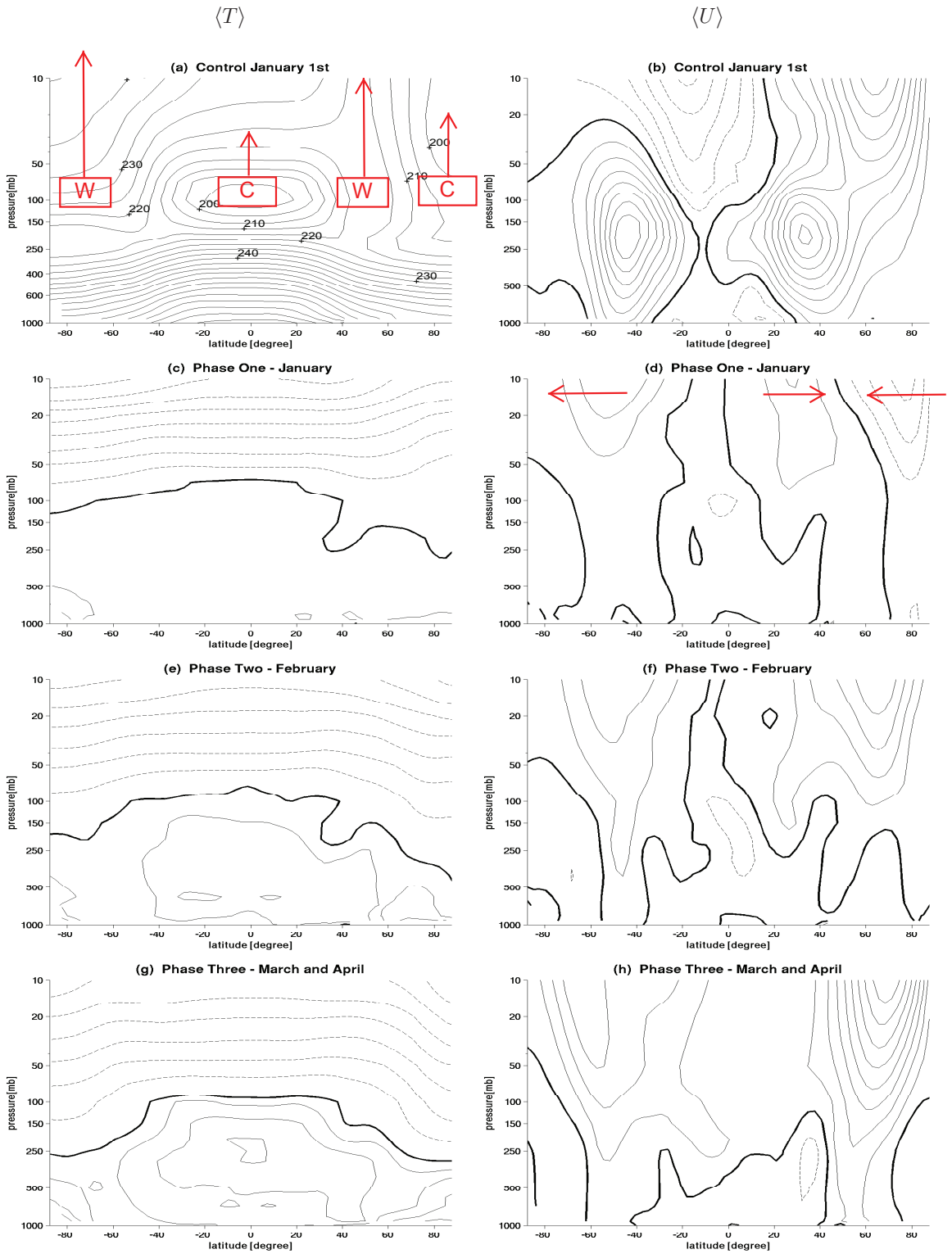

Figure 4.3: (a)(b) Climatological $\langle u \rangle$ and $\langle T \rangle$ on January 1st, and anomalies in $\langle u \rangle$ and $\langle T \rangle$ for Phase One (c)(d), Phase Two (e)(f), and Phase Three (g)(h) during the transient adjustment in the CAM3-SOM-2CO2 simulations. The contour intervals are 5 K for (a), 5 m/s for (b), +0.25 K (-0.5 K) for (c), 0.25 m/s for (d), +0.25 K (-1 K) for (e)(g) and 0.5 m/s for (f)(h).

contribution from planetary wave 1 and wave 2 is shown in Fig. 4.4(b). The agreement between Fig. 4.4(a) and Fig. 4.4(b) indicates that the dominant waves are, as expected, of planetary scale. Figure 4.4(c)(e)(f) shows the total EP flux convergence anomaly ($\frac{1}{acos\phi}\nabla\cdot\vec{F}$), its contribution from the horizontal convergence of eddy momentum flux ($\frac{1}{a^2cos^2\phi}\frac{\partial F_{(\phi)}cos\phi}{\partial\phi}$) and from the vertical convergence of eddy heat flux ($\frac{1}{acos\phi}\frac{\partial F_{(p)}}{\partial p}$), respectively, from wave 1. The counterpart from wave 2 is shown in Fig. 4.4(d)(g)(h). These show more equatorward wave propagation from wave 1 and less upward propagation from wave 2. From Fig. 4.4(e), it is found that the westerly acceleration in the stratosphere is mainly caused by the increased equatorward wave refraction and resulting momentum flux convergence anomaly from planetary wave 1. It is also noted that the wave 2 anomaly indicates less upward wave propagation in both the stratosphere and the troposphere.

To understand why more planetary waves are refracted equatorward as a consequence of the CO_2 increase, the index of refraction $n^2_{\rm ref}$ is computed, the anomaly of which is shown in Figure 4.5 for $C_p = 0$ m/s using the basic state during Phase 2. It is superimposed with the corresponding EP flux anomaly and the zero wind lines for the $1CO_2$ and the $2CO_2$ runs. The largest equatorward wave refraction occurs in the midlatitude stratosphere between about 50^oN and 60^oN whereas the change in $n^2_{\rm ref}$ is positive (negative) on the poleward (equatorward) side. This is not in agreement with predictions of the linear refraction theory. However, as mentioned in the previous section, the model simulations with CAM3 fail to realistically produce the circulation climatology in the stratosphere possibly because of the artificial model top and resulting downward wave reflection. It is possible that the anomalies in wave propagation, in particular, in the stratosphere, are also influenced by the model upper boundary, and if this is the case, the wave propagation may not follow the index of refraction.

Sigmond et al. (2008) and Sigmond and Scinocca (2010) found distinct NH cir-

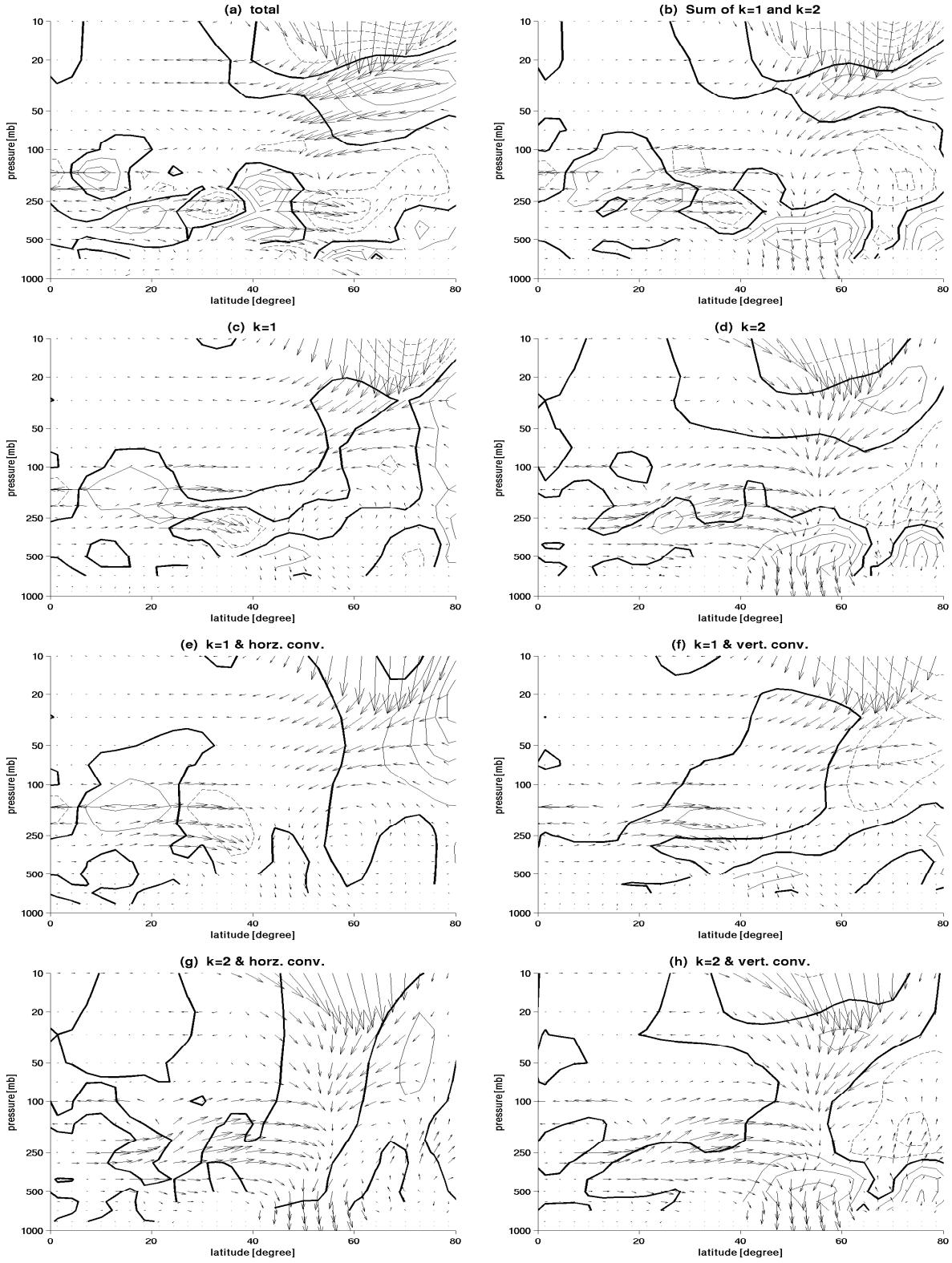

Figure 4.4: QG EP flux and its convergence anomaly ($2CO_2$-$1CO_2$) in Phase 2 (February) from (a) all the wave numbers, (b) wave 1 plus wave 2; (c) wave 1 and (d) wave 2. The contours in (e)(f) show the meridional divergence of eddy momentum flux and the vertical divergence of eddy heat flux, respectively, for planetary wave 1 with the vectors the same as in (c). The counterpart for wave 2 is shown in (g)(h). The contour interval is 0.1 m/s/day.

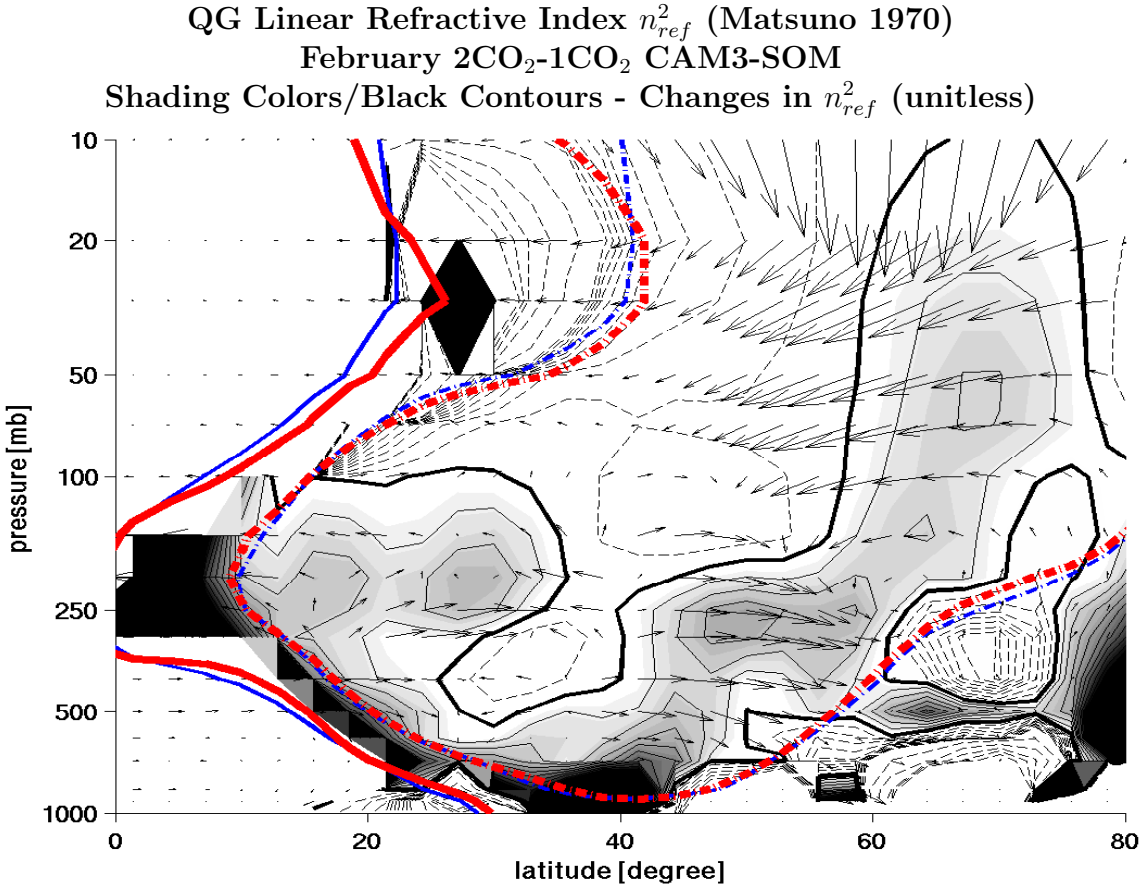

Figure 4.5: Changes in index of refraction n^2_{ref} (shown in black contours) and EP flux vectors in Phase 2 (February) in the Northern Hemisphere. Solid contours and shadings denote positive trends in n^2_{ref} while dashed contours shown negative trends. The zero wind lines (8 m/s zonal wind lines) for the $1CO_2$ and the $2CO_2$ runs are highlighted in solid (dashed) blue and red, respectively.

culation responses to increased CO_2 for different parameterizations of orographic gravity wave drag and resulting different basic states. Weak (strong) orographic gravity wave drag is usually associated with a strong (weak) westerly climatology in the lower stratosphere and as a result of CO_2 increase, the NH polar vortex strengthens (weakens) and a hemispheric-wide (localized) meridional dipole pattern in mean sea level pressure exists. They used the changing index of refraction as explanations and argued that the region of negative n^2_{ref} in the subtropical lower stratosphere, which is usually considered a barrier to equatorward wave propagation, is the key factor and disappears when the climatological zonal wind is strong. This allows more eddies to propagate equatorward from the stratospheric subpolar region, leading to a net eddy forcing divergence and a subpolar westerly acceleration tendency whereas not much change was found for the case of weak westerly climatology. Different from what Sigmond and Scinocca (2010) found, we didn't find any significant change of n^2_{ref} in the region of the subtropical lower stratosphere where n^2_{ref} is negative but, nonetheless, more waves are refracted equatorward in our model simulations.

4.3.3 Phase Three (March and April): Poleward Displacement of Tropospheric Jets

As shown in Fig. 4.1, Fig. 4.3 and Figure 3.8 in Chapter 3, the jet stream anomaly in the troposphere starts to shift poleward in early March. This circulation change in the troposphere appears to follow the westerly flow acceleration in the stratosphere and the intensification of transient eddy momentum flux convergence in the subtropical middle and upper troposphere. This is consistent with the conclusion in Kushner and Polvani (2004) which demonstrated that the residual circulation in the stratosphere can induce the zonal wind anomaly to penetrate into the mid-troposphere and that the transient eddies are crucial in shifting the tropospheric

jet streams.

Previous studies have proposed hypotheses to interpret the tropospheric jet shift in response to global warming. The major hypotheses include: (1) an increase in eddy phase speed (Lu et al., 2008; Chen et al., 2008); (2) a rise in tropopause height (Lorenz and DeWeaver, 2007); (3) an increase in eddy length scale (Kidston et al., 2011. Another possibility comes from the idea of changing index of refraction which has been used successfully in understanding the transient eddy propagation during El Niños (Seager et al., 2003a; Harnik et al., 2010) as well as solar cycles (Simpson et al., 2009). In Phase 3, based on our modeling experiments with CAM3-SOM, we look into each of the above possible mechanisms and see whether or not they make impacts. This study provides an unified and comparable assessment of all the possible mechanisms within the same framework.

4.3.3.1 Eddy Phase Speed

Lu et al. (2008) and Chen et al. (2008) identified an increase in eddy phase speed in the GFDL CM2.1 model simulations under the 'business-as-usual' A2 scenario in which the CO_2 concentration reaches 800 ppmv at the end of the 21st century. They argued that this eddy phase speed increase causes the critical line, subtropical breaking region, transient eddy momentum flux convergence and tropospheric zonal jets to move poleward. Here we follow the computational methodology for the eddy phase speed cross-spectra as in Randel and Held (1991) and Chen and Held (2007) and see whether this hypothesis helps explain the shift in the jet position in our modeling experiments.

Figure 4.6 shows the co-spectra of eddy momentum flux convergence at 250mb during the first 120 days of transient adjustment in January-February-March-April of year 1 as a function of angular phase speed ($C_{p,a}$) and latitude along with the 250mb zonal wind distribution. The difference between the $2CO_2$ and the $1CO_2$ runs

is shown in contours while the climatology is shown in color shadings. As expected the climatological co-spectrum shows a divergence in eddy momentum flux in the subtropics and a convergence in the midlatitudes. The 250mb waves are primarily eastward propagating transient waves with angular phase speed of about 10m/s in the NH. In addition, the meridional wave propagation is confined by the subtropical critical layer which is consistent with the linear refraction theory. The transient anomalies in eddy momentum flux convergence co-spectra show a poleward shift in the NH relative to the climatology with an intensification (reduction) on the poleward (equatorward) flank of the climatological maximum position. However, different from what was found in Lu et al. (2008) and Chen et al. (2008), our model experiments with CAM3-SOM don't show any significant increase in eddy phase speed during the transient adjustment process. What's more, we find no significant increase in eddy phase speed in the quasi-equilibrium state either (not shown).

Simpson et al. (2009) found no increase in eddy phase speed in their study investigating the chain of causality on how the stratospheric heating perturbations drive tropospheric circulation anomalies in a simple general circulation model. Rivire (2011) investigated the effect of changing eddy length scale on wave breaking and resulting changes in jet position, and a slightly decreased phase speed was found during the process. Perhaps increased eddy phase speed in response to an increase in CO_2 is model-dependent, but at least in this model it is not an explanation of the tropospheric jet shift.

4.3.3.2 Tropopause Height

Second, as the location of the jet streams and the eddies is closely related to the depth of the troposphere, it is possible that the jet position shift could be induced by a change in tropopause height. Since the scale of the eddies is characterized by the Rossby radius, $L_R = \frac{NH}{f}$, where H denotes the thickness of the troposphere,

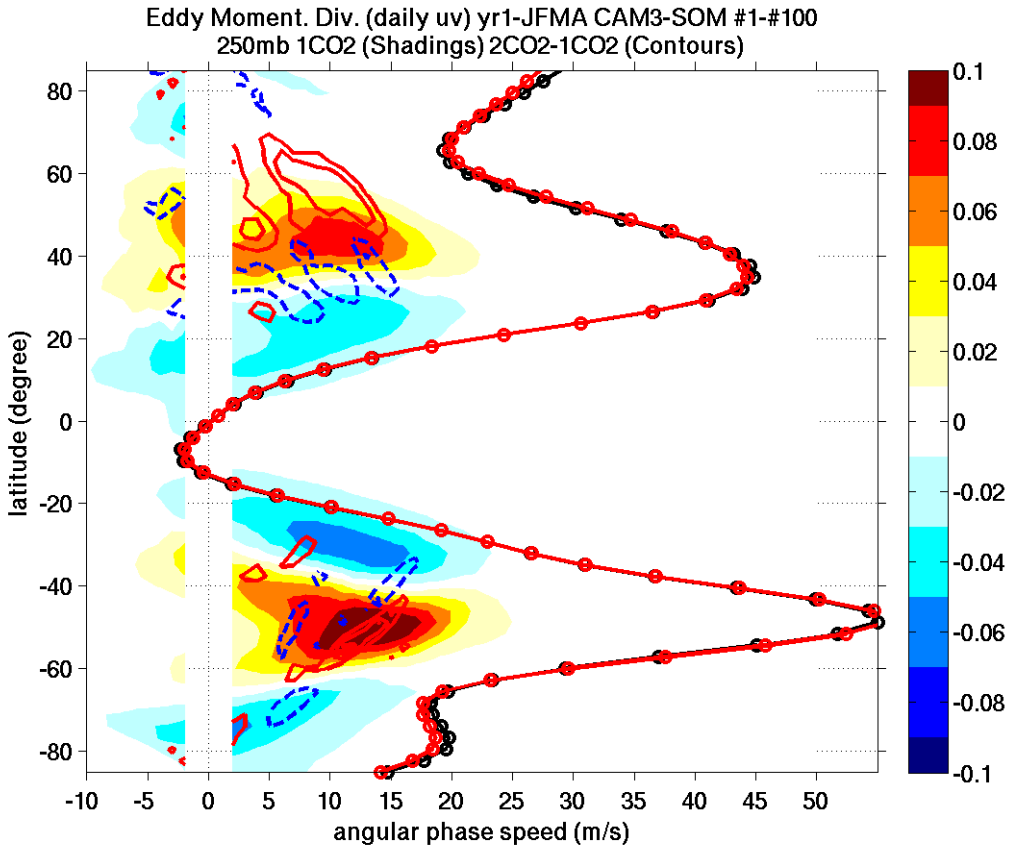

Figure 4.6: Cross spectrum of eddy momentum flux convergence [m/s/day] at 250mb as a function of angular phase speed (m/s) and latitude (degree) in the CAM3-SOM simulations. Contours show the difference between the $2CO_2$ and the $1CO_2$ runs with contour interval of 0.0050 m/s/day. Shadings show the results from the $1CO_2$ runs with positive (negative) values indicating momentum flux convergence (divergence). Black (red) lines show the 250mb $\frac{u}{cos\phi}$ for the $1CO_2$ ($2CO_2$) runs. Following Randel and Held (1991), the spectrum is shown for (absolute) angular phase speeds great than 2 m/s because lower phase speeds are not resolved.

eddies in theory should become larger as the tropopause height is raised. As the baroclinic zone shifts poleward as a consequence of larger eddies, the jets are expected to move toward higher latitudes as well. Observations indicate that the height of the tropopause has gone up by several hundred meters since year 1979, predominantly driven by anthropogenic forcing (Santer et al., 2003). This rising trend in tropopause height has also been found to be closely related to the warming of the troposphere and the poleward expansion of the Hadley Cell (e.g., Santer et al., 2003; Lu et al., 2009). Lorenz and DeWeaver (2007) found similarities in extratropical circulation response between IPCC AR4 coupled models (A2 scenario) and a simple dry GCM when the tropopause height is raised (by about 400 meters), suggesting that the rise in tropopause height is the dominant driver of the extratropical circulation response to global warming although in their experiments the effect of increasing baroclinic instability in the upper troposphere wasn't excluded.

Figure 4.7 shows the day-by-day evolution of the latitudinal shift in 850mb midlatitude jet maximum location and the rise in tropopause height averaged in the midlatitude region between 30^oN and 70^oN. The calculation of tropopause height follows the algorithm in Reichler et al. (2003) and finds the lowest pressure level at which the temperature lapse rate decreases to 2 K/km. Because of the coarse resolution in latitude of CAM3, the zonal mean zonal wind is first interpolated[3] to a finer latitude grid before locating the jet maximum. As a result of CO_2 doubling and the fast radiative stratospheric cooling, the tropopause starts to rise after about 15 days and keeps on rising by about 1mb before it drops at the end of February. Despite these changes in tropopause height, there is not much change in jet maximum position near the surface at this point. In early March, the tropopause height starts to rise again sharply and this time is followed by a poleward shift in the jet position near the surface with a lag of a few days. This is a robust result for

[3]Cubic spline interpolation is used here but the results don't change much for other interpolation schemes.

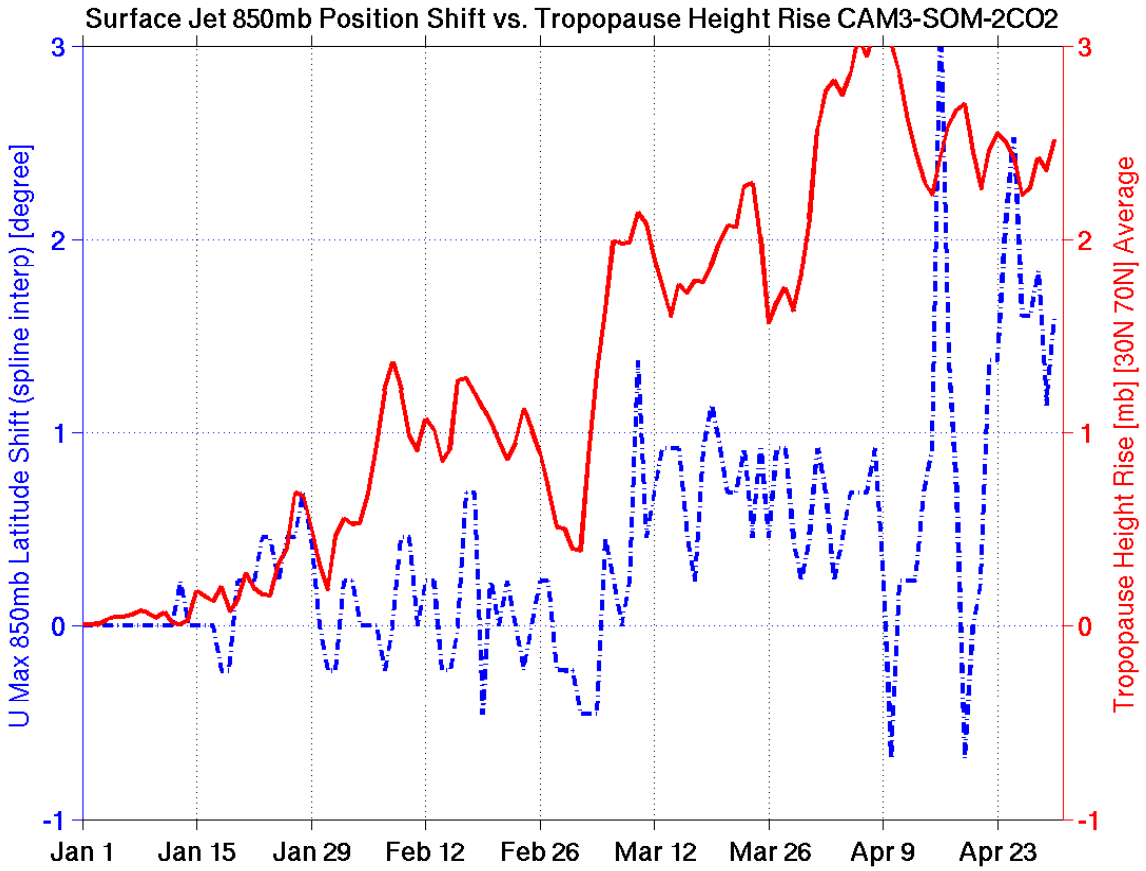

Figure 4.7: Day-by-day evolution of the 850mb jet position shift (blue) vs. the rise tropopause height (red) averaged in the midlatitudes between 30^oN and 70^oN during January-February-March-April in year 1.

the jets at various vertical levels and for tropopause height at different latitudes. The tropopause, on average, rises by 2 mb while the low-level jet moves by about 1^oN in March. Although the rise in tropopause height leads the low-level jet shift in early March, there is overall little correlation between the time history of these two quantities. The dynamics underlying the conventional theory always connects the tropopause height rise with the poleward displacement of the tropospheric jet streams via an increase in eddy length scale, the day-by-day evolution of which is further investigated in the following.

4.3.3.3 Eddy Length Scale

Kidston et al. (2010) found a robust increase in eddy length scale in the A2 scenario simulation of the future climate among an ensemble of CMIP3/IPCC AR4 models. Wu et al. (2010) also noticed this increase in eddy length scale in the GFDL CM2.1 model under the A1B scenario and found that the increased larger eddies are partially responsible for the increased poleward energy transport carried by the storm tracks in the future climate. Kidston et al. (2011) refined the idea that an increase in eddy length scale can cause the jet streams to move poleward rather than vice versa, which is confirmed in a simple barotropic model experiment. Rivire (2011) emphasized the role of enhanced upper-tropospheric baroclinic instability in the poleward shift of the jet streams via changes in eddy length scale and anticyclonic/cyclonic wave breaking in the global warming scenario.

Following the methodology in Kidston et al. (2010), we calculate the eddy length scale day by day during the transient adjustment process. The mean eddy length scale is defined as $\bar{L}_{\text{eddy}} = \frac{2\pi a cos\phi}{\bar{k}}$ with $\bar{k}$ measuring the energy weighted zonal wave number $\bar{k} = \frac{\sum_k k \cdot |\hat{v}(k)|^2}{\sum_k |\hat{v}(k)|^2}$ where $|\hat{v}(k)|^2$ denotes the high-pass filtered[4] meridional component of the eddy kinetic energy in wave number (k) spectrum. Figure 4.8 plots the day-by-day evolution of the change in eddy length scale $\bar{L}_{\text{eddy}}$ averaged in the midlatitudes between 30^oN and 70^oN at 500mb along with the jet shift at 500mb. The evolution in eddy length scale is noisy compared with that of the jet shift and tropopause height rise but clearly shows a rapid transition from a negative anomaly to a steady positive anomaly starting in early March. The increase in eddy length scale on average reaches about 60km at the end of March and in April. The time sequence in Fig. 4.8 indicates that the increase in eddy length scale takes place after the jet shift in the middle troposphere, with a time lag of about two days. This time sequence is robust for the jet shift and the eddy length scale increase at

[4]The high-pass filter retains synoptic time scales of 2-8 days.

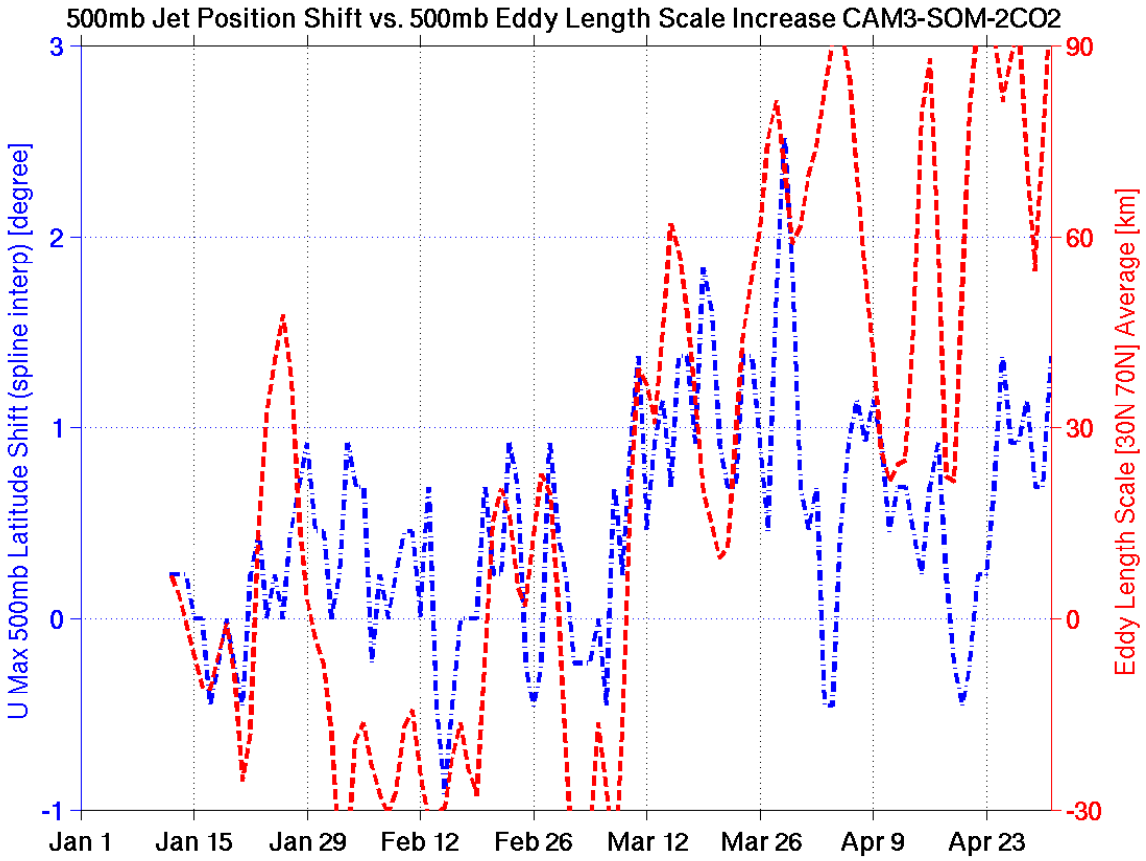

Figure 4.8: Day-by-day evolution of the 500mb jet position shift (blue) vs. the change in eddy length scale (red) averaged in the midlatitudes between 30°N and 70°N during January-February-March-April in year 1. A 1-2-1 temporal smoothing has been applied for the time evolution of the eddy length scale anomaly.

different vertical levels, which implies that during the transient adjustment process the eddy length scale increase is a consequence of the tropospheric jet shift. This can be interpreted in terms of the linear baroclinic instability theory: the poleward displacement of the tropospheric jet streams shifts the maximum vertical wind shear and the region for transient eddy generation poleward and thus increases the length scale of the transient eddies.

The time sequence between the jet shift and the increase in eddy length scale in the extratropical troposphere supports the idea that the eddy length scale increase

occurs as a consequence of the jet poleward shift in our modeling experiments. While the mechanism proposed by Kidston et al. (2011) is scientifically valid, it might not make impacts during the circulation adjustment process in this model. In addition, as the increase in eddy length scale follows the jet shift, the dynamical mechanisms linking the tropopause height rise and the jet shift remain unclear.

4.3.3.4 Linear Refractive Index

Simpson et al. (2009) successfully used the index of refraction to diagnose and interpret how the changing eddy propagation and eddy momentum flux drives anomalous tropospheric circulation step by step as a result of initial stratospheric heating perturbations using a simple GCM. The index of refraction, in particular, the meridional wave number calculated from the linear QG model was also used to understand the equatorward displacement of the transient eddies and its associated dynamical mechanisms during El Niños (Seager et al., 2003a; Harnik et al., 2010). It is shown that, as a consequence of the equatorward shift of the subtropical jets and resulting changes in meridional wave number, the transient eddies act to persistently maintain the mean flow anomalies via anomalous convergence (divergence) of momentum flux in the subtropical (midlatitude) region.

In this section, we use the linear QG model as in Seager et al. (2003a) and Harnik et al. (2010) to isolate the effect of linear wave refraction and to quantify the eddy feedback to the zonal flow. A zonal wave number of 6 and a phase speed of about 10 m/s is prescribed[5]. The zonal mean zonal wind and temperature fields from each day of the 120-day adjustment process are used as input for the linear QG model, and the corresponding solution for eddy fluxes is calculated for each day. Figure 4.9 shows the day-by-day zonal mean evolution of the zonal flow, the eddy

[5]We have used the same set of model parameters as in Seager et al. (2003a) and Harnik et al. (2010) and have assumed k and C_p constant for the $1CO_2$ and the $2CO_2$ runs. This mechanism of linear wave refraction is different from the previous mechanisms and assumes no changes in eddy properties.

momentum flux convergence output from the linear QG model, and the high-pass filtered eddy momentum flux convergence calculated from the CAM3-SOM runs, respectively, all averaged in the upper and middle troposphere between 150mb and 500mb. A 8-day temporal running average has also been applied to these variables. Figure 4.9(b) shows an organized latitudinal dipole structure in eddy momentum flux convergence starting in early March which tends to persistently accelerate the zonal flow on the poleward flank between 40^oN and 60^oN while decelerate that on the equatorward side. This is similar to the high-pass filtered transient eddy momentum flux convergence calculated from the CAM3-SOM runs, as shown in Fig. 4.9(c), though the latter extends further poleward to about 70^oN. These results clearly indicate a positive feedback between the transient eddies and the zonal flow and the anomalous transient eddy propagation and momentum flux is attributed to the changes in basic state and resulting changes in index of refraction.

The results from the linear QG model suggest the positive feedback between the transient eddies and the zonal flow which persistently maintain the jet displacement in the troposphere. However, because the linear QG model input already includes the eddy feedback, it is not entirely clear what initiates the tropospheric jet shift. This will be further investigated in future work.

4.4 Conclusions and Discussions

As a consequence of instantaneous and uniform doubling of CO_2, the day-by-day evolution of the atmospheric circulation reveals the chain of causality that occurs in the adjustment. This was examined by analyzing the day-to-day and week-to-week forced change over an ensemble of 100 runs with slightly different initial conditions at the time of instantaneous CO_2 doubling. It is found that after a few months of integration, the circulation and thermal responses in the extratropical troposphere resemble the major features seen in the quasi-equilibrium simulations from the

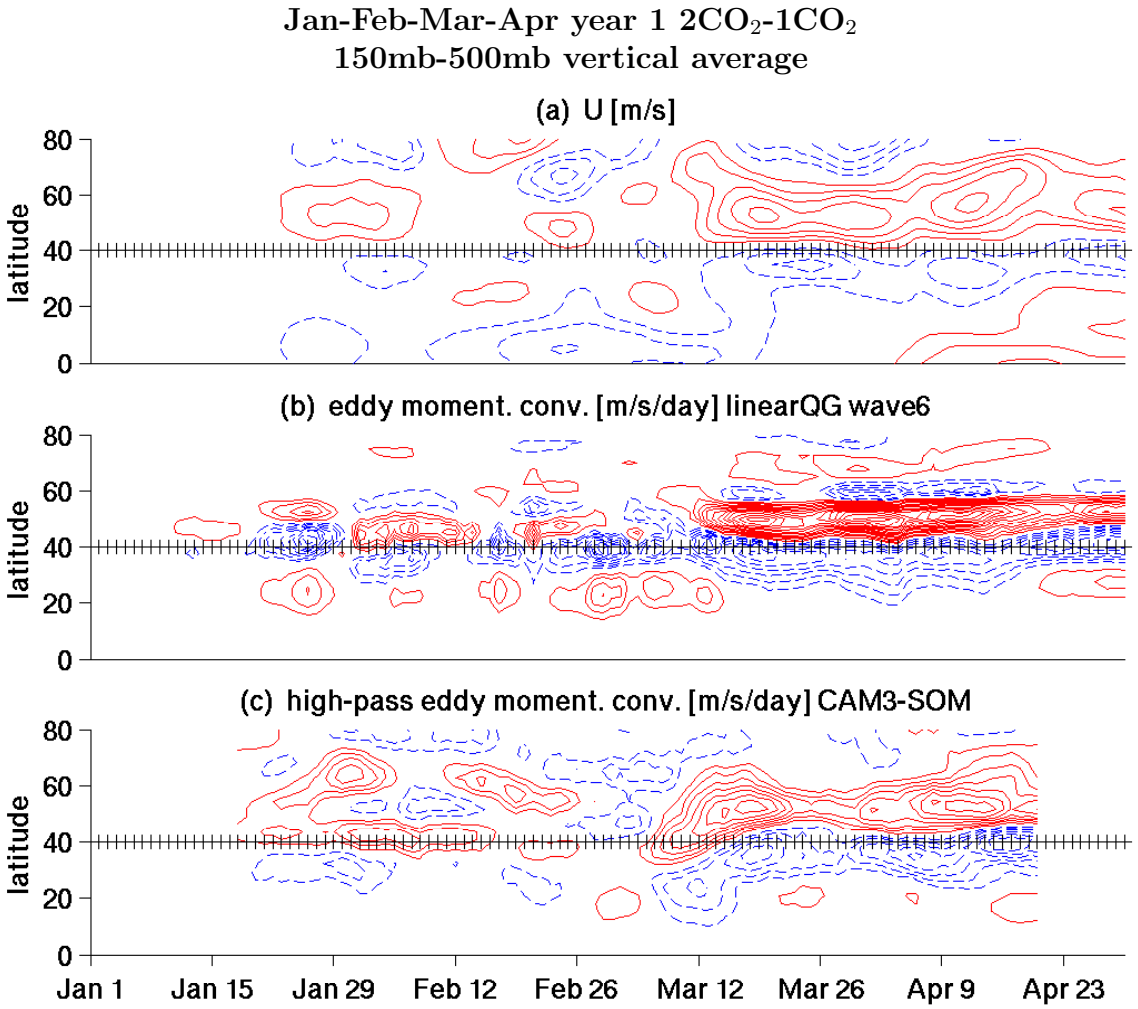

Figure 4.9: The day-by-day zonal mean evolution of (a) the zonal flow, (b) the eddy momentum flux convergence output from the linear QG model, and (c) the high-pass filtered transient eddy momentum flux convergence calculated from the CAM3-SOM runs, all averaged between 150mb and 500mb. A 8-day temporal running average has also been applied. Red solid (blue dashed) contours indicate positive (negative) values. The contour intervals are 0.25 m/s for (a) and 0.05 m/s/day for (b)(c).

CMIP3/IPCC AR4 coupled models using the A1B emission scenario, which suggests the usefulness and relevance of examining the transient adjustment process. Chapter 3 mainly focused on the transient thermal response in the troposphere. It showed that the extensive warming in the upper and middle subtropical troposphere is caused adiabatically by the anomalous descending motion driven by the transient eddy momentum flux anomalies in the troposphere. Here, Chapter 4 further explores the dynamical mechanisms underlying the sequential transient adjustment leading up to the establishment of the circulation response in the extratropical troposphere. From the day-by-day evolution of the zonal mean zonal wind in the extratropics, three phases are defined. The initial response takes place in the stratosphere and has a westerly flow anomaly in the stratosphere low latitudes, together with an easterly anomaly in the northern high latitudes, all is driven radiatively by the CO_2 increase and associated latitudinal gradients of temperature response. It then switches to a westerly flow acceleration throughout the stratosphere in Phase 2 driven by enhanced horizontal momentum flux convergence within the planetary-scale eddies. However, interpreting the eddy propagation anomaly in terms of changes in the index of refraction is not successful. This may be related to the low model upper boundary and possible wave reflection. Phase 3 sees the westerly acceleration propagate downward from the lower stratosphere into the troposphere, followed by the poleward shift of the tropospheric jet streams. Previous studies have provided possible mechanisms to interpret this process and they are all examined here to see whether they are important in these modeling experiments: 1) Different from Lu et al. (2008) and Chen et al. (2008), we found no significant increase in eddy phase speed in neither the transient process nor the quasi-equilibrium state. 2) The day-by-day evolution of the rise in tropopause height (averaged in the extratropics) appears to lead the tropospheric jet shift by a few days but there is not a close relation of the time evolution of these two quantities and the dynam-

ical mechanism linking the two is not clear yet. 3) The transient eddy length scale increases but only after the tropospheric jet has shifted, different from the sequence proposed by Kidston et al. (2011). 4) The transient eddies play an important role in maintaining the poleward displacement of the tropospheric jet streams via an acceleration (deceleration) on the poleward (equatorward) flank and the anomalies in eddy propagation and momentum flux are attributed to the changes in the basic state and resulting changes in the index of refraction.

There are a few caveats in this study and more future work is needed to achieve a better and thorough understanding of the dynamics. First, the process of CO_2 doubling is expected to be dependent on the initial conditions. The radiative response strongly depends on the latitudinal distribution of the basic state temperature which controls the initial temperature anomaly following the CO_2 doubling. Hence experiments starting from January 1st and others starting from July 1st are expected to behave differently. This suggests the necessity of another set of modeling experiments with the initial condition of July 1st. Second, although the initial radiative response in the NH wintertime is an equatorward shift of the polar jets with an easterly (westerly) anomaly at high (low) latitudes in the stratosphere, this feature is later strongly modified by the dynamical forcing imposed by the planetary waves. Possibly because of the existence of the low model upper lid and resulting downward wave reflection, more planetary-scale long waves are refracted equatorward, leading to a westerly flow acceleration in the stratosphere. Although this consequence of a low model upper boundary might be universal among other CMIP3/IPCC AR4 coupled climate models, it leads to another question of how the stratospheric and tropospheric circulation responses would be in a model of high stratosphere resolution. Scaife et al. (2011) demonstrated the distinct circulation responses to climate change for standard (CMIP3/IPCC AR4) and vertically extended climate models although the difference in basic state between the two sets

of models probably is not excluded as a cause of differences in the responses. Finally, in our model simulations, the stratospheric circulation responses in the two hemispheres are different. For example, the stratospheric polar jets strengthen in northern winter while that in southern winter shift equatorward associated with an easterly (westerly) anomaly at high (low) latitudes (as shown in Figure 3.3(c)(d) in Chapter 3). This feature is true for both the transient and quasi-equilibrium state in our model simulations. It is possible that the differences in both the radiative and dynamical adjustment for the two hemispheres cause the different circulation anomalies.

Chapter 5

Midlatitude Storm Track Response in A Warmer Climate in CMIP3/IPCC AR4 Coupled Models

5.1 Introduction

Chapter 2 analyzed the midlatitude storm track response to increased greenhouse warming using the GFDL CM2.1 coupled climate model and found that the poleward shift and intensification of the storm tracks is closely related to the enhanced global energy imbalance in the atmosphere. Chapter 3 and 4 further explored the dynamical mechanisms by looking into the transient adjustment of the circulation using the NCAR CAM3 atmospheric model as the CO_2 concentration was instantaneously and uniformly doubled. It is found that the transient eddy momentum flux anomalies drive an anomalous descending motion in the subtropical middle and upper troposphere and thus warms up the atmosphere adiabatically in this

region. In this chapter, we extend the above work to an ensemble of CMIP3/IPCC AR4 coupled models (Meehl et al., 2007a) and demonstrate that the conclusions are universal among other CMIP3/IPCC AR4 models.

5.2 Model Descriptions

Table 5.1 lists the 12 models used in this analysis. These models are chosen based on the availability of daily variables of u, v, T, and q for both the 20C3M runs (1961-2000) and the SRES A1B runs (2081-2100). They are the same models analyzed in Seager et al. (2010d) except for 3 models: the Institute for Numerical Mathematics Climate Model version 3.0 (INMCM3.0) which has no available output for 2081-2100, the NASA Goddard Institute for Space Studies (GISS)-ER which has wrong surface fluxes, and the Model for Interdisciplinary Research on Climate (MIROC3.2) (medres) which has bad specific humidity data. The late 21st century trend is defined as the difference between 2081-2100 and 1961-2000. It is noted here that daily atmosphere data are output to standard levels up to 200mb. In this chapter, we focus on the late 21st century trend in boreal winter.

5.3 Midlatitude Storm Track Response and Its Link with Atmospheric Energy Budget

Figure 5.1 shows the late 21st century trend in 200mb band-pass filtered eddy momentum flux $\overline{u'v'}$ and variance of eddy meridional velocity $\overline{v'v'}$ and 700mb eddy meridional sensible heat flux $\overline{v'T'}$ and moist flux $\overline{v'q'}$. Figure 5.2 shows the zonal average results as a function of latitude and pressure level. The anomalies are shown in color shadings while the 20th century climatologies are shown in contours. These eddy statistics are all averaged in 12 CMIP3/IPCC AR4 coupled models for

Table 5.1: 12 CMIP3/IPCC AR4 coupled models and their resolution for the atmospheric component used in this study.

Model	Atmospheric Resolution
CCCma CGCM3.1 T47	T47L31
CCCma CGCM3.1 T63	T63L31
CNRM-CM3	T63L45
CSIRO Mk3.5	T63L18
GFDL CM2.0	$2.5^o \times 2^o$L24
GFDL CM2.1	$2.5^o \times 2^o$L24
GISS-AOM	$4^o \times 3^o$L12
IAP FGOALS	T42L26
IPSL CM4A	$2.5^o \times 3.75^o$L19
MIUBECHOG	T30L19
MPI ECHAM5	T63L31
MRI CGCM2.3	T42L30

December-January-February (DJF).

The horizontal patterns show a poleward and eastward (downstream) intensification of the midlatitude storm activity accompanied by an intensification on the poleward side of the climatological location while a reduction on its equatorward flank. This is a consistent feature for all the band-pass filtered climate fields and for both hemispheres which is also clearly demonstrated in the vertical patterns (shown in Fig. 5.2). The intensification over the North Atlantic ocean is stronger than that over the North Pacific ocean while it is more zonally symmetric in the SH.

Figure 5.3 shows the response in energy fluxes at the top of the atmosphere (TOA) and at the surface i.e. R_{TOA}, R_{srf}, SH, LH, F_{srf}^{net} and F_{atm}^{net}[1] for DJF. The multi-model averages are shown in color lines while thin grey lines show the results for individual models. As shown, there is a broad increase in TOA radiative flux in

[1]The notations follow Chapter 2. R_{TOA}, R_{srf}, SH, LH, F_{srf}^{net} denote the net radiative flux at the TOA and at the surface, the surface sensible and latent heat flux, and the net energy flux at the surface, respectively.

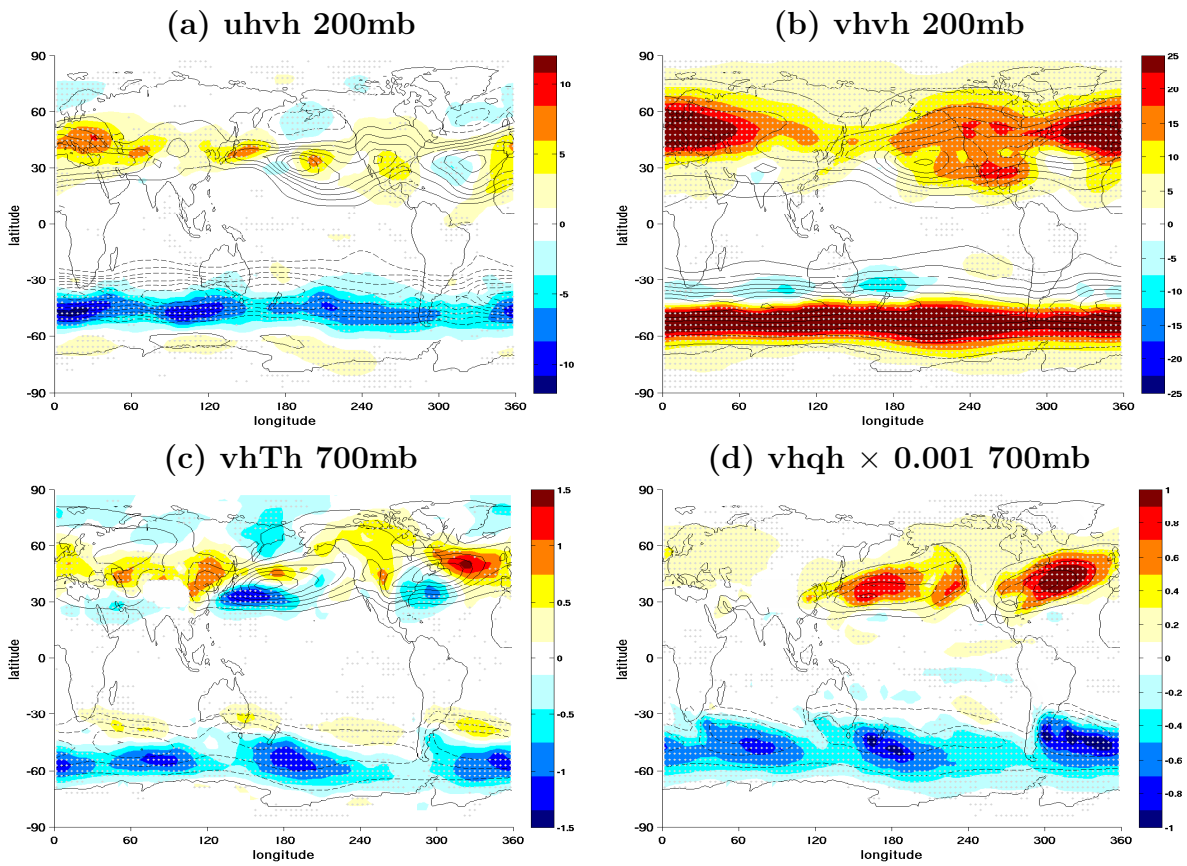

Figure 5.1: The late 21st century trend (A1B scenario) in the midlatitude storm tracks characterized by the band-pass filtered (a) eddy momentum flux and (b) variance of eddy meridional velocity at 200mb, and meridional sensible (c) and moisture transport (d) at 700mb. The trends (climatologies) are shown in color shadings (contours). The results are averaged in 12 CMIP3/IPCC AR4 coupled climate models for December-January-February (DJF). Grey dots indicate at least 10 out of the 12 models agree in the sign of the storm track changes.

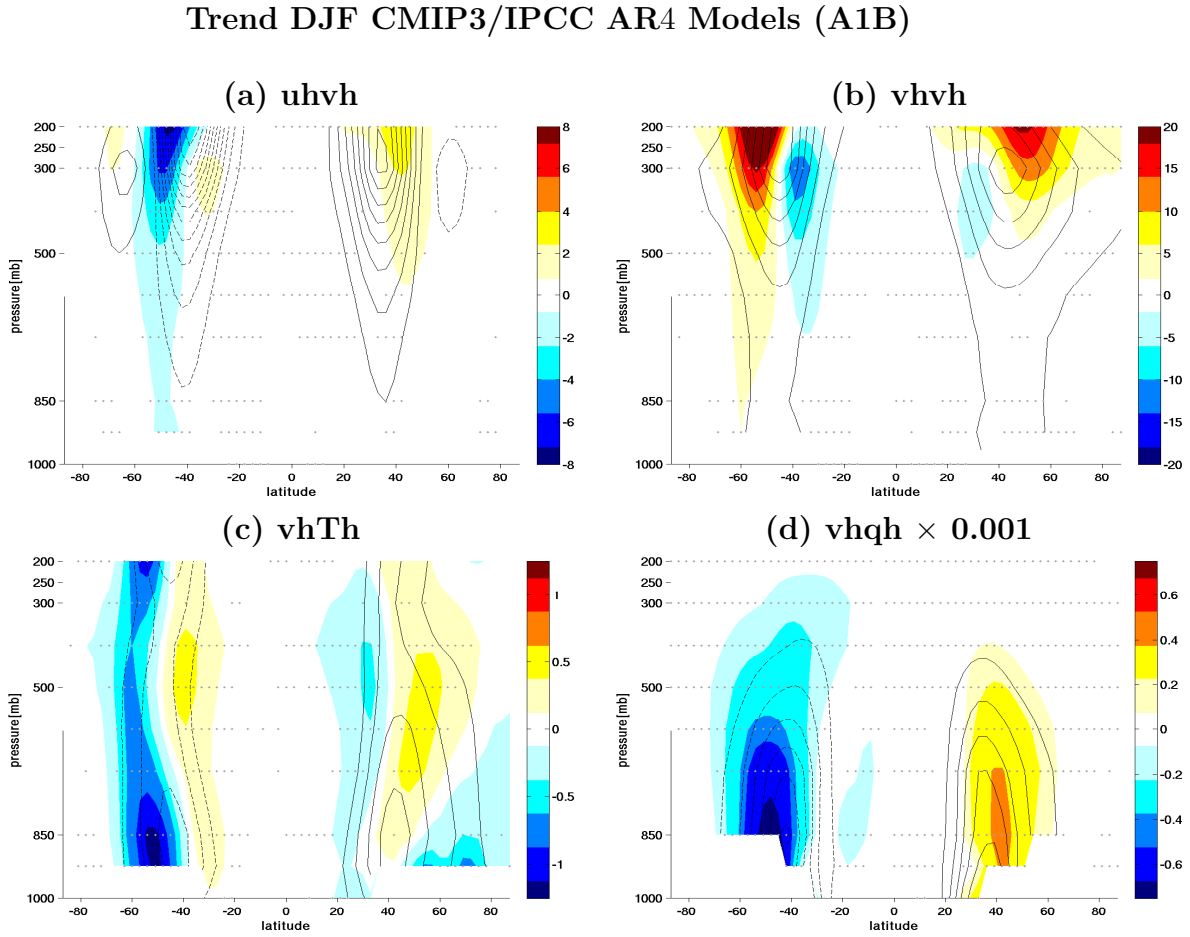

Figure 5.2: The same as Figure 5.1 but for the zonal averages as a function of latitude and pressure level.

the tropics and subtropics between about 40^{o}S and 40^{o}N. This is associated with a reduction in outgoing longwave radiation (OLR) in the deep convective region and a reduction in low cloud cover and increased incoming solar radiation elsewhere in the low latitudes (Trenberth et al., 2009). However, as a result of high latitude surface warming and increased terrestrial radiation, the radiative flux at the TOA decreases in the NH middle and high latitudes. In the SH, R_{TOA} decreases (increases) in the middle (high) latitudes which is related to the change in low cloud cover (not shown). The change in net surface flux is relatively small with surface radiative and non-radiative fluxes largely offsetting each other except in the NH middle and high latitudes and in the SH high latitudes (shown in Fig. 5.3(e)). In particular, consistent with what has been found in the GFDL CM2.1 model simulations in Chapter 2, the evaporation generally enhances everywhere as a result of increased greenhouse effect and the surface sensible flux reduces in the NH due to reduced land-sea contrast except in the NH polar region where the heat flux increases due to sea ice melting. In the Southern Ocean, both the sensible and latent heat fluxes decrease as a result of increased ocean heat uptake. Therefore, the change in net energy flux in the atmosphere F_{atm}^{net} is similar to that in R_{TOA} and shows a net gain in the tropics and subtropics while a net loss at middle and high latitudes (shown in Fig. 5.3(f)). This feature is robust among different CMIP3/IPCC AR4 coupled climate models. The enhanced energy imbalance in the atmosphere requires the atmosphere to transport more energy from low to high latitudes, a large portion of which is accomplished by the intensified midlatitude storm tracks.

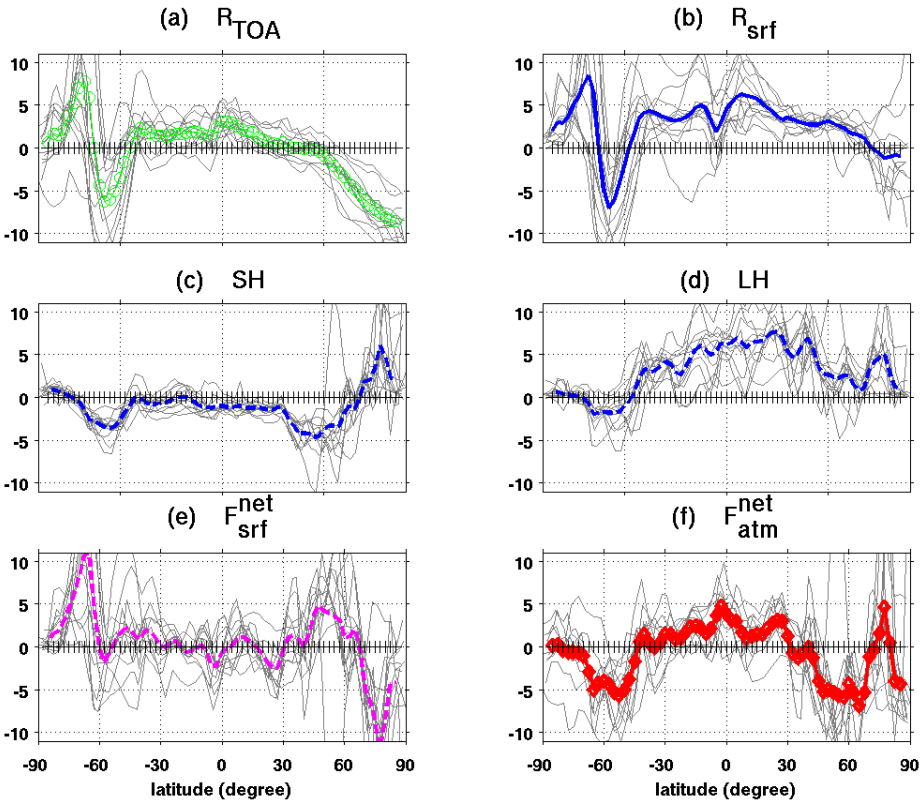

Figure 5.3: The late 21st century trend in (a) R_{TOA}, (b) R_{srf}, (c) SH, (d) LH, (e) F_{srf}^{net} and (f) F_{atm}^{net} for December-January-February (DJF). The color lines show the multi-model averages while the thin grey lines show the results from individual models. The units are W/m^2.

5.4 Eddy-Driven Vertical Motion in CMIP3/IPCC AR4 Coupled Models

Figure 5.4 shows the boreal winter multi-model average of $\langle \bar{T} \rangle$, $\langle \bar{u} \rangle$, $\langle \overline{u'v'} \rangle$, $\langle \overline{u_H v_H} \rangle$ [2], $\langle \bar{\omega}_{eddy} \rangle$ and $\langle \bar{\omega} \rangle$ for the 1961-2000 climatology (shown in black contours) and the late 21st century trend (shown in colors) in the troposphere from 200mb to 1000mb. Because the CMIP3/IPCC AR4 experiments are quasi-equilibrium runs and the diabatic heating term is not available in the standard output, we can't examine the causality sequence or close the zonal mean temperature equation as in Chapter 3. Instead we calculate the eddy-driven vertical motion ω_{eddy} using the transient eddy momentum flux $\langle \overline{u'v'} \rangle$ from the model output and compare it to the total vertical motion ω. As expected, there is a broad temperature increase in the whole troposphere. For example, the 4K temperature increase extends to about 40^oS and 50^oN. Both the tropospheric jets and (high-frequency) transient eddy momentum flux shift poleward with an intensification on the poleward flank. There is also an anomalous downward motion in the subtropics between about 30^oN and 40^oN and between 40^oS and 50^oS, generally at the poleward edge of the upper tropospheric warming. The agreement between ω_{eddy} and ω in both the location and amplitude supports the idea that the descending motion anomaly is driven by the enhanced transient eddy momentum flux convergence, primarily via the high-frequency component. This is a robust feature for each of these 12 models except for the IAP FGOALS. Therefore, the linkage between the eddy-driven vertical motion anomaly and the subtropical warming expansion in the middle and upper troposphere is consistent with the CAM3-SOM results although the cause and effect can't be assessed for the CMIP3/IPCC AR4 models.

[2] $\langle \overline{u'v'} \rangle$ denotes the transient eddy momentum flux without band-pass filtered while $\langle \overline{u_H v_H} \rangle$ denotes the band-pass filtered component.

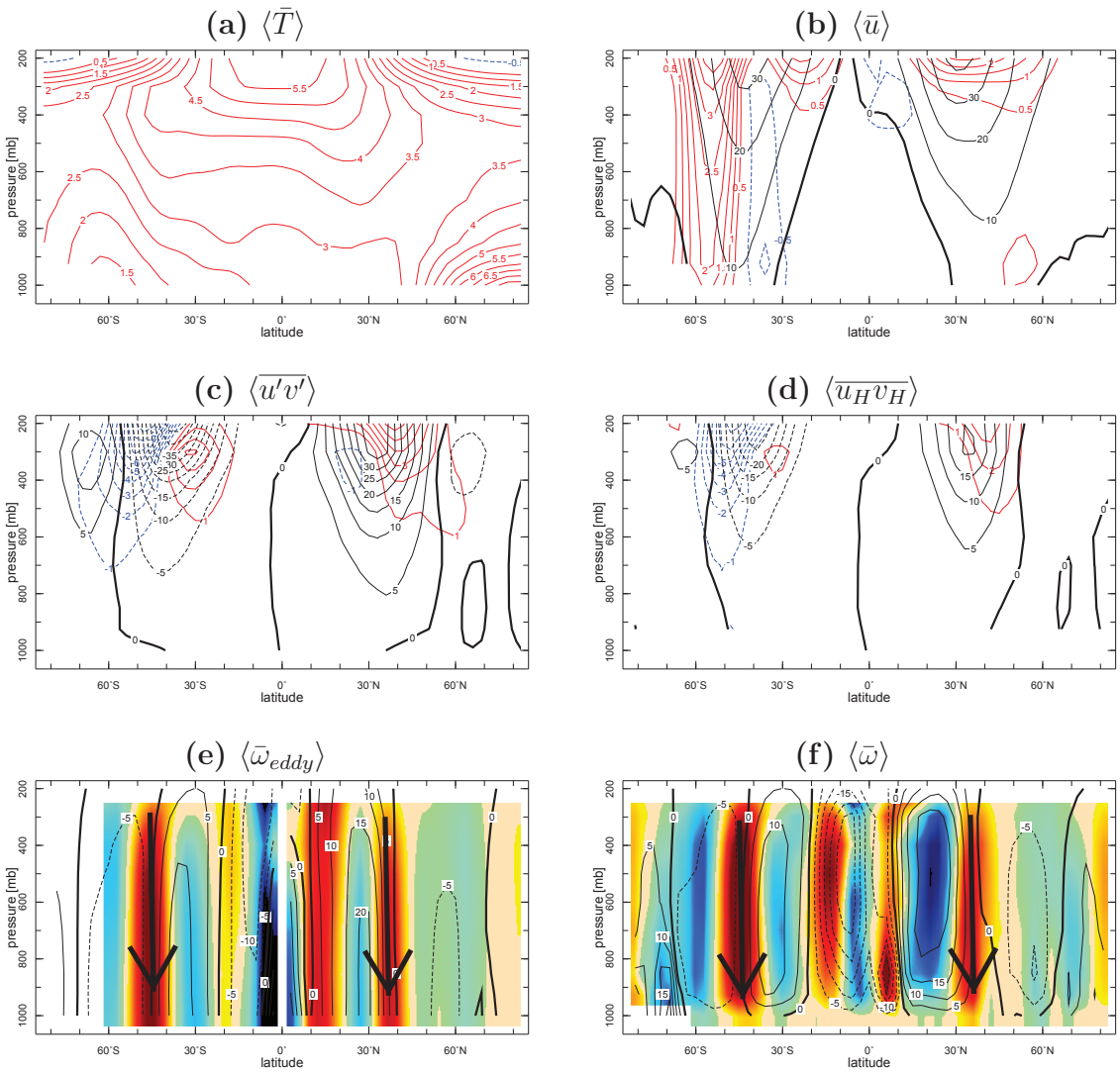

Figure 5.4: The late 21st century trend in (a) $\langle \bar{T} \rangle$ [K], (b) $\langle \bar{u} \rangle$ [m/s], (c) transient eddy momentum flux $\langle \overline{u'v'} \rangle$ [m^2/s^2], (d) band-pass filtered transient eddy momentum flux denoted by $\langle \overline{u_H v_H} \rangle$ [m^2/s^2], (e) eddy-driven vertical motion $\langle \bar{\omega}_{eddy} \rangle$ [mb/day] and (f) model output $\langle \bar{\omega} \rangle$ [mb/day] averaged in 12 CMIP3/IPCC AR4 coupled models for December-January-February (DJF). The color contours (shadings) show the late 21st century trend while the black contours show the average of 1961-2000. The color scale in (e)(f) is the same as in Figure 3.10 in Chapter 3. It is noted that the pressure level is up to 200mb due to availability of daily variables.

5.5 Conclusions and Discussions

This chapter is a follow-up study from the previous chapters and extends the analyses to an ensemble of CMIP3/IPCC AR4 coupled models. Consistent with the results in Chapter 2, the future projections in midlatitude storm tracks show a poleward and upward shift and an intensification on the poleward side of the maximum climatological position in multi-model averages. The enhanced atmospheric energy imbalance is also true for other climate models and is in good agreement with the intensified storm tracks and associated poleward energy transport in the midlatitudes. As a consequence of increased transient eddy momentum flux convergence, largely from its high frequency component, the eddies tend to drive an anomalous mean meridional circulation in the troposphere and the resulting descending motion anomaly acts to warm up the subtropical troposphere adiabatically. The agreement between the calculated eddy-driven vertical motion anomaly and the actual vertical motion anomaly supports the idea that the extensive warming anomaly in the subtropical troposphere is driven as a consequence of circulation change rather than vice versa. This is also consistent among different CMIP3/IPCC AR4 coupled models.

Chapter 6

Conclusions and Future Directions

In this thesis, we study the future projections of the midlatitude storm tracks and the associated dynamical mechanisms by using comprehensive climate models.

We start from analyzing the anthropogenic climate change simulation (A1B scenario) from the GFDL CM2.1 coupled model, one of the models that have been widely used to study a variety of phenomena both in the atmosphere and the ocean. A broad range of band-pass filtered climate fields have been diagnosed to identify the changes in the midlatitude storm tracks such as the transient eddy momentum flux, the meridional component of the eddy kinetic energy, the poleward transport of sensible and latent heat flux for both the boreal summer and winter. It is found that the storm tracks are projected to shift poleward and upward and to intensify on the poleward flank of the climatology, consistently across all the climate variables characterizing the midlatitude storm tracks. The maximum dry Eady growth rate is examined to determine the effect of global warming on the time mean state and associated available potential energy for transient eddy growth. The trend in maximum Eady growth rate, mainly determined by the extensive tropical and subtropical upper tropospheric warming, is generally consistent with the poleward shift and intensification of the storm tracks in the middle latitudes of both hemispheres

in both seasons. However, in the lower troposphere in northern winter, increased meridional eddy transfer within the storm tracks is more associated with increased eddy velocity, stronger correlation between eddy velocity and eddy moist static energy, and longer eddy length scales. The changing characteristics of baroclinic instability are, therefore, closely related to the storm track response as climate warms. Diagnosis of the latitude-by-latitude energy budget for the current and future climate demonstrates how the coupling between radiative and surface heat fluxes and eddy heat and moisture transports influence the midlatitude storm track response to global warming. Partly by radiative forcing by increased atmospheric CO_2 and water vapor, more energy is gained within the tropics and subtropics, while in the middle and high latitudes energy is reduced through increased outgoing terrestrial radiation in the Northern Hemisphere and increased ocean heat uptake in the Southern Hemisphere. This enhanced energy imbalance in the future climate requires larger atmospheric energy transport in the midlatitudes which are partially accomplished by intensified storm tracks. This is covered in Chapter 2.

The work in Chapter 2 focuses on the equilibrium simulation of the future climate where the CO_2 concentration is gradually increased and doubles at the end of the 21st century; however, how and why the future climate state is reached as a consequence of CO_2 increase is not clear. As also noticed in Chapter 2 and other studies (e.g., Yin, 2005; O'Gorman, 2010; Butler et al., 2010), the enhanced tropical and subtropical upper tropospheric warming is closely connected to the poleward displacement of the tropospheric jet streams and the transient eddies as expected from the theory of linear baroclinic instability. However, whether the temperature response acts as the forcing of the circulation change or takes place because of the circulation change is not known. Therefore, one of the major questions investigated next is what causes the broad warming in the subtropical upper and middle troposphere. In order to identify the chain of causality sequence that occurs in

the circulation response to global warming, Chapter 3 and Chapter 4 study the transient circulation adjustment in the atmosphere when the CO_2 concentration is instantaneously and uniformly doubled. We use the NCAR CAM3 coupled to a slab ocean model where the sea surface temperatures (SSTs) are allowed to adjust to energy imbalance. It is found that the thermal structure and circulation response is well established after one year of integration with the magnitudes gradually increasing afterwards towards quasi-equilibrium. Chapter 3 mainly emphasizes the transient temperature response in the middle and upper troposphere and the zonal mean temperature equation with the adiabatic and diabatic contributions being investigated. It is found that the subtropical warming in the middle and upper troposphere takes place after two months' integration and is driven adiabatically by the dynamical contributions rather than diabatically due to latent heat release which was commonly assumed in previous studies (e.g., Hansen et al., 1984; Butler et al., 2010; Rivire, 2011). It is the intensification of the transient eddy momentum flux convergence that causes anomalous descending motion and adiabatic warming in the subtropics. Therefore, the warming in the subtropical middle and upper troposphere is a consequence of the circulation change rather than a cause.

It is also noticed in the day-by-day evolution of the zonal mean zonal wind anomaly that the poleward displacement of the midlatitude tropospheric jet streams occurs after the intensification of the subpolar westerlies in the stratosphere as well as the intensification of transient eddy momentum flux convergence in the upper troposphere with all occurring in the first few months of integration. This suggests the importance of the stratosphere, the stratosphere-troposphere coupling and the tropospheric transient eddies in determining the extratropical tropospheric circulation response to global warming. In order to further explore the dynamical mechanisms, Chapter 4 defines three stages during the transient circulation adjustment process in the Northern Hemisphere. Phase 1 contains a small equatorward shift

of the polar jets in the stratosphere associated with an easterly (westerly) anomaly at high (low) latitudes. This process is primarily radiatively driven caused by the effect the CO_2 increase has on basic state temperature variations as a function of latitude. This circulation anomaly is then altered by the planetary-scale eddies in Phase 2 and a westerly acceleration in the stratosphere occurs. This westerly acceleration is driven by the increased meridional divergence of the momentum flux from planetary waves (possibly as a result of the low model upper boundary and downward wave reflection). In Phase 3 the extratropical circulation response gets established and the tropospheric jet streams are shifted poleward. Different from Lu et al. (2008) and Chen et al. (2008), we found no significant increase in eddy phase speed in this process, and what's more, the increase in eddy length scale takes place after the jet shift, which is different from the mechanism suggested by Kidston et al. (2011).

Chapter 5 extends the above diagnoses to other CMIP3/IPCC AR4 coupled models and the results shown in the previous chapters are consistent among other models. The storm tracks consistently shift poleward and intensify on the poleward side of the maximum climatological location. There is also a robust enhancement of the global atmospheric energy imbalance which requires the atmosphere to transport more energy from the Equator to the poles, and in the midlatitudes, the storm tracks accomplish a large amount of the energy transfer. The enhanced transient eddy momentum flux convergence also tends to drive an anomalous descending motion in the subtropical troposphere which agrees well with the actual downward motion anomaly in this region. It supports the idea that the extensive upper and middle upper tropospheric warming is driven by the eddies.

The major conclusions in this thesis are summarized in the following:

- We have confirmed the poleward and upward shift and intensification of the midlatitude storm tracks as a consequence of increased CO_2 emission in the

CMIP3/IPCC AR4 coupled climate models based on a wide range of band-pass filtered climate fields characterizing the storm tracks. The changes in the location and intensity of the storm tracks are generally consistent with the changes in the baroclinic instability. In the lower troposphere in northern winter, the increased meridional energy transfer within the storm tracks is more associated with increased eddy velocity, stronger correlation between eddy velocity and eddy moist static energy, and longer eddy length scale despite reduced latitudinal temperature gradients at low levels. Furthermore, a close linkage between the changes in the storm tracks and the changes in global atmospheric energy budget is identified. It is found that in the future climate more energy is gained within the tropical and subtropical atmosphere while more is lost from middle and high latitude atmosphere. This increased energy imbalance in the global atmosphere requires larger atmospheric energy transports in the midlatitudes which are partially accomplished by the intensified storm tracks.

- We have investigated the dynamical mechanisms underlying the extratropical tropospheric circulation responses as simulated in the CMIP3/IPCC AR4 models by looking into the transient circulation adjustment. This allows an assessment of the transient, sequential, response day by day and week by week before the structure of the extratropical tropospheric circulation response is established. The transient circulation adjustment is examined using the NCAR CAM3 atmospheric model (one of the CMIP3/IPCC AR4 models but with T42 horizontal resolution) coupled to a slab ocean model subject to a uniform and instantaneous doubling of CO_2 concentration in the atmosphere on January 1st. The thermal structure and circulation response is well established after one year of integration with the magnitudes gradually increasing afterwards towards quasi-equilibrium. Tropical upper tropospheric

warming occurs in the first month. The expansion of the warming in the middle and upper troposphere to the subtropics occurs later and is found to be primarily dynamically-driven due to the intensification of transient eddy momentum flux convergence and resulting anomalous descending motion in this region. This indicates that the extensive warming in the subtropical middle and upper troposphere is a consequence of the extratropical circulation change rather than a cause.

- We have further examined the dynamics associated with the transient circulation adjustment prior to the establishment of the extratropical tropospheric circulation response. The transient adjustment process also allows an unified and comparable assessment of all the possible proposed mechanisms within the same framework to see whether they play an important role or not. From the day-by-day evolution of the zonal mean zonal wind in the Northern Hemisphere extratropics, we have identified three stages during the adjustment process. The initial response takes place in the stratosphere and has an easterly anomaly at high latitudes together with a westerly anomaly at low latitudes which is driven radiatively due to the impact of the CO_2 increase on the stratospheric temperature distribution. A strong westerly acceleration is then seen in Phase 2 and is driven as a result of enhanced planetary wave momentum flux convergence. Following the westerly acceleration in the stratosphere, a poleward displacement of the midlatitude tropospheric jet streams occurs in Phase 3 together with the change in transient eddy momentum flux convergence. In the final stage of the transient adjustment, we have identified the importance of the transient eddies in setting up the poleward displacement of the tropospheric jet streams and linear refractive theory is quite successful in interpreting the transient eddy propagation anomaly in this process. In addition, we have found no significant increase in eddy phase

speed during the adjustment process and the increase in eddy length scale appears to occur after the jet shift, not before.

This work has emphasized the complex dynamics of the general circulation of the atmosphere and found that more future work is needed to achieve a better and thorough understanding of the dynamics. Some of the future directions following this thesis are listed below:

- The simulation results from the instantaneous doubling CO_2 experiments could be dependent on the initial conditions such as the timing of the increase of CO_2 concentration. In Chapter 3 and Chapter 4, the CO_2 concentration is suddenly doubled on January 1st and because of the different stratospheric basic states in the Northern and Southern Hemisphere, the initial radiative responses are different for the two hemispheres. Therefore it is worth repeating the model experiments but with July 1st as initial conditions. This set of experiments is currently being performed at the Lamont-Doherty Earth Observatory and the results will be analysed once they are finished.

- The results presented in Chapter 4 have indicated the possible effect of the low model upper boundary in affecting the circulation adjustment in the stratosphere. Therefore it is worth checking how the stratospheric circulation will respond to climate change with a high stratosphere resolution model. Similar work has been done in Scaife et al. (2011) but the role of a changing basic state might not be excluded in their study. So we would like to set up two parallel climate change experiments with a model of low top and high top while keeping other model configurations the same. The comparison between these two experiments will reveal the impact of the model upper boundary.

- A set of instantaneous ozone depletion experiments are being performed at Lamont-Doherty Earth Observatory using the CAM3 coupled to a slab ocean

model. Previous studies have found that the ozone depletion in the stratosphere could shift the tropospheric jet streams poleward and in fact, the stratospheric ozone depletion in the 20th century is the dominant driver of the atmospheric circulation change in the Southern Hemisphere (e.g., Kushner and Polvani, 2004; Polvani et al., 2011). The ozone field in our experiments is suddenly switched from the 1960 reference level to the estimated 'world avoided' level during years 2020-2030 if the chlorofluorocarbons (CFCs) had not been regulated (Newman et al., 2009). One purpose of this study is to investigate the transient circulation adjustment to instantaneous ozone depletion for comparison with the case of instantaneous CO_2 doubling. The depletion of ozone is expected to modify the stratospheric temperature distribution and later influence the tropospheric circulation via 'downward control'. Another purpose is to explore the hydrological cycle response as a consequence of severe ozone depletion. Kang et al. (2011) demonstrated that the observed drying trend in Australia in summer is dominantly caused by the ozone depletion in the latter half of the 20th century. With a stronger ozone depletion in the case of 'world avoided', we expect to see a stronger impact on the hydrological cycle in the tropics and even in the Northern Hemisphere. In addition, as mentioned in Newman et al. (2009), the 'world avoided' severe ozone depletion would lead to significant circulation changes in the stratosphere, for example, the climatological easterlies in southern summer would switch to westerlies and 'a permanent winter across the seasons by 2065' in the stratosphere would occur (Newman et al., 2009). We plan to look into these interesting phenomena and investigate the associated dynamical mechanisms as well.

Bibliography

Andrews, D. G., J. R. Holton, and C. B. Leovy, 1987: *Middle Atmosphere Dynamics*. Academic Press, 480pp pp.

Baldwin, M. P. and T. J. Dunkerton, 2001: Stratospheric harbingers of anomalous weather regimes. *Sci.*, **294 (5542)**, 581–584.

Bengtsson, L., K. I. Hodges, and N. Keenlyside, 2009: Will extratropical storms intensify in a warmer climate? *J. Climate*, **22**, 2276–2301.

Bengtsson, L., K. I. Hodges, and E. Roeckner, 2006: Storm tracks and climate change. *J. Climate*, **19**, 3518–3543.

Blackmon, M. L., 1976: A climatological spectral study of the 500mb geopotential height of the Northern Hemisphere. *J. Atmos. Sci.*, **33**, 1607–1623.

Bordoni, S. and T. Schneider, 2008: Monsoons as eddy-mediated regime transitions of the tropical overturning circulation. *Nature Geoscience*, **1**, 515–519.

Bordoni, S. and T. Schneider, 2010: Regime transitions of steady and time-dependent hadley circulations: Comparison of axisymmetric and eddy-permitting simulations. *J. Atmos. Sci.*, **67**, 1643–1654.

Boville, B. A., 1984: The influence of the polar night jet on the tropospheric circulation in a GCM. *J. Atmos. Sci.*, **41**, 1132–1142.

Boville, B. A. and C. S. Bretherton, 2003: Heating and kinetic energy dissipation in the NCAR Community Atmosphere Model. *J. Clim.*, **16**, 3877–3887.

Boville, B. A. and X. Cheng, 1988: Upper boundary effects in a general circulation model. *J. Atmos. Sci.*, **45**, 2592–2606.

Broccoli, A. J. and S. Manabe, 1992: The effects of orography on midlatitude Northern Hemisphere dry climates. *J. Climate*, **5**, 1181–1201.

Butchart, N., S. A. Clough, T. N. Palmer, and P. J. Trevelyan, 1982: Simulations of an observed stratospheric warming with quasigeostrophic refractive index as a model diagnostic. *Quart. J. Roy. Meteor. Soc.*, DOI: 10.1002/qj.49710845702.

Butler, A. H., D. W. J. Thompson, and R. Heikes, 2010: The steady-state atmospheric circulation response to climate change-like thermal forcings in a simple general circulation model. *J. Clim.*, **23**, 3474–3496.

Carissimo, B. C., A. H. Oort, and T. H. V. Haar, 1985: Estimating the meridional energy transports in the atmosphere and ocean. *J. Phys. Oceanogr.*, **15**, 82–91.

Chang, E. K., 1993: Downstream development of baroclinic waves as inferred from regression analysis. *J. Atmos. Sci.*, **50**, 2038–2053.

Chang, E. K. M., 2009: Diabatic and orographic forcing of northern winter stationary waves and storm tracks. *J. Climate*, **22**, 670–688.

Chang, E. K. M., S. Lee, and K. L. Swanson, 2002: Storm track dynamics. *J. Climate*, **15**, 2163–2183.

Chang, E. K. M. and I. Orlanski, 1993: On the dynamics of a storm track. *J. Atmos. Sci.*, **50**, 999–1015.

Charney, J. G., 1947: The dynamics of long waves in a baroclinic westerly current. *J. Meteor.*, **4**, 135–162.

Charney, J. G. and P. G. Drazin, 1961: Propagation of planetary-scale disturbances from the lower into the upper atmosphere. *J. Geophys. Res.*, **66(1)**, 83–109, doi:10.1029/JZ066i001p00 083.

Chen, G. and I. M. Held, 2007: Phase speed spectra and the recent poleward shift of Southern Hemisphere surface westerlies. *Geophys. Res. Lett.*, **34**, L21 805, doi:10.1029/2007GL031 200.

Chen, G., J. Lu, and D. M. Frierson, 2008: Phase speed spectra and the latitude of surface westerlies: Interannual variability and Global warming trend. *J. Climate*, **21**, 5942–5959.

Chen, P. and W. Robinson, 1992: Propagation of planetary waves between the troposphere and stratosphere. *J. Atmos. Sci.*, **49**, 2533–2545.

Collins, W. D., et al., 2004: Description of the NCAR Community Atmosphere Model (CAM3.0). Tech. rep., Climate And Global Dynamics Division, National Center For Atmospheric Research, Boulder, Colorado, USA.

Collins, W. D., et al., 2006: The formulation and atmospheric simulation of the Community Atmosphere Model version 3 (CAM3). *J. Clim.*, **19**, 2144–2161.

Delworth, T. L., et al., 2006: GFDL's CM2 Global Coupled Climate Models. Part I: Formulation and Simulation Characteristics. *J. Climate*, **19**, 643–674.

Dunkerton, T., 1978: On the mean meridional mass motions of the stratosphere and mesosphere. *J. Atmos. Sci.*, **35(12)**, 2325–2333.

Eady, E. T., 1949: Long waves and cyclone waves. *Tellus*, **1**, 33–52.

Edmon, H. J., B. J. Hoskins, and M. E. McIntyre, 1980: Eliassen-palm cross sections for the troposphere. *J. Atmos. Sci.*, **37**, 2600–2616.

Emanuel, K. A., M. Fantini, and A. J. Thorpe, 1987: Baroclinic Instability in an Environment of Small Stability to Slantwise Moist Convection. Part I: Two-Dimensional Models. *J. Atmos. Sci.*, **44**, 1559–1573.

Frierson, D. M. W., I. M. Held, and P. Zurita-Gotor, 2006: A Gray-Radiation Aquaplanet Moist GCM. Part I: Static Stability and Eddy Scale. *J. Atmos. Sci.*, **63**, 2548–2566.

Frierson, D. M. W., I. M. Held, and P. Zurita-Gotor, 2007: A Gray-Radiation Aquaplanet Moist GCM. Part II: Energy Transports in Altered Climates. *J. Atmos. Sci.*, **64**, 1680–1693.

Fyfe, J. C., 2003: Extratropical Southern Hemisphere cyclones: Harbingers of climate change. *J. Climate*, **16**, 2802–2805.

Gastineau, G. and B. J. Soden, 2009: Model projected changes of extreme wind events in response to global warming. *Geophys. Res. Lett.*, **36**, L10 810, doi:10.1029/2009GL037 500.

Geng, Q. and M. Sugi, 2003: Possible change of extratropical cyclone activity due to enhanced greenhouse gases and sulfate aerosols - Study with a high-resolution AGCM. *J. Climate*, **16**, 2262–2274.

Green, J. S. A., 1970: Transfer properties of the large-scale eddies and the general circulation of the atmosphere. *Quart. J. Roy. Meteor. Soc.*, **96**, 157–185.

Gregory, J. and M. Webb, 2008: Tropospheric adjustment induces a cloud component in CO_2 forcing. *J. Clim.*, **21**, 58–71.

Gregory, J. M., J. F. B. Mitchell, and A. J. Brady, 1996: Summer Drought in Northern Midlatitudes in a Time-Dependent CO_2 Climate Experiment. *J. Climate*, **10**, 662–686.

Gregory, J. M., et al., 2004: A new method for diagnosing radiative forcing and climate sensitivity. *Geophys. Res. Lett.*, **31**, L03 205, doi:10.1029/2003GL018 747.

Hall, N. M. J., B. J. Hoskins, P. J. Valdes, and C. A. Senior, 1994: Storm tracks in a high-resolution GCM with doubled carbon dioxide. *Quart. J. Roy. Meteor. Soc.*, **120**, 1209–1230.

Hansen, J. E., A. Lacis, D. Rind, G. Russell, P. Stone, I. Fung, R. Ruedy, and J. Lerner, 1984: Climate sensitivity: Analysis of feedback mechanisms. In *Climate Processes and Climate Sensitivity*, AGU Geophysical Monograph 29, Maurice Ewing Vol. 5. J. E. Hansen and T. Takahashi, Eds. American Geophysical Union, 130-163 pp.

Harnik, N. and R. S. Lindzen, 1997: The effect of basic-state potential vorticity gradients on the growth of baroclinic waves and the height of the tropopause. *J. Atmos. Sci.*, **55**, 344–360.

Harnik, N. and R. S. Lindzen, 2001: The effect of reflecting surfaces on the vertical structure and variability of stratospheric planetary waves. *J. Atmos. Sci.*, **58**, 2872–2894.

Harnik, N., R. Seager, N. Naik, M. Cane, and M. Ting, 2010: The role of linear wave refraction in the transient eddy-mean flow response to tropical Pacific SST anomalies. *Quart. J. Roy. Meteor. Soc.*, 136: 2132C2146. doi: 10.1002/qj.688.

Hartley, D. E., J. T. Villarin, R. X. Black, and C. A. Davis, 1998: A new perspective on the dynamical link between the stratosphere and troposphere. *Nature*, **391**, 471–474.

Haynes, P. H., M. E. McIntyre, T. G. Shepherd, C. J. Marks, and K. P. Shine, 1991: On the downward control of extratropical diabatic circulations by eddy-induced mean zonal forces. *J. Atmos. Sci.*, **48**, 651–678.

Hazeleger, W., 2005: Can global warming affect tropical ocean heat transport? *Geophys. Res. Lett.*, 32, L22 701, doi:10.1029/2005GL023 450.

Held, I. M., 1993: Large-scale dynamics and global warming. *Bull. Amer. Meteor. Soc.*, **74**, 228–241.

Held, I. M. and E. O'Brien, 1992: Quasigeostrophic turbulence in a three-layer model: effects of vertical structure in the mean shear. *J. Atmos. Sci.*, **49**, 1861–1870.

Held, I. M. and B. J. Soden, 2006: Robust Response of the Hydrological Cycle to Global Warming. *J. Climate*, **19**, 5686–5699.

Hoskins, B. J. and K. I. Hodges, 2002: New perspectives on the northern hemisphere winter storm tracks. *J. Atmos. Sci.*, **59**, 1041–1061.

Hoskins, B. J. and P. J. Valdes, 1990: On the Existence of Storm-Tracks. *J. Atmos. Sci.*, **47**, 1854–1864.

Hu, Y. and Q. Fu, 2007: Observed poleward expansion of the Hadley circulation since 1979. *Atmos. Chem. Phys.*, **7**, 5229–5236.

Hurrell, J. W., J. J. Hack, A. S. Phillips, J. Caron, and J. Yin, 2006: The dynamical simulation of the Community Atmosphere Model version 3 (CAM3). *J. Clim.*, **19**, 2162C2183.

Ineson, S. and A. A. Scaife, 2009: The role of the stratosphere in the european climate response to El Nino. *Nature Geoscience*, **2**, 32–36.

Kalnay, E. and Coauthors, 1996: The NCEP/NCAR 40-Year Reanalysis Project. *Bull. Amer. Meteor. Soc.*, **77**, 437–471.

Kang, S., L. Polvani, J. C. Fyfe, and M. Sigmond, 2011: Impact of polar ozone depletion on subtropical precipitation. *Sci.*, **332**, 951–954.

Karoly, D. J. and B. J. Hoskins, 1982: Three-dimensional propagation of planetary waves. *J. Meteor. Soc. Japan*, **60**, 109–123.

Kidston, J., S. M. Dean, J. A. Renwick, and G. K. Vallis, 2010: A robust increase in eddy length scale in the simulation of future climates. *Geophys. Res. Lett.*, 37, L03 806, doi:10.1029/2009GL041 615.

Kidston, J., G. K. Vallis, S. M. Dean, and J. A. Renwick, 2011: Can the increase in the eddy length scale under global warming cause the poleward shift of the jet streams? *J. Clim.*, In press.

Klein, W. H., 1957: Principal tracks and mean frequencies of cyclones and anticyclones in the Northern Hemisphere. Tech. rep., Research Paper 40, U. S. Weather Bureau, 60pp pp.

Kunz, T., 2008: The role of breaking synoptic scale Rossby waves for the North Atlantic oscillation and its coupling with the stratosphere. Ph.D. thesis, der Universitat Hamburg.

Kushner, P. and L. Polvani, 2004: Stratosphere-troposphere coupling in a relatively simple AGCM: The role of eddies. *J. Clim.*, **17**, 629–639.

Kushner, P. J., I. M. Held, and T. L. Delworth, 2001: Southern Hemisphere atmospheric circulation response to global warming. *J. Clim.*, **14**, 2238–2249.

Lambert, S. J., 1995: The effect of Enhanced Greenhouse Warming on Winter Cyclone Frequencies and Strengths. *J. Climate*, **8**, 1447–1452.

Lambert, S. J. and J. C. Fyfe, 2006: Changes in winter cyclones frequencies and strengths simulated in enhanced greenhouse warming experiments: results from the models participating in the IPCC diagnostic exercise. *Clim. Dyn.*, **26**, 713–728.

Lapeyre, G. and I. M. Held, 2004: The role of moisture in the dynamics and energetics of turbulent baroclinic eddies. *J. Atmos. Sci.*, **61**, 1693–1710.

Lee, W.-J. and M. Mak, 1996: The role of orography in the dynamics of storm tracks. *J. Atmos. Sci.*, **53**, 1737–1750.

Levitus, S., J. I. Antonov, J. Wang, T. L. Delworth, K. W. Dixon, and A. J. Broccoli, 2001: Anthropogenic Warming of Earth's Climate System. *Sci.*, **292**, 267–270.

Lin, S. J., 2004: A Vertically Lagrangian Finite-Volume Dynamical Core for Global Models. *Mon. Wea. Rev.*, **132**, 2293–2307.

Lindzen, R. S. and B. F. Farrell, 1980: A simple approximation result for maximum growth rate of baroclinic instabilities. *J. Atmos. Sci.*, **37**, 1648–1654.

Lorenz, D. J. and E. T. DeWeaver, 2007: Tropopause height and zonal wind response to global warming in the IPCC scenario integrations. *J. Geophys. Res.*, **112**, D10 119, doi:10.1029/2006JD008 087.

Lorenz, D. J. and D. L. Hartmann, 2001: Eddyczonal flow feedback in the southern hemisphere. *J. Atmos. Sci.*, **58**, 3312–3327.

Lorenz, E. N., 1955: Available potential energy and the maintenance of the general circulation. *Tellus*, **7**, 157–167.

Lu, J., G. Chen, and D. M. W. Frierson, 2008: Response of the zonal mean atmospheric circulation to El Nino versus global warming. *J. Clim.*, **21**, 5835–5851.

Lu, J., C. Deser, and T. Reichler, 2009: Cause of the widening of the tropical belt since 1958. *Geophys. Res. Lett.*, **36**, L03 803, doi:10.1029/2008GL036 076.

Lu, J., G. A. Vecchi, and T. Reichler, 2007: Expansion of the Hadley cell under global warming. *Geophys. Res. Lett.*, **34**, L06 805, doi:10.1029/2006GL028 443.

Lunkeit, F., K. Fraedrich, and S. E. Bauer, 1998: Storm tracks in a warmer climate: sensitivity studies with a simplified global circulation model. *Clim. Dyn.*, **14**, 813–826.

Manabe, S., K. Bryan, and M. J. Spelman, 1990: Transient response to a global ocean-atmosphere model to a doubling of atmosphere carbon dioxide. *J. Phys. Oceanogr.*, **20**, 722–749.

Matsuno, T., 1970: Vertical propagation of stationary planetary waves in the winter Northern Hemisphere. *J. Atmos. Sci.*, **27**, 871–883.

McCaa, J. R., M. Rothstein, B. E. Eaton, J. M. Rosinski, E. Kluzek, and M. Vertenstein, 2004: User's guide to the NCAR Community Atmosphere Model (CAM3.0). Tech. rep., Climate And Global Dynamics Division, National Center For Atmospheric Research, Boulder, Colorado, USA.

McCabe, G. J., M. P. Clark, and M. C. Serreze, 2001: Trends in Northern Hemisphere surface cyclone frequency and intensity. *J. Climate*, **14**, 2763–2768.

McLandress, C., T. G. Shepherd, J. F. Scinocca, D. A. Plummer, M. Sigmon, A. I. Jonsson, and M. C. Reader, 2011: Separating the dynamical effects of climate change and ozone depletion. Part II: Southern Hemisphere troposphere. *J. Clim.*, **24**, 1850–1868.

Meehl, G., C. Covey, T. Delworth, M. Latif, B. McAvaney, J. F. B. Mitchell, R. J. Stouffer, and K. E. Taylor, 2007a: WCRP CMIP3 multimodel dataset: A new era in climate change research. *Bull. Amer. Meteor. Soc.*, **88**, 1383–1394.

Meehl, G. A. and W. M. Washington, 1996: El Nino-like climate change in a model with increased atmospheric CO_2 concentrations. *Nature*, **382**, 56–60.

Meehl, G. A., et al., 2007b: Global climate projections. *Climate Change 2007: The Physical Science Basis. Contribution of Working Group I to the Fourth Assessment Report of the Intergovernmental Panel on Climate Change*, S. Solomon, D. Qin, M. Manning, Z. Chen, M. Marquis, K. B. Averyt, M. Tignor, and H. L. Miller, Eds., Cambridge University Press, Chap. 10, 747–846.

Monier, E. and B. C. Weare, 2011: Climatology and trends in the forcing of of the stratospheric zonal-mean flow. *Atmos. Chem. Phys. Discuss.*, **11**, 11 649–11 690.

Nakamura, H., 1992: Midwinter suppression of baroclinic wave activity in the Pacific. *J. Atmos. Sci.*, **49**, 1629–1642.

Nakamura, H., T. Sampe, Y. Tanimoto, and A. Shimpo, 2004: Observed associations among storm tracks, jet streams and midlatitude oceanic fronts, "Earth's Climate: The Ocean-Atmosphere Interaction", C. Wang, S.-P. Xie and J. A. Carton. *Eds., Geophys. Monogr.,* 147, American Geophysical Union, Washington, D. C., U. S. A., 329–346.

Newman, P. A., et al., 2009: What would have happened to the ozone layer if chlorofluorocarbons (CFCs) had not been regulated? *Atmos. Chem. Phys.*, **9**, 2113–2128, doi:10.5194/acp–9–2113–2009.

O'Gorman, P. A., 2010: Understanding the varied response of the extratropical storm tracks to climate change. *Proc. Natl. Acad. Sci. U. S. A.*, **107**, 19 176–19 180.

O'Gorman, P. A. and T. Schneider, 2008: Energy of midlatitude transient eddies in idealized simulations of changed climates. *J. Climate*, **21**, 5797–5806.

Orlanski, I. and E. K. M. Chang, 1993: Ageostrophic geopotential fluxes in downstream and upstream development of baroclinic waves. *J. Atmos. Sci.*, **50**, 212–225.

Pavan, V., N. Hall, P. Valdes, and M. Blackburn, 1999: The importance of moisture distribution for the growth and energetics of mid-latitude systems. *Ann. Geophysicae*, **17**, 242–256.

Perlwitz, J. and N. Harnik, 2003: Observational evidence of a stratospheric influence on the troposphere by planetary wave reflection. *J. Clim.*, **16**, 3011–3026.

Polvani, L., D. Waugh, G. Correa, and S.-W. Son, 2011: Stratospheric ozone depletion: the main driver of 20th century atmospheric circulation changes in the Southern Hemisphere. *J. Clim.*, **24**, 795–812, doi: 10.1175/2010JCLI3772.1.

Randel, W. J. and I. M. Held, 1991: Phase speed spectra of transient eddy fluxes and critical layer absorption. *J. Atmos. Sci.*, **48**, 688–697.

Rasch, P. J., et al., 2006: A characterization of tropical transient activity in the CAM3 atmospheric hydrologic cycle. *J. Clim.*, **19**, 2222–2242.

Reichler, T., M. Dameris, and R. Sausen, 2003: Determining the tropopause height from gridded data. *Geophys. Res. Lett.*, **30**, 2042, doi:10.1029/2003GL018 240.

Rivire, G., 2011: A dynamical interpretation of the poleward shift of the jet streams in global warming scenarios. *J. Atmos. Sci.*, **68**, 1253–1272.

Russell, J. L., K. W. Dixon, A. Gnanadesikan, R. J. Stouffer, and J. R. Toggweiler, 2006: The Southern Hemisphere Westerlies in a Warming World: Propping Open the Door to the Deep Ocean. *J. Climate*, **19**, 6382–6390.

Santer, B. D., et al., 2003: Contributions of anthropogenic and natural forcing to recent tropopause height changes. *Sci.*, **301(5632)**, 479–483.

Sassi, F., R. R. Garcia, D. Marsh, and K. W. Hoppel, 2010: The role of the Middle Atmosphere in simulations of the troposphere during Northern Hemisphere

winter: differences between high- and low-top models. *J. Atmos. Sci.*, **67**, 3048–3064.

Scaife, A. A., et al., 2011: Climate change projections and stratosphere-troposphere interaction. *Clim. Dyn.*, 10.1007/s00 382–011–1080–7.

Seager, R., N. Harnik, Y. Kushnir, W. Robinson, and J. Miller(Nakamura), 2003a: Mechanisms of hemispherically symmetric climate variability. *J. Climate*, **16**, 2960–2978.

Seager, R., R. Murtugudde, A. C. Clement, and C. Herweijer, 2003b: Why is there an evaporation minimum at the Equator. *J. Climate*, **16**, 3792–3801.

Seager, R. and N. Naik, 2011: A mechanisms-based approach for detecting recent anthropogenic hydroclimate change. *J. Clim.*, submitted (revised in May 2011).

Seager, R., N. Naik, W. Baethgen, A. Robertson, Y. Kushnir, J. Nakamura, and S. Jurburg, 2010a: Tropical oceanic causes of interannual to multidecadal precipitation variability in southeast South America over the past century. *J. Clim.*, **23**, 5517–5539.

Seager, R., N. Naik, M. Ting, M. A. Cane, N. Harnik, and Y. Kushnir, 2010b: Adjustment of the atmospheric circulation to tropical Pacific SST anomalies: Variability of transient eddy propagation in the Pacific-North America sector. *Quart. J. Roy. Meteor. Soc.*, **136**, 277–296. DOI: 10.1002/qj.588.

Seager, R., N. Naik, and G. Vecchi, 2010c: Thermodynamic and dynamic causes of large-scale changes in the hydrological cycle in response to global warming. *J. Clim.*, submitted.

Seager, R., N. Naik, and G. A. Vecchi, 2010d: Thermodynamic and dynamic mech-

anisms for large-scale changes in the hydrological cycle in response to global warming. *J. Clim.*, **23(17)**, 4651–4668.

Seager, R. and G. Vecchi, 2010: Global warming and the 21st century climate of southwestern North America. *Proc. Nat. Acad. Sci.*, submitted.

Seager, R., et al., 2007: Model projections of an imminent transition to a more arid climate in southwestern North America. *Sci.*, **316**, 1181–1184.

Shaw, T. A. and J. Perlwitz, 2010: The impact of stratospheric model configuration on planetary scale waves in northern hemisphere winter. *J. Clim.*, **23**, 3369–3389.

Shaw, T. A., J. Perlwitz, and N. Harnik, 2010: Downward wave coupling between the statosphere and troposphere: the importance of meridional wave guiding and comparison with zonal-mean coupling. *J. Clim.*, **23**, 6365–6381.

Shindell, D. T., R. L. Miller, G. A. Schmidt, and L. Pandolfo, 1999: Simulation of recent northern winter climate trends by greenhouse-gas forcing. *Nature*, **399**, 452–455.

Shindell, D. T., G. A. Schmidt, R. L. Miller, and D. Rind, 2001: Northern Hemisphere winter climate response to greenhouse gas, ozone, solar, and volcanic forcing. *J. Geophys. Res.*, **106**, 7193–7210, doi:10.1029/2000JD900 547.

Sigmond, M. and J. F. Scinocca, 2010: The influence of basic state on the Northern Hemisphere circulation response to climate change. *J. Clim.*, **23**, 1434–1446.

Sigmond, M., J. F. Scinocca, and P. J. Kushner, 2008: Impact of the stratosphere on tropospheric climate change. *Geophys. Res. Lett.*, **35**, L12 706, doi:10.1029/2008GL033 573.

Sigmond, M., P. C. Siegmund, E. Manzini, and H. Kelder, 2004: A simulation of the separate climate effects of middle-atmospheric and tropospheric CO_2 doubling. *J. Clim.*, **17**, 2352–2367.

Simmons, A. J. and B. J. Hoskins, 1979: The downstream and upstream development of unstable baroclinic waves. *J. Atmos. Sci.*, **36**, 1239–1254.

Simpson, I. R., M. Blackburn, and J. D. Haigh, 2009: The role of eddies in driving the tropospheric response to stratospheric heating perturbations. *J. Atmos. Sci.*, **66**, 1347–1365.

Son, S.-W., N. F. Tandon, L. M. Polvani, and D. W. Waugh, 2009: Ozone hole and Southern Hemisphere climate change. *Geophys. Res. Lett.*, **36**, L15 705, doi:10.1029/2009GL038 671.

Son, S.-W., et al., 2008: The impact of stratospheric ozone recovery on the Southern Hemisphere westerly jet. *Sci.*, **320**, 1486–1489.

Song, Y. and W. A. Robinson, 2004: Dynamical mechanisms for stratospheric influences on the troposphere. *J. Atmos. Sci.*, **61**, 1711–1725.

Stephenson, D. B. and I. M. Held, 1993: GCM response of northern winter stationary waves and storm tracks to increasing amounts of carbon dioxide. *J. Climate*, **6**, 1859–1870.

Thompson, D. W. J., J. M. Wallace, and G. C. Hegerl, 2000: Annular Modes in the extratropical circulation. Part II: Trends. *J. Clim.*, **13**, 1018–1036.

Trenberth, K. E. and J. M. Caron, 2001: Estimates of meridional atmosphere and ocean heat transports. *J. Climate*, **14**, 3433–3443.

Trenberth, K. E., J. M. Caron, and D. P. Stepaniak, 2001: The atmospheric energy budget and implications for surface fluxes and ocean heat transports. *Clim. Dyn.*, **17**, 259–276.

Trenberth, K. E., J. T. Fasullo, and J. Kiehl, 2009: Earth's global energy budget. *Bull. Amer. Meteor. Soc.*, **90**, 311–323.

Trenberth, K. E. and D. P. Stepaniak, 2003: Seamless poleward atmospheric energy transports and implications for the Hadley circulation. *J. Climate*, **16**, 3705–3721.

Vallis, G. K., 2006: *Atmospheric and Oceanic Fluid Dynamics*. Cambridge University Press, Cambridge, U. K., 745 pp.

Vecchi, G. A. and B. J. Soden, 2007: Global warming and the weakening of the tropical circulation. *J. Clim.*, **20(17)**, 4316–4340.

Walker, C. C. and T. Schneider, 2006: Eddy influences on hadley circulations: Simulations with an idealized GCM. *J. Atmos. Sci.*, **63**, 3333–3350.

Williams, G. P., 2006: Circulation sensitivity to tropopause height. *J. Atmos. Sci.*, **63**, 1954–1961.

Wittman, M. A. H., A. J. Charlton, and L. M. Polvani, 2007: The effect of lower stratospheric shear on baroclinic instability. *J. Atmos. Sci.*, **64**, 479–496.

Wu, Y., M. Ting, R. Seager, H.-P. Huang, and M. A. Cane, 2010: Changes in storm tracks and energy transports in a warmer climate simulated by the GFDL CM2.1 model. *Clim. Dyn.*, DOI 10.1007/s00 382–010–0776–4.

Yin, H., 2005: A consistent poleward shift of the storm tracks in simulations of 21st century climate. *Geophys. Res. Lett.*, **32**, L18 701, doi:10.1029/2005GL023 684.